Covalent Transition Metal Borosilicides: Reaction Pathways in Molten Salts for Water Oxidation Electrocatalysis

Daniel Janisch, Fernando Igoa Saldaña, Edouard de Rolland Dalon, Carlos V. M. Inocêncio, Yang Song, Pierre-Olivier Autran, Antoine Miche, Sandra Casale, David Portehault

Covalent Transition Metal Borosilicides: Reaction Pathways in Molten Salts for Water Oxidation Electrocatalysis

Daniel Janisch, Fernando Igoa Saldaña, Edouard De Rolland Dalon, Carlos V. M. Inocêncio, Yang Song, Pierre-Olivier Autran, Antoine Miche, Sandra Casale, and David Portehault*

ABSTRACT: The properties of transition metal borides and silicides are intimately linked to the covalent character of the chemical bonds within their crystal structures. Bringing boron and silicon together within metal borosilicides can then engender different competing covalent networks and complex charge distributions. This situation results in unique structures and atomic environments, which can impact charge transport and catalytic properties. Metal borosilicides, however, hold the status of unusual exotic species, difficult to synthesize and with poor knowledge of their properties. Our strategy consists of developing a redox pathway to synthesize transition metal borosilicides in inorganic molten salts as high-temperature solvents. By studying the formation of Ni_6Si_2B, $Co_{4.75}Si_2B$, Fe_5SiB_2, and Mn_5SiB_2 with in situ X-ray diffraction, we highlight how new reaction routes, maintaining covalent structural building blocks, draw a general scheme of their formation. This pathway is driven by the covalence of the chemical bonds within the boron coordination framework. Next, we demonstrate high efficiency for water oxidation electrocatalysis, especially for Ni_6Si_2B. We ascribe the strongly increased resistance to corrosion, high stability, and electrocatalytic activity of the Ni_6Si_2B-derived material to three factors: (1) the two entangled boron and silicon covalent networks; (2) the ability to codope with boron and silicon an in situ generated catalytic layer; and (3) a rare electron enrichment of the transition metal by back-donation from boron atoms, previously unknown within this compound family. With this work, we then unveil a new chemical dimension for Earth-abundant water oxidation electrocatalysts by bringing to light a new family of materials.

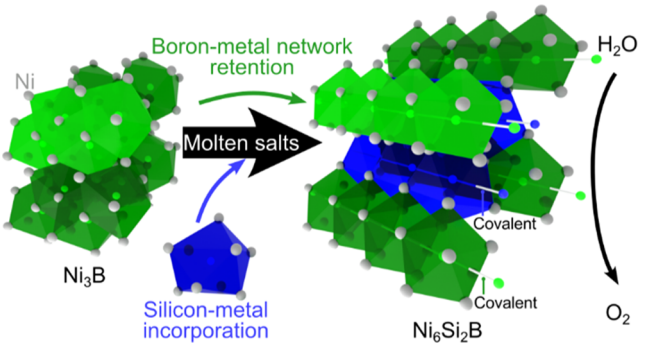

INTRODUCTION

Transition metal borides and silicides show magnetism, charge and spin transport, and especially (electro)catalysis properties that focus most current research efforts on these compounds.[1,2] These behaviors are intimately linked to the nature of chemical bonds ensuring their cohesion: the significant covalent character constrains coordination spheres and atomic charge distribution.[2,3] The bonding scheme is deeply complexified when boron and silicon are combined with a transition metal. Indeed, contrary to mixed anionic compounds,[4] the electronegativities of the different elements in first row transition metal borosilicides are so close that a priori estimation of charge distribution is not possible. This situation can deeply impact the population of the metal 3d states that drive the above-mentioned properties.[5] The tendency to concatenation of boron and of silicon further enriches these chemical systems, by bringing together competitive boron and silicon subnetworks. These materials however require harsh synthesis conditions to order the covalent bonds, so that only traditional solid-state synthesis strategies have been employed.[6−8] This has yielded rare and only bulk solids without knowledge of their potential (electro)catalytic properties. Therefore, transition metal borosilicides provide an opportunity to unlock a structural diversity that has not been explored in the search for electrocatalytic materials.

Our aim here is to bypass the hurdle of metal borosilicide synthesis and then uncover a new family of materials. Our strategy consists of developing a redox chemical route within molten salts as inorganic solvents. Molten salts enable liquid-phase synthesis at temperatures higher than those accessible with usual solvents,[9,10] but lower than those traditionally employed for solids reluctant to crystallization.[10−13] Within this route, we trigger a range of new transformations with only minor atomic rearrangement of covalent frameworks, hence enabling further decrease of the synthesis temperature.

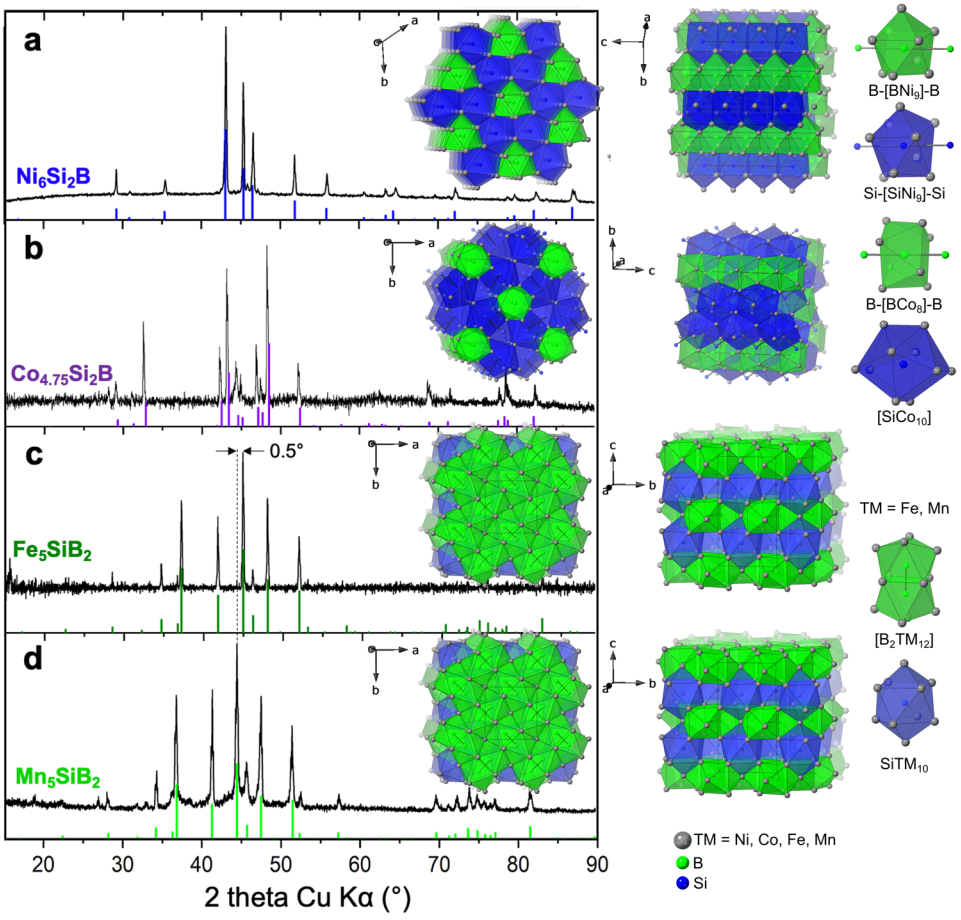

Figure 1. Crystal structure of metal borosilicides. Powder XRD patterns of the borosilicides synthesized in molten salts. The patterns are indexed along PDF-4+ references detailed in the supporting experimental details. The corresponding crystal structures are displayed along two different point of views with the corresponding structural motifs (boron and silicon coordination polyhedra are shown in green and blue, respectively): (a) Ni_6Si_2B (synthesis at 650 °C for 1.5 h), (b) $Co_{4.75}Si_2B$ (1200 °C—8 h), (c) Fe_5SiB_2 (800 °C—2 h), and (d) Mn_5SiB_2 (850 °C—4 h).

By exploring this pathway, we shed the first light on the electrocatalytic properties of metal borosilicides and highlight highly efficient water oxidation electrocatalysts. First row transition metal borides and silicides show promise as precatalysts for alkaline water oxidation electrocatalysis because of their ability to generate in situ supported oxyhydroxide electrocatalytic layers.[10,14,15] The resulting nanocomposites have higher activity and longer lifetime than pure oxyhydroxides.[16−20] Due to covalent bonds, some borides and silicides resist corrosion during water oxidation so that only a thin layer of oxyhydroxide forms. Meanwhile, boride or silicide cores remain and act as efficient current collectors, thanks to their high electrical conductivity. Silicon[10] and boron[21] can be incorporated into the surface oxyhydroxide layer, thus modifying its local structure and intrinsic electrocatalytic properties. To date, enhancement of water oxidation electrocatalytic properties has been observed when iron, cobalt, and nickel are combined with only a single p-block element, boron or silicon,[10,22] but also phosphorus,[23−25] carbon,[26−28] and selenium.[29−31] Modifying the composition of these materials impacts water oxidation electrocatalysis by tuning the corrosion resistance, the electrical conductivity, and the local environment of catalytic sites in the oxyhydroxide-related layers. This is demonstrated for multimetallic boride[32,33] and P,N-doped boride catalysts.[34−36] But these materials retain the structure and coordination of the parent binary solids, hence limiting the modularity of atomic environments. Combining two nonoxidic p-block elements into specific structures to design electrocatalysts has been attempted for highly ionic compounds, such as CoPS,[37] which readily convert into oxides during electrocatalysis. By selecting silicon and boron, we explore metal atom environments not accessible otherwise and ensure that the materials are predominantly covalent while maintaining metallic properties.

This work brings to light a general pathway in molten salts to transition metal borosilicides for water oxidation electrocatalysis. We analyze in situ the crystallization mechanisms of Ni_6Si_2B, $Co_{4.75}Si_2B$, Fe_5SiB_2, and Mn_5SiB_2 to highlight new reaction routes that are driven by the boron-based covalent subnetwork. Next, we demonstrate for some of these materials a high efficiency in water oxidation electrocatalysis. We then probe the electronic states of these materials, especially charge transfers between atoms, to unveil how they drive surface reconstruction during water oxidation electrocatalysis on transition metal borosilicides. We thus provide guidelines for the design of corrosion-resistant and Earth-abundant water oxidation electrocatalysts.

RESULTS AND DISCUSSION

Synthesis of Transition Metal Borosilicides. The synthesis procedure (details are provided in the Experimental Methods section) is designed to ensure the reduction of

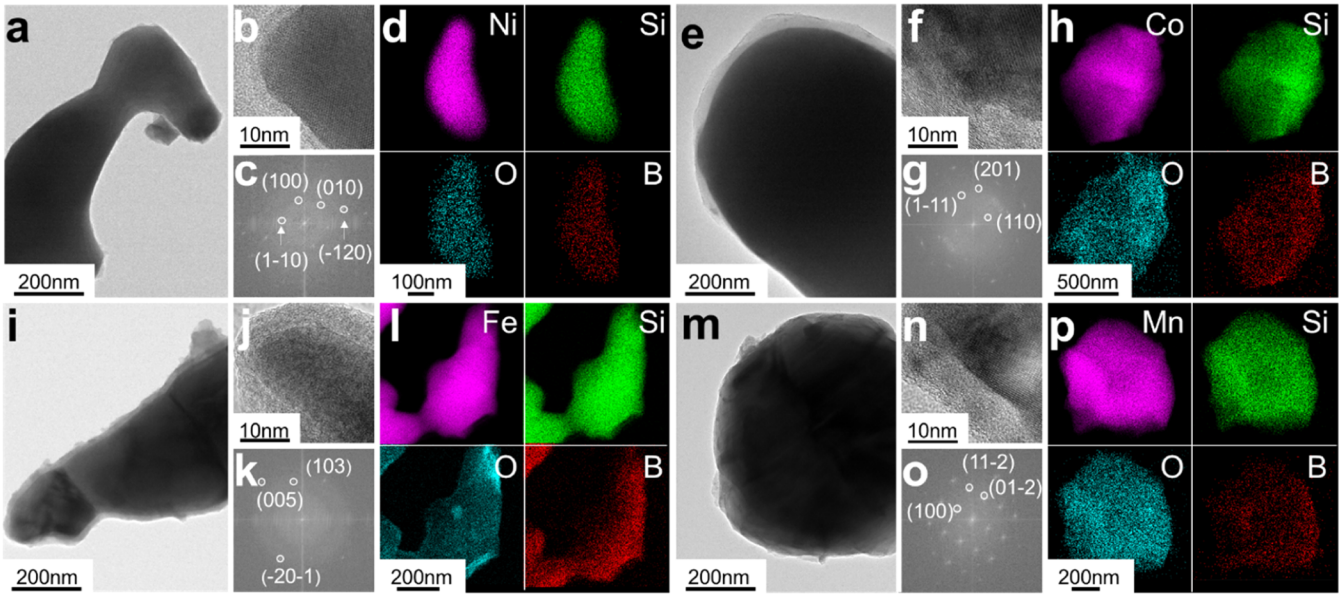

Figure 2. Nanostructure of borosilicides. TEM analysis of as-prepared (a–d) Ni_6Si_2B, (e–h) $Co_{4.75}Si_2B$, (i–l) Fe_5SiB_2, and (m–p) Mn_5SiB_2. (a, e, i, m) TEM, (b, f, j, n) HRTEM images, (c, g, k, o) corresponding FFTs and (d, h, l, p) STEM-EDS maps.

transition metal chlorides with Na_4Si_4 and $NaBH_4$, which serve both as reducing agents and Si and B source, respectively. NaH is used as additional reducing agent to ensure total reduction of the metal cations according to the following equation:

$$a\mathrm{TMCl}_x + b/4\mathrm{Na}_4\mathrm{Si}_4 + c\mathrm{NaBH}_4 + (a{\cdot}x - b - c)\mathrm{NaH} \rightarrow \mathrm{TM}_a\mathrm{Si}_b\mathrm{B}_c + a{\cdot}x\mathrm{NaCl} + (3c + a{\cdot}x - b)/2\mathrm{H}_2$$

The eutectic mixture LiCl-KCl is chosen as a cheap, sustainable solvent with a relatively low melting point (353 °C). Table S1 summarizes the conditions we employed to reach Ni_6Si_2B, $Co_{4.75}Si_2B$, Fe_5SiB_2, and Mn_5SiB_2. By using a molten salt medium, we could significantly lower reaction temperatures and times compared to those of previously described solid-state reactions (Table S1). Powder XRD (Figure 1) coupled to Rietveld refinement (Figure S1 and Table S2) indicates cell parameters in agreement with the literature.

Ni_6Si_2B (Figure 1a, inset) is made of linear chains of face-sharing BNi_9 polyhedra that are connected by B–B covalent bonds. Additional linear chains of face-sharing $SiNi_9$ polyhedra are nested between the BNi_9 chains, also encompassing Si–Si covalent bonds. Note that the incorporation of silicon constrains sufficiently the boron subnetwork to enable B–B covalent bonding, while this situation is not met in borides with such low Ni:B ratio.[5] $Co_{4.75}Si_2B$ (Figure 1b, inset) is made of linear face-sharing BCo_8 polyhedra chains, again connected by B–B bonds, as well as chains of face- and edge-sharing $SiCo_{10}$ polyhedra, too far from each other to enable bonding between Si atoms. Fe_5SiB_2 and Mn_5SiB_2 are isostructural (Figure 1**c-d**, insets). They are built on alternating layers of BTM_8 and $SiTM_{10}$ (TM = Fe, Mn) polyhedra, which share faces and edges in the boron-based layers and edges in the silicon-based layers. Two face-sharing BTM_8 polyhedra form B_2TM_{12} dumbbells, with B atoms connected by a covalent bond. The orientation of these dumbbells alternates in the boron layers. There is no bonding between Si atoms. Following the smaller atomic radius of Fe vs Mn, the cell volume decreases from Fe_5SiB_2 to Mn_5SiB_2, as evidenced by a ~ 0.5° (2 theta Cu Kα) shift of the XRD reflections to higher angles (Figure 1c,d) and by the refined cell parameters (Table S2). Noteworthy, in all of these compounds, metal atoms are involved in at least one M-Si or M-B bond, but there is no Si–B connection. As for the nickel system, we observe for all metal borosilicide that incorporation of silicon brings B atoms close together, thus establishing B–B covalent bonds that are not found in borides with such low boron contents.[5]

Transmission electron microscopy (TEM) (Figure 2) shows that the samples encompass ill-defined submicronic particles, except for Ni_6Si_2B (Figure 2a) that is made of 50 to 200 nm particles, with a crystallite size of 66 nm derived from Rietveld refinement. The smallest size of Ni_6Si_2B is related to its lowest synthesis temperature (650 °C) among the borosilicides studied in this work. $Co_{4.75}Si_2B$ (Figure 2e) synthesized at the highest temperature (1200 °C) encompass particles beyond 2 μm. The particle sizes of Fe_5SiB_2 and Mn_5SiB_2 (Figure 2i,m) lie between them, again in agreement with their respective synthesis temperatures (800–850 °C). High resolution TEM (HRTEM) images (Figure 2b,f,j,n) and their corresponding Fast Fourier Transforms (FFTs, Figure 2c,g,k,o) confirm the respective crystal structures. STEM-EDS maps (Figure 2d,h,l,p) indicate the homogeneous distribution of the transition metals, Si and B, throughout the particles with corresponding EDS spectra shown in Figure S2.

Ex Situ Insights Into Synthesis Mechanism: Mixtures of Binary Phases. We then questioned the formation mechanisms. First, we quenched the reaction medium below the temperature used to obtain the metal borosilicides. Mixtures of the respective binary silicides and borides were isolated, which can be considered as reaction intermediates (noted as TM-Int samples). The crystalline phase ratios of the binary phases were evaluated by Rietveld refinement (Figure S3). The B and Si contents in **Ni-Int** and **Fe-Int** evaluated from the phase fractions (Table S3) are consistent with the initial molar ratios of reagents (B:Si = 41:59 and 37:63 respectively, versus 41:59 and 33:67 expected), which makes unlikely the presence of an amorphous phase. This is confirmed by TEM, which shows that **Ni-Int** and **Fe-Int**

(Figure S4a,c) are predominantly made of crystalline particles with only little amounts of low-contrast material, presumably amorphous, at the surface of the particles.

Evaluation of boron and silicon contents in the crystalline components of **Co-Int** and **Mn-Int** from Rietveld refinements of the powder patterns highlights significant deviation from the expected molar ratios of the reagents (B:Si = 55:45 and 39:61 (excluding the Mn^0 share in Table S3) for **Co-Int** and **Mn-Int** versus 35:65 and 67:33, respectively). This discrepancy is reflected by TEM images (Figure S4b,d) indicating some low-contrast amorphous components, which might be ascribed to noncrystalline Si- and B-rich compounds, not detected by XRD. Overall, the recovery of binary phases at intermediate temperatures hints at sequential crystallization of silicides and borides, followed by their reaction to form borosilicides.

In Situ Study of Synthesis Reaction Mechanisms. To assess the sequence of crystallization, we have monitored the syntheses by synchrotron radiation-based in situ XRD. This was performed by using a custom-made capillary oven enabling to mimic lab-scale syntheses, in a 1 mm-diameter capillary filled with the reaction mixture and kept under argon flow (Figure S5). During heating, we recorded XRD patterns in transmission mode every 90 s with a 5 s acquisition time by continuously scanning the capillary to ensure the representativeness of the diagrams. The resulting diffractograms are depicted as heatmaps, with few selected diagrams plotted in one dimension in Figures S6–S13. Initially, the predominant diffraction peaks stem from the still solid LiCl-KCl mixture with minor peaks of the metal chloride precursor. Above the melting point of the eutectic mixture, these reflections disappear, and significant diffuse scattering from the inorganic liquid is observed at low angles. Sequential Rietveld refinements were carried out to assess the phase fraction of crystalline phases in the salt melt, as shown in Figure S14.

A general reaction pathway could be identified from the crystalline phases detected and their relative contents in the reaction media (Figure 3). First, the metal chloride is reduced to elemental metal before melting of the salt, between 300 and 350 °C (Figures S6, S8, S10, and S13). Above the melting point, the metal reacts with silicon and boron precursors to yield binary silicides (TM-Si) and borides (TM-B) (Figures 3, S6–S14), in agreement with ex situ data on quenched reaction media. *h*/*o*-Ni_2Si and Ni_3B are forming at the lowest temperature (ca. 350 °C), followed by Mn_2B and Mn_5Si_3 (400 °C), Fe phases (Fe_2B 425 °C and Fe_5Si_3 450 °C), and Co phases (Co_2Si 515 °C and Co_2B 550 °C) (Figures S6–S14).

In the third and last step, the binary compounds react together yielding the ternary borosilicide (Figures S6–S13). The onsets of crystallization (Figure 3) of Ni_6Si_2B, Fe_5SiB_2, and Mn_5SiB_2 are ca. 430 °C, 575, and 825 °C, respectively. $Co_{4.75}Si_2B$ could not be observed since its synthesis temperature exceeds the operating temperature of the capillary oven used for in situ XRD. Reflections of nickel borosilicide rapidly gain in intensity from ca. 430 °C at the expense of *h*-Ni_2Si (blue triangles) and Ni_3B (green triangles), while *o*-Ni_2Si (violet triangles) only slowly feeds into the ternary compound. This indicates the higher stability of the *o*-Ni_2Si polymorph, in line with its predominance in reported syntheses.[38,39] We note that the Ni_3B crystal structure (Figure 4a) already contains the chains of face-sharing BNi_9 polyhedra building Ni_6Si_2B, but these chains are corrugated and lack the B–B bonds connecting the polyhedra in Ni_6Si_2B. With Ni_6Si_2B crystallization, the BNi_9 polyhedra align, which brings boron atoms

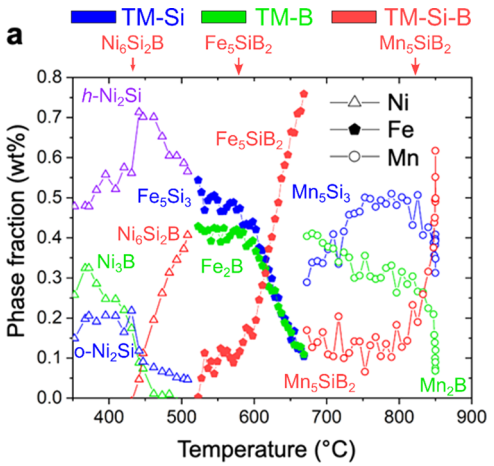

Figure 3. Evolution of intermediate species and products during the crystallization of transition metal borosilicides according to in situ XRD. Phase fractions as a function of temperature during the transformation from binary transition metal silicides (TM-Si, blue) and borides (TM-B, green) to ternary borosilicides (red), where TM is Ni (triangle), Fe (pentagon), or Mn (circle). For the Ni system, blue and purple open triangles represent the phase fractions of o-Ni_2Si and h-Ni_2Si, respectively. The red arrows on the top indicate the crystallization onset temperatures of the borosilicides.

sufficiently close to each other to form linear covalent B–B chains. We observe that $SiNi_9$ building blocks of intermediate *o*-Ni_2Si are also maintained in the borosilicide, where they are getting sufficiently close to each other to form linear covalent Si–Si chains. One can then suggest that these $SiNi_9$ units insert between the B-based chains during the crystallization of Ni_6Si_2B.

Although we could not observe in situ the crystallization of the cobalt borosilicide, we stress out that the linear chains of face-sharing BCo_8 polyhedra with B atoms connected by covalent bonds in the borosilicide are already found, identical, in the Co_2B intermediate (Figure S15), making Co_2B a likely gateway for the formation of $Co_{4.75}Si_2B$. The $SiCo_{10}$ polyhedra of intermediate Co_2Si are also maintained in the resulting borosilicide. But contrary to the nickel system, Si atoms are too far from each other to be connected by covalent bonds, in both the intermediate and final compounds.

Since iron and manganese borosilicide are isostructural, it is not surprising that they follow the same reaction mechanism. Fe_5SiB_2 and Mn_5SiB_2 are layered compounds, while the intermediates TM_2B (TM = Fe, Mn) contain linear chains of face-sharing BTM_8 polyhedra, so that the structural evolution is less straightforward (Figure 4b). The TM_5SiB_2 structure is built from B_2TM_{12} dumbbells that correspond to two face-sharing BTM_8 polyhedra with B atoms connected by a covalent bond. These building units can be traced back to the linear chains of TM_2B: breaking every second B–B bond in TM_2B yields the B_2TM_{12} dumbbells. In the borosilicide, every second dumbbell is twisted. Like for the nickel and cobalt systems, we observe that the evolution of the boron coordination network from the intermediate to the borosilicide can be explained by only minor movements of B and metal atoms (Figure 4b). The silicon network undergoes deeper reconstruction: the covalent Si–Si bonds forming zigzag chains in the TM_5Si_3 intermediate are totally broken to form $SiTM_{10}$ polyhedra layers in TM_5SiB_2, where Si atoms are too far from each other to form covalent bonds.

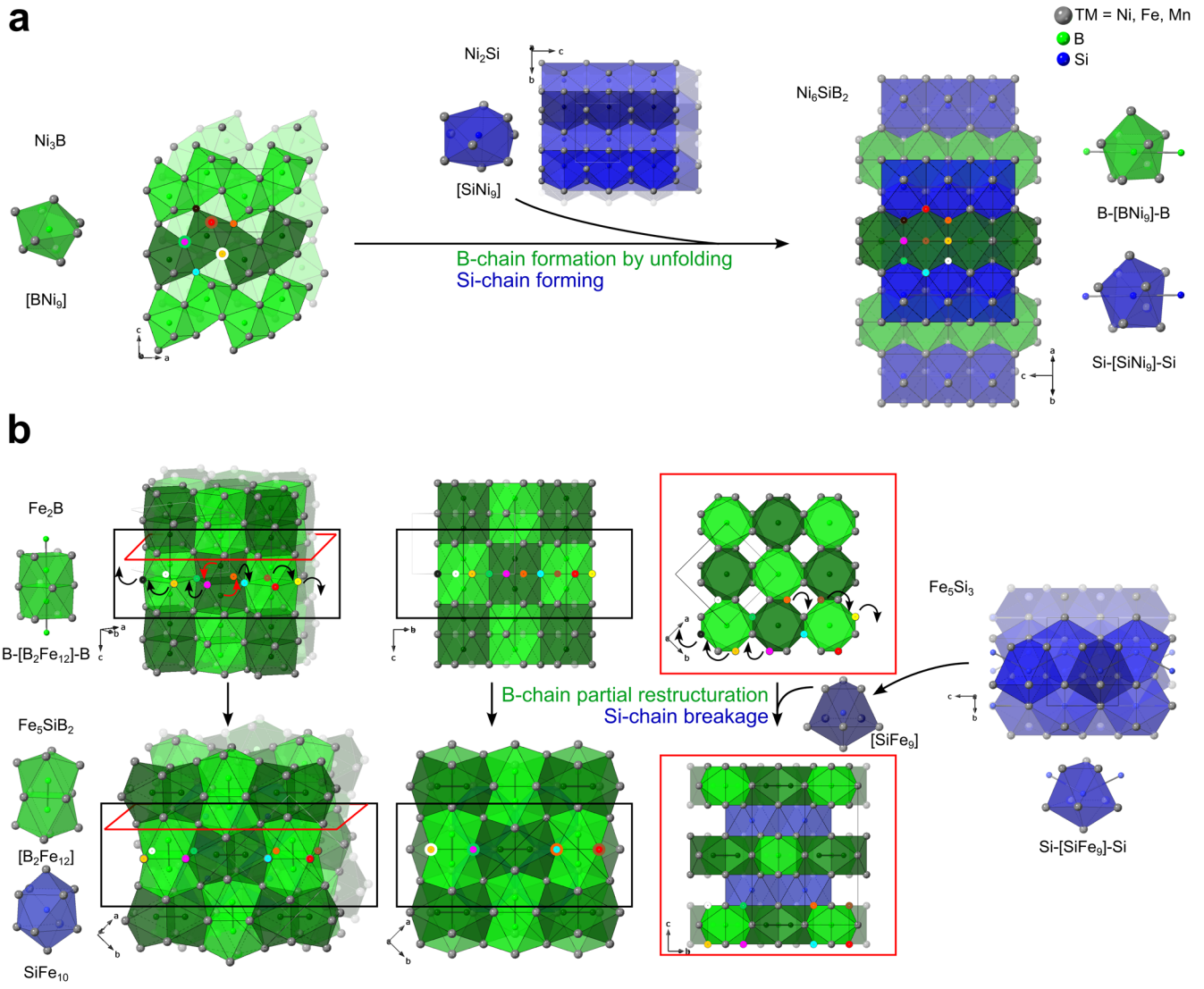

Figure 4. Mechanisms of the crystallization of transition metal borosilicides unveiled by in situ XRD. (a) Scheme of the reaction mechanism from Ni_3B and o-Ni_2Si to Ni_6Si_2B through insertion of Si (blue polyhedra) and slight unfolding of face-sharing BNi_9 polyhedra chains (green) to form covalently bonded linear B-chains. (b) Scheme of the reaction mechanism from Fe_2B (Mn_2B) and Fe_5Si_3 (Mn_5Si_3) to Fe_5SiB_2 (Mn_5SiB_2, respectively). The evolution of the boron coordination network can be explained by partial breakage of the covalent B-chains into B_2Fe_{12} dumbbells that alternatively twist. Insertion of Si proceeds from breakage of the covalently bonded zigzag Si polyhedra chains in Fe_5Si_3 (Mn_5Si_3). Light and dark green boron coordination polyhedra correspond to the same crystallographic sites, but different colors are used as guides to the eye to highlight structural motifs. Color-coded atoms, black and red arrows in b illustrate the little movements that metal atoms must undergo to ensure evolution of the boron coordination network from the boride to the borosilicide. When two metal atoms are superimposed on the scheme, the front-end one and the back-end one are colored by inner and outer circles, respectively.

In the four systems that we examined, the boron coordination network is only slightly modified when evolving from the intermediate transition metal boride to the borosilicide. The silicon coordination is more impacted, involving in some cases the breakage of all Si−Si bonds in the intermediate silicide. This is in line with the higher bonding strength of borides compared to silicides.[40,41] Overall, we highlight how the higher covalency of borides makes the boron coordination network and its structural motifs the likely building blocks of the borosilicide structures by constraining the coordination geometry of boron atoms.

Alkaline Water Oxidation Electrocatalysis. Electrocatalytic properties for the Oxygen Evolution Reaction (OER) were assessed for reference IrO_2, respective binary silicides and borides (Figure S16), reaction intermediates (**TM-Int** samples), and oxides as references. Composite ethanolic inks containing the catalyst powders, carbon black as a conductive additive, and Nafion were deposited onto polished glassy carbon rotating disk electrodes. Cyclic voltammograms (CVs) were recorded in an O_2-saturated 0.1 M KOH electrolyte purified from Fe impurities (Figure 5).[32] The curves were corrected for the ohmic drop obtained by electrochemical impedance spectroscopy (EIS).

Typical for Ni-based catalysts in the OER (Figure 5a) is the oxidation wave Ni^{2+}/Ni^{3+} at about 1.45 V vs RHE in the oxidation branch. The significant growth of the redox waves during 50 cycles (Figures S17a and S18a) is attributed to an increase in the thickness of an Ni (oxy)hydroxide layer, as was previously observed for similar binary compounds.[39,42] Ni_6Si_2B strongly activates during 50 cycles between 1 and 2 V vs RHE

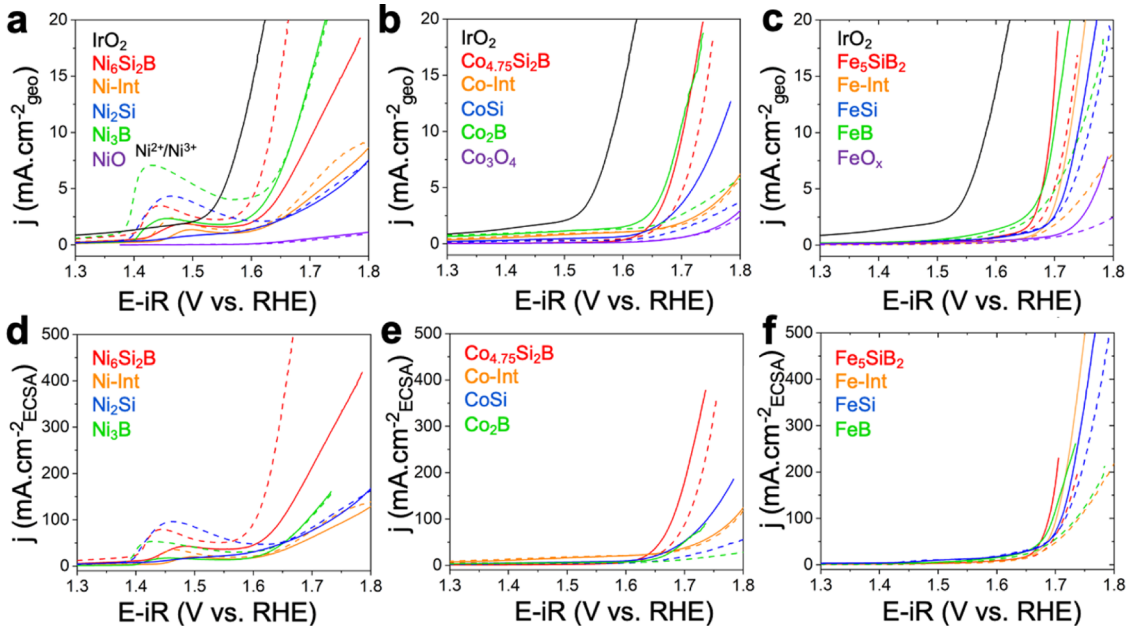

Figure 5. Water oxidation electrocatalytic activity. *iR*-corrected polarization curves recorded in Fe-purified and O_2-saturated 0.1 M KOH at a scan rate of 20 mV·s^{-1} on a rotating disk electrode (RDE) at 1600 rpm. The current is normalized vs the geometrical surface area for (a) Ni-, (b) Co-, (c) and Fe-based samples. Polarization curves normalized by ECSA for (d) Ni-, (e) Co-, and (f) Fe-based samples. Solid and dashed lines indicate the 1st and 50th cycles, respectively.

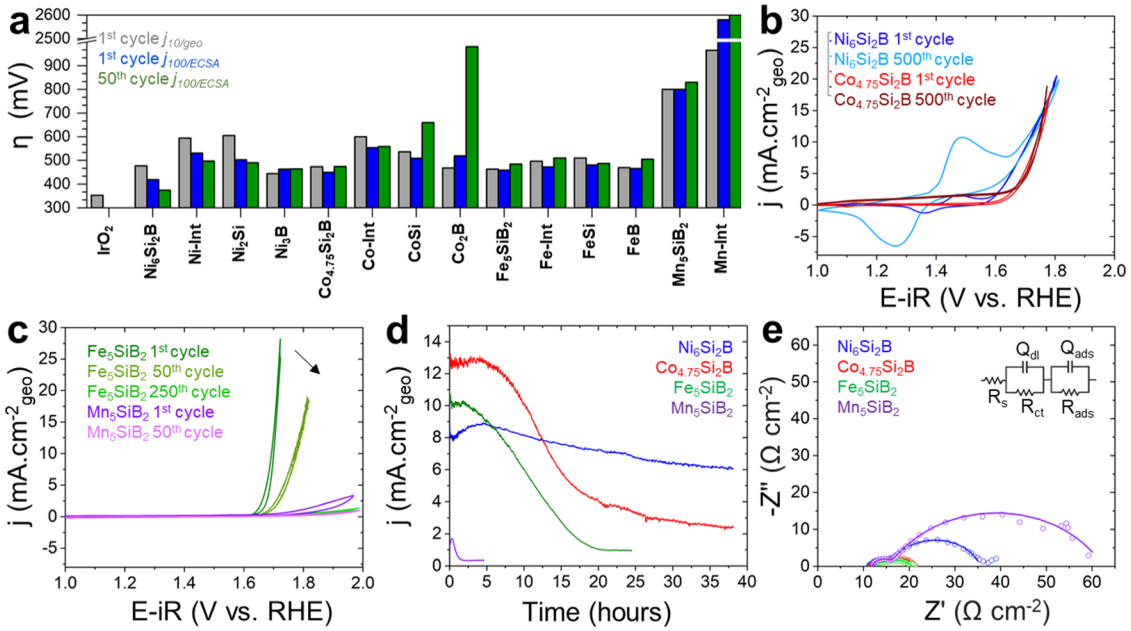

Figure 6. Accelerated aging study of borosilicide OER electrocatalysts. (a) Bar chart of overpotentials extracted from 1st cycle of geometric surface area normalized and 1st and 50th cycle of ECSA-normalized polarization curves. Stability assessment of transition metal borosilicides: *iR*-corrected polarization curves in 0.1 M Fe-purified and O_2-saturated KOH obtained with a scan rate of 20 mV·s^{-1} on a rotating disk electrode (RDE) at 1600 rpm for (b) Ni_6Si_2B and $Co_{4.75}Si_2B$, and (c) Fe_5SiB_2 and Mn_5SiB_2. (d) CA measurement at 2 V vs RHE in Fe-purified and O_2-saturated 0.1 M KOH on glassy carbon plate (GC) electrodes. (e) Nyquist plot recorded at 2 V vs RHE of pristine samples on GC electrodes, with inset showing the equivalent circuit used to evaluate the internal resistance.

with the overpotential decreasing from 480 to 400 mV at 10 mV per geometric surface area ($j_{10/geo}$). The activities are then getting closer to the IrO_2 benchmark (325−350 mV).[34,43] After 50 cycles, the potential at $j_{10/geo}$ ranks in the order of Ni_6Si_2B (1.63 V) < Ni_3B (1.68 V) < Ni-Int (1.83 V) < Ni_2Si (1.86 V), so that Ni_6Si_2B shows the lowest overpotential and is then the most active catalyst. This agrees with the corresponding Tafel slope (Figure S19) at 97 mV dec^{-1} after 50 cycles, thus approaching reported kinetics on IrO_2 (65 mV·dec^{-1}).[34,43]

$Co_{4.75}Si_2B$ and Fe_5SiB_2 show slightly lower activity than Ni_6Si_2B (Figures 5b,c and S17b), with overpotentials of 470 and 500 mV, respectively, coinciding with the respective values for Co_2B and FeB in the first cycle. Corresponding Tafel slopes

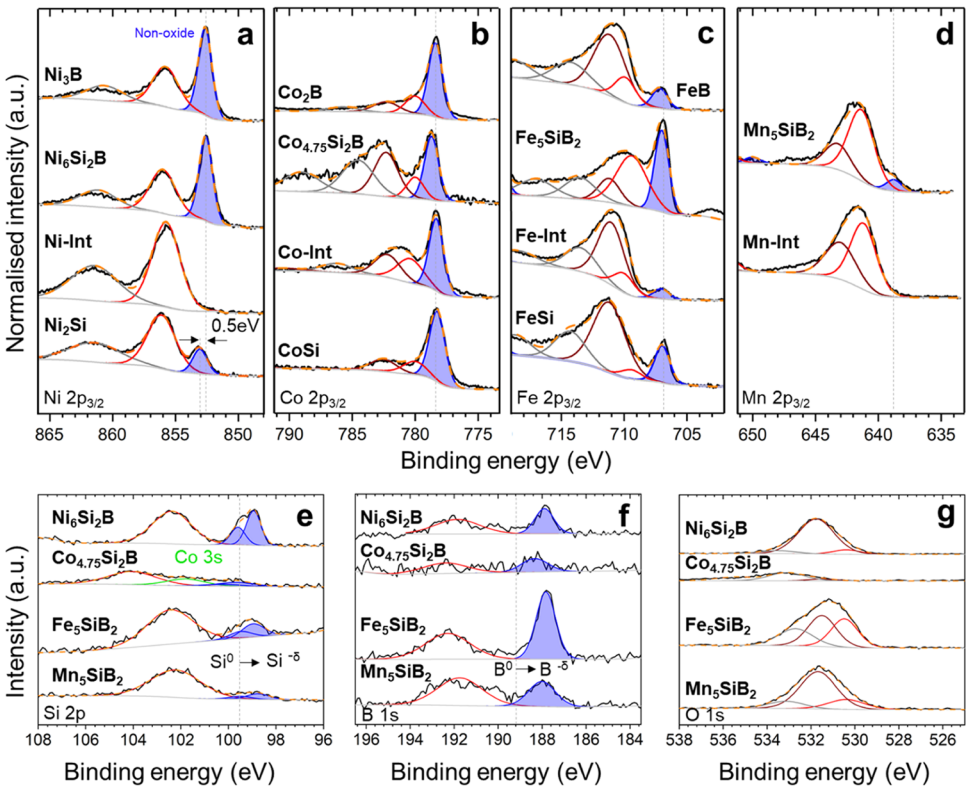

Figure 7. Bulk and surface electronic states of transition metal borosilicides. High resolution XP spectra and corresponding deconvolutions of as-prepared binary borides, binary silicides, reaction intermediates (**TM-Int**), and ternary borosilicides. The surfaces of $Co_{4.75}Si_2B$, Co_2B, and Fe_5SiB_2 were Ar^+ sputtered for 15 min prior measurements. (a) Ni $2p_{3/2}$, (b) Co $2p_{3/2}$, (c) Fe $2p_{3/2}$, (d) Mn $2p_{3/2}$, (e) Si 2p, (f) B 1s, and (g) O 1s regions. The shaded blue peaks correspond to nonoxide components. The other peaks correspond to contributions from oxidized species. The vertical dashed lines correspond to the binding energies of elemental references.

(Figure S19, Table S5) are 99 $mV{\cdot}dec^{-1}$ for $Co_{4.75}Si_2B$ and 46 $mV{\cdot}dec^{-1}$ for Fe_5SiB_2. While a slight decrease in activity was measured for $Co_{4.75}Si_2B$ and Fe_5SiB_2, deactivation is more severe for the binary compounds, with overpotentials increasing by 230, 10, 210, and 50 mV for CoSi, FeSi, Co_2B, and FeB, respectively. Manganese-based compounds show very low activity toward the OER (Figure S17c) consistent with other reports of Mn-based electrocatalysts (Table S5).

As the geometric surface area may not reflect a similar amount of catalyst active sites from one sample to the other, we have normalized the current densities by the electrochemical surface area (ECSA, Figures 5d–f and S17d) evaluated from the measured double layer capacitance (C_{DL}, supporting text 1, Figures S20 and S21, Table S6).[43] ECSA normalization confirms the superior catalytic activity of all four ternary borosilicides compared to binary compounds, with lower overpotentials (Figure 6a). Ni_6Si_2B, $Co_{4.75}Si_2B$, and Fe_5SiB_2 show low overpotentials of 374, 450, and 459 mV at 100 $mA{\cdot}cm^{-2}$ ($j_{100/ECSA}$), respectively (Figures 5d–f and 6a).

To ensure that the differences in the OER activity we measured are relevant, we have assessed the stability of the electrocatalytic properties first by voltammetric cycling between 1 and 2 V vs RHE. While Ni_6Si_2B and $Co_{4.75}Si_2B$ show steady OER current over 500 cycles (Figure 6b), Fe_5SiB_2 and Mn_5SiB_2 experience degradation of the anodic current before the 50th cycle (Figure 6c). Although the OER current is stable for Ni_6Si_2B, we observe an increase in the reversible Ni^{2+}/Ni^{3+} redox wave (Figure S18a), which indicates further oxidation of the sample. Because long-term cycling is harsher than operational potentiostatic measurements,[44] we have completed cycling measurements with chronoamperometry experiments (CA) at 2 V vs RHE. Prior to CA, Ni_6Si_2B and $Co_{4.75}Si_2B$ were activated by 50 cycles between 1 and 2 V vs RHE whereas Fe_5SiB_2 and Mn_5SiB_2 were cycled only 5 times to avoid fast degradation of the activity. Ni_6Si_2B exhibits a slight decrease in current density over 38 h whereas $Co_{4.75}Si_2B$, Fe_5SiB_2, and Mn_5SiB_2 show a strong loss of activity from 10, 5, and 1.5 h, respectively (Figure 6d). This evolution can be ascribed to deactivation or detachment of the catalysts from the current collector.

The evolution of charge transfer kinetics within the electrodes was then assessed by potentiostatic electrochemical impedance spectroscopy (PEIS) in OER conditions at 2 V vs RHE before and after activation (CV), and then after consecutive CA measurements for a total of 38 h at 2 V vs RHE (supporting text 1 and Figure S22). Figure 6e depicts Nyquist plots of the pristine samples before activation (before CV), which were fitted with an equivalent circuit $R_s(Q_{dl}R_{ct}(Q_{ads}R_{ads}))$ (Table S7).[45,46] The charge transfer resistances (R_{ct}) for the four borosilicides are initially similar and low, indicating highly conductive catalyst films. R_{ct} increases after activation (Table S7), which agrees with the growth of poorly conductive metal (oxyhydr)oxide layers in agreement with the $Ni^{2+} \rightarrow Ni^{3+}$ wave (Figure 5a). R_{ads} corresponds to the adsorption resistance of oxygen containing intermediates. It is initially lowest for cobalt and iron borosilicides, which suggests less favorable OER kinetics on pristine Ni and Mn borosilicides. Upon activation, R_{ads} decreases for Ni, Co, and Fe borosilicides, thus indicating more efficient adsorption/desorption processes of OH^- and

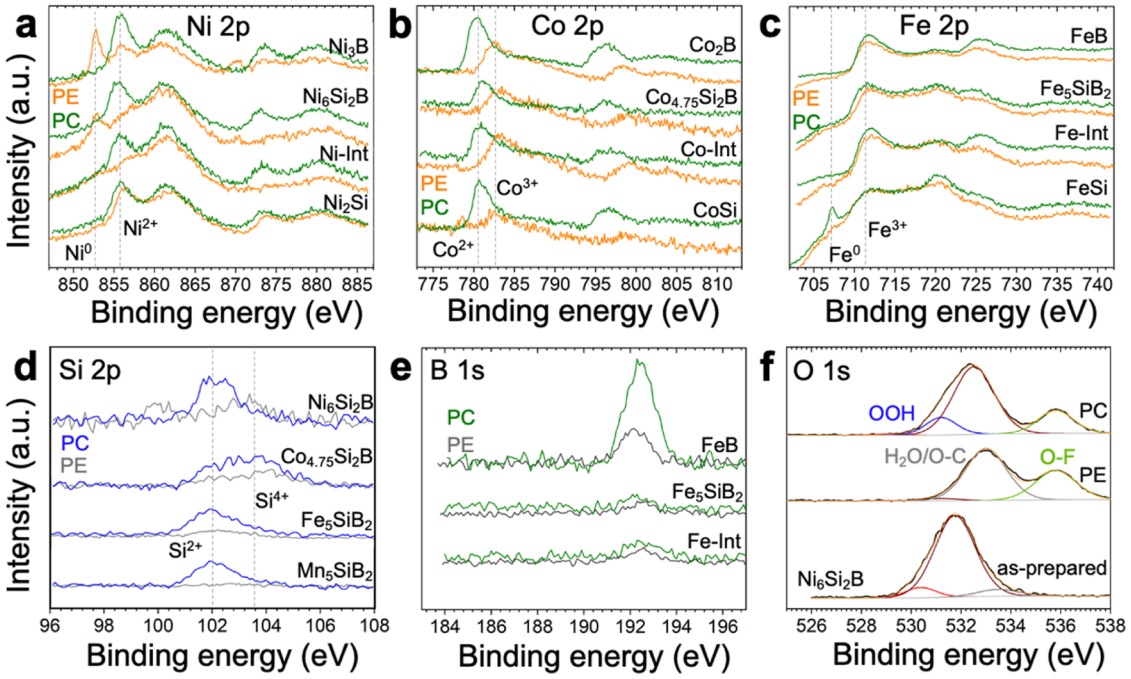

Figure 8. Surface states of transition metal borosilicide-derived water oxidation electrocatalysts. Non-normalized HR-XPS profiles of (a) Ni-based (Ni 2p), (b) Co-based (Co 2p), and (c) Fe-based (Fe 2p) before (PE, orange) and after (PC, green) chronoamperometry. Corresponding (d) Si 2p before (PE, gray) and after (PC, blue), (e) B 1s before (PE, gray) and after (PC, green) CA, (f) deconvoluted O 1s spectra of the as-prepared Ni_6Si_2B powder, before (PE) and after catalysis (PC). In panel (a), the broad peak at ~862.5 eV corresponds to the F KL2 peak[53] from fluorine in the Nafion polymer of the electrode film.

intermediates on the (oxyhydr)oxide layers formed in situ during activation. Low R_{ads} values also correlate with high current densities in the beginning of the CA measurements for $Co_{4.75}Si_2B$ and Fe_5SiB_2. Overall, we observe for nickel, cobalt, and iron borosilicides electrocatalytic properties that remain steady during the first hours of operation after activation. Ni_6Si_2B stands out for its superior stability in terms of surface states, as R_{ads} does not increase significantly after tenths of hours under operation, contrary to other borosilicides. The inflection point of the current density curve after ca. 6−7 h of CA (Figure 6d) may indicate growth of the poorly conductive (hydr)oxide layers during CA (R_{ct} increase) or catalyst detachment from the electrode. In any case, it does not strongly affect the adsorption processes (R_{ads}).

The large decrease of R_{ads} upon activation (Table S7) and its steady value upon CA indicates that Ni_6Si_2B is more robust than the other materials versus surface degradation. Energy dispersive X-ray spectroscopy coupled to scanning electron microscopy (SEM-EDS, Figures S24−S26) shows a steady Si/TM atomic ratio before and after the OER for Ni, Fe, and Mn borosilicides, while the Si content in the Co samples decreases upon operation. The low energy of the B−K transition results in strong autoabsorption, including by the Nafion binder, that makes its detection poorly reliable.

Bulk and Surface Electronic States. To understand the chemical and structural evolutions of the transition metal borosilicides during water oxidation electrocatalysis, we have first probed the electronic states of the different elements in the pristine borosilicides by using X-ray photoelectron spectroscopy (XPS, Figure 7, detailed discussion in supporting text 2).

The Ni $2p_{3/2}$ spectrum of Ni_6Si_2B shows three contributions at 852.6, 856.0, and 861.2 eV (Figures 7a, S27a and supporting text 2). The low binding energy (BE) Ni 2p contribution is consistent with values measured for Ni_3B (Figure S27a) and reported for elemental Ni[14] and nickel borides.[42] This peak appears at lower binding energy than for Ni_2Si (Figure 7a) and other silicides, which shows electron enrichment of Ni 3d states.[39] The Si 2p doublet at low BE (Figure 7e), consistent with the spectra of Ni_2Si (Figure S27e) and other silicides,[31] is negatively shifted compared to elemental Si,[47] which indicates electron enrichment of Si from its closest Ni neighbors atoms. Likewise, the low valence B 1s BE (Figure 7f) is consistent with the spectra of metal-rich borides (Figure S27f) and negatively shifted compared to elemental boron.[48] This indicates the electron enrichment of boron from nickel. Overall electron transfer from Ni to Si and B agrees with the electronegativity scale, which yields a global charge state $Ni^{+\delta+\delta'}Si^{-\ \delta}B^{-\ \delta'}$. Enrichment of Ni 3d states, opposite to the overall electron transfer, is a signature of back-donation, well documented in nickel borides: hybridization with boron sp states populates the Ni 3d states, which compensates the Ni 2p binding energy shift expected from global electron impoverishment of the metal.[5,49] Globally, Ni 3d states are then electron-enriched compared to elemental nickel and silicides but less than in nickel borides because Si partially alleviates the effect by pulling out electrons from the metal atoms.

The surface of as-prepared Ni_6Si_2B is oxidized, as evidenced by a Ni $2p_{3/2}$ peak and its satellite at high BE (Figure 7a), as well as O 1s BE (Figure 7g) indicative of Ni (oxyhydr)oxide species that can form upon exposure to air (Figure S27g).[50] Partially oxidized Si and B species are also evidenced by high BE components in the Si 2p (Figure 7e)[47] and B 1s (Figure 7f)[51,52] regions. In Ni_6Si_2B, the Si 2p oxidation contribution is slightly shifted to lower energy compared to that of Ni_2Si (102.6 eV, Figure S27e). The corresponding B 1s component

is positively shifted compared with Ni_3B (Figure S27f). Boron is then deprived of electrons in the oxidized layer at the surface of the borosilicide. On the opposite, silicon is slightly less oxidized than on the silicide, which could indicate a sacrificial anodic effect of boron.

A similar analysis of cobalt, iron, and manganese borosilicides (detailed discussion in supporting text 2) shows that silicon acts as electron acceptor in the four borosilicides. While boron is also generally an electron withdrawing group, we observe that it also enriches the transition metal 3d band by hybridization in the case of Ni_6Si_2B, and also most probably to a lesser extent in Mn_5SiB_2. This is the first time this effect, previously documented for binary nickel borides,[5,49] is reported for ternary compounds. Upon exposure to air, the materials exhibit metal oxyhydroxide-related surface layers, where Si species (Figure S27e) are electron-enriched when compared to oxidized surfaces derived from reference binary silicides, thus indicating higher stability versus corrosion of the silicon species at the surface of the ternary compounds.

XPS was then used to probe surface states in the electrodes before and after electrocatalysis (Figure 8). For all electrodes, the materials are diluted into carbon black and Nafion, hence elements heavier than boron are prone to absorb the B 1s photoelectrons at low kinetic energy. As a result, boron is hardly detected, except for the materials bearing the highest B content (Figures 8e and S28b). Overall, all as-prepared materials (Figure 7a) retain their electronic states upon processing of the catalytic ink in the pristine (PE) electrodes (Figures 8 and S28 with a detailed discussion).

The postcatalysis (PC) electrodes after 2 h chronoamperometry show more significant changes. For Ni-based materials, the low valence Ni contributions have vanished after catalysis to the benefit of higher BE peaks at 855.9 and 873.5 eV (Figure 8a), ascribed to nickel (oxyhydr)oxides.[38] This is in agreement with a O 1s BE peak at 531.1 eV (Figure 8f)[39] and the oxidation wave $Ni^{2+} \rightarrow Ni^{3+}$ observed by cyclic voltammetry (Figure 6a).[50] The Si region also evolves for Ni_6Si_2B, with an intense Si 2p signal appearing at BE corresponding to partially oxidized silicon (Figures S28a and 8d). The surfaces of as-prepared Co samples were already oxidized (Figure 7b spectra were acquired after argon sputtering to remove part of the oxidized layer), and electrode processing did not change these surface states (Figure 8b).[54] After 2 h CA, the high valence Co peak shows a new and predominant contribution at lower BE (780.5 eV), which indicates the prevalence of Co^{2+} over Co^{3+} species.[55] This might indicate oxidation during catalysis of subsurface cobalt, originally belonging to the borosilicide with a close-to-elemental state. Analogously, Fe- and Mn-based samples show metal 2p states with high energy multiplets indicative of strong surface oxidation (Figures 8c and S29).[56] Again, the O 1s spectra (Figure S30) of the Co, Fe, and Mn borosilicide electrodes after electrocatalysis show a peak at 530.9 eV, which suggests the formation of metal oxyhydroxide during OER,[55] in line with previous studies on Co-based[57] and Fe-based OER catalysts.[58] The Si 2p windows indicate increased presence of oxidized SiO_x species (102.2 eV) on all postcatalysis borosilicides (Figure 8d). During the oxyhydroxide layer formation, the surface Si content increases, and Si integrates the oxyhydroxide layer.

OER Electrocatalytic Properties of Transition Metal Borosilicides vs Respective Binary Compounds. EIS, SEM, and XPS show that during water oxidation electrocatalysis, the surface of borosilicide particles evolves into metal oxyhydroxide-like phases, which act as the actual catalytic species, as already discussed for binary compounds.[50,59,60] Therefore, borosilicides, silicides, and borides are precatalysts, to form in situ the active surface species in oxidative conditions.

While the poor OER activity and stability of Mn_5SiB_2 can be ascribed to its complete oxidation and formation of an insulating (oxyhydr)oxide layer, in agreement with EIS, the relative activity ranking where the Ni_6Si_2B-derived catalyst appears after activation very active versus state-of-the-art materials (Table S5), more active and more stable than $Co_{4.75}Si_2B$ and Fe_5SiB_2-derived materials (Figure 6a,d), merits further questioning. For $Co_{4.75}Si_2B$ and Fe_5SiB_2 electrodes, the activity loss upon operation (Figure 6d) is correlated with a strong increase in the charge transfer resistance (Table S7), which increases much less for the Ni_6Si_2B electrode. We thus propose that although the catalytic properties of the oxyhydroxide layers on the $Co_{4.75}Si_2B$ and Fe_5SiB_2 electrodes may provide more favorable OER kinetics (lower adsorption resistance values, Table S7), it is not enough to counterbalance the loss of electrical conductivity within the catalyst film as the oxyhydroxide layer grows. Hence, the superior electrocatalytic activity and stability of Ni_6Si_2B-based electrodes relate at least in part to its resistance to corrosion. The electron back-donation effect we have unveiled specifically for Ni_6Si_2B results in enrichment of the 3d states of nickel, which stabilizes nickel versus oxidation processes,[5,49] and then restrains the growth of the oxyhydroxide layer to maintain electrocatalytic properties during electrocatalysis. Likewise, Ni_6Si_2B is the only borosilicide examined herein that comprises both B−B and Si−Si covalent bonds (Figure 1). This bonding scheme enhances the stability of the material during operation and hence resistance to corrosion.

Ni_6Si_2B and $Co_{4.75}Si_2B$-based electrodes exhibit an OER activity significantly higher than their binary compound counterparts (Figure 6a). Back-donation explains the higher current density achieved for Ni_6Si_2B and Ni_3B, compared to nickel silicides, which are more prone to oxidation and loss of charge transport properties. However, this cannot account for the higher ECSA-normalized activity of Ni_6Si_2B compared to Ni_3B and to the binary reaction intermediates. Likewise, the cobalt borosilicide shows also higher activity than its binary counterparts, while it does not present back-donation, so that the higher performances achieved by combining Si and B together in a single compound must originate from additional effects. Masa and co-workers observed a strong influence from the Ni−Ni distance in pristine binary nickel-*p*-block element compounds on the apparent OER activation energy.[42] It is unlikely that the crystal structure of the pristine compound may impact the structure of a thick oxyhydroxide catalytic layer obtained for the Co-based electrodes, propagating over more than 50 nm as we observed previously for CoSi.[10] On the contrary, borate and silicate species may modify the local structure of the surface oxyhydroxide layers. In the case of cobalt silicide, we recently evidenced that the silicide gets oxidized in situ by providing silicate units. The latter dope the oxyhydroxide layer and brings additional flexibility to the catalytic layer to better bind reaction intermediates.[10] Similar effects have been evidenced for borate doping of nickel compounds.[21] In all cases, the rate-determining step is the *OOH formation, borates and silicates decreasing its activation energy by bringing flexibility to the oxyhydroxide layer. EIS,

SEM, and XPS show that oxidation of the borosilicides yields borate and silicate species that we detect as dopants within the oxyhydroxide-like layers. We therefore postulate that combining these BO_x and SiO_x units brings additional structural flexibility to the metal oxyhydroxide catalytic layer, thus further enhancing OER kinetics and performances compared to the binary compounds.

CONCLUSIONS

By designing reactions in molten salts, we have unveiled a general redox route toward transition metal borosilicides. The involved reaction pathways combine intermediate binary silicides and borides toward the complex crystal structures of borosilicides. In all cases, we observe that the more covalent metal boride coordination units act as building blocks for ultimate borosilicides. One can then envision applying these guidelines to explore and design new ternary compounds by considering corresponding binary phases as structural templates.

In the specific case of a nickel borosilicide, we provide evidence of a back-donation effect from boron to nickel atoms that was previously described only in binary borides. The resulting electronic enrichment of the Ni 3d band and the unique crystal structure merging covalent boron and silicon networks have a deep impact on the water oxidation electrocatalytic activity and stability. Indeed, they hinder oxidation of nickel atoms, hence retaining the metallic behavior of the borosilicide to ensure efficient charge transfer within the operating electrode. Besides charge transport properties, borosilicides offer the ability to precisely tune the catalytic properties of oxidized layers formed in situ, by enabling codoping of these layers with borate and silicate structural units and then by adjusting water oxidation kinetics. Therefore, the use of multielement compounds as single-source precatalysts opens new avenues for the design of electrocatalysts.

EXPERIMENTAL METHODS

Reagents and references are detailed in Supporting information, with the synthesis protocols for binary reference solids.

Synthesis of Ternary Transition Metal Borosilicides. *Synthesis of Ni_6Si_2B.* 129.6 mg (1 mmol) of $NiCl_2$, 17.0 mg (0.33 mmol) of Na_4Si_4, 8.8 mg (0.23 mmol) of $NaBH_4$, 34.4 mg (1.43 mmol) of NaH, and 1.25 g of eutectic LiCl-KCl mixture were ball-milled (Retsch MM400 ball mill airtight vial of 50 mL, with one steel ball of 62.3 g and a diameter of 23 mm) under an Ar atmosphere for 2 min at 20 Hz. The homogeneous mixture was then transferred into a glassy carbon crucible (Ø10 × H200 mm^2). The crucible was placed in a bottom closed quartz tube connected to a Schlenk line under Ar flow. In a vertical furnace (Eraly), the reaction mixture was heated at 10 °C·min^{-1} to 650 °C and kept for 90 min before cooling to room temperature naturally. The product-salt mixture was subsequently washed in 10−15 cycles of centrifugation/redispersion in methanol until the conductivity of the supernatant dropped below 3 $\mu S \cdot cm^{-1}$. Big chunks of salt-product mixture required preliminary grinding in order to speed up the washing step due to the low solubility of LiCl-KCl in methanol. The washed powders were dried under a vacuum at room temperature overnight and stored in an Ar-filled glovebox.

The **synthesis of $Co_{4.75}Si_2B$** was performed in a way similar to the one described above, with 129.8 mg (1 mmol) of $CoCl_2$, 21.5 mg (0.42 mmol) of Na_4Si_4, 8.8 mg (0.23 mmol) of $NaBH_4$, 32.3 mg (1.35 mmol) of NaH and 1.25 g of eutectic LiCl-KCl mixture, a reaction temperature of 1200 °C for 8 h. **Fe_5SiB_2** was synthesized using 126.8 mg (1 mmol) of $FeCl_2$, 10.2 mg (0.20 mmol) of Na_4Si_4, 15.1 mg (0.40 mmol) of $NaBH_4$, 67.2 mg (2.80 mmol) of NaH, and 1.25 g of eutectic LiCl-KCl mixture with a reaction temperature of 800 °C for 2 h. **Mn_5SiB_2** was synthesized using 251.7 mg (2 mmol) of $MnCl_2$, 20.4 mg (0.40 mmol) of Na_4Si_4, 30.3 mg (0.80 mmol) of $NaBH_4$, 67.2 mg (2.80 mmol) of NaH, and 2.5 g of a eutectic LiCl-KCl mixture with a reaction temperature of 850 °C for 4 h.

Synthesis of Reaction Intermediates. The reaction intermediates were prepared following the same procedures as those for the corresponding ternary compounds, but the reaction temperature and dwell time were lowered below the temperature threshold of the ternary compound formation. To obtain the **Ni-Int** sample, the Ni-based reaction was quenched at 500 °C with no dwell time. The **Co-Int**, **Fe-Int**, and **Mn-Int** samples were quenched after 4 h at 900 °C, 1 h at 700 °C, and 2 h at 450 °C, respectively.

Characterization. In situ X-ray diffraction was carried out at the ESRF synchrotron on beamline ID11, in transmission mode at an energy (wavelength) of 93.3159 keV (0.1329 Å). A Double Crystal Monochromator equipped with two Si(111) crystals was used to tune the energy. The detector was a Frelon4M 2048 × 2048 16Bit fast CCD camera. A custom-made capillary oven was used to perform transmission X-ray diffraction in situ during controlled heating of the reaction mixture in a 1.5 mm-diameter fused silica capillary under continuous argon flow, to mimic conditions of ex situ lab syntheses. Intermediate compounds Ni, *h*-Ni_2Si, *o*-Ni_2Si, and Ni_3B were identified through PDF cards 04-016-6268, 01-072-2547, 00-048-1339, and 04-014-0853, respectively. B−Co, Co_2Si, Co_2B, and CoB were identified using PDF cards 04-003-3863, 04-010-3523, 04-004-1666, and 04-003-2122, respectively. Fe, Fe_5Si_3, and Fe_2B were identified using PDF cards 04-007-9753, 04-016-3988, and 04-013-1639, respectively. α-Mn, Mn_5Si_3, and Mn_2B were identified using PDF cards 00-032-0637, 01-078-4965, and 00-025-0535, respectively. Refined cell parameters were obtained by Rietveld refinement with the GSAS-II software.[61]

Other characterization methods are detailed in supporting information.

Supporting information. Experimental details; synthesis conditions and additional structural and morphological characterization (Tables S1−S3, Figures S1−S4); details and interpretation of in situ XRD experiments (Figures S5−S15, Table S4); details of electrochemical studies: structural characterization of the binary reference compounds (Figure S16); electrochemical characterization (Figures S17−S19); literature survey of state-of-the-art OER electrocatalysts (Table S5); supplementary text 1 focused on ECSA and EIS measurements (Figures S20−S23, Table S6−S7); SEM and EDS characterization of pristine and postcatalysis electrodes (Figures S24−S26); supplementary text 2 providing detailed discussion of XPS data recorded for as-obtained powders (Figure S27); pristine and postcatalysis electrodes (Figures S28−S30)

Authors

David Portehault − *Laboratoire de Chimie de la Matière Condensée de Paris (LCMCP), Sorbonne Université, CNRS, F-75005 Paris, France;* orcid.org/0000-0003-4914-4913; Email: david.portehault@sorbonne-universite.fr

Daniel Janisch − *Laboratoire de Chimie de la Matière Condensée de Paris (LCMCP), Sorbonne Université, CNRS, F-75005 Paris, France*

Fernando Igoa Saldaña − *Laboratoire de Chimie de la Matière Condensée de Paris (LCMCP), Sorbonne Université, CNRS, F-75005 Paris, France*
Edouard De Rolland Dalon − *Laboratoire de Chimie de la Matière Condensée de Paris (LCMCP), Sorbonne Université, CNRS, F-75005 Paris, France*
Carlos V. M. Inocêncio − *Laboratoire de Chimie de la Matière Condensée de Paris (LCMCP), Sorbonne Université, CNRS, F-75005 Paris, France;* orcid.org/0000-0001-7632-0463
Yang Song − *Laboratoire de Chimie de la Matière Condensée de Paris (LCMCP), Sorbonne Université, CNRS, F-75005 Paris, France*
Pierre-Olivier Autran − *European Synchrotron Radiation Facility (ESRF), 38043 Grenoble, France*
Antoine Miche − *Laboratoire de Réactivité de Surface (LRS), Sorbonne Université, CNRS, F- 75005 Paris, France*
Sandra Casale − *Laboratoire de Réactivité de Surface (LRS),*

■ ACKNOWLEDGMENTS

This project has received funding from the European Research Council (ERC) Consolidator Grant GENESIS under the European Union's Horizon 2020 research and innovation program (grant agreement n°864850). Experiments at the ID11 beamline of ESRF have been funded by ESRF as the User Proposals MA4506, MA4760, and MA5188. CVMI thanks the French national agency for research (ANR) under the project HSM2 ANR-21-CE50-0021 for funding. The authors also acknowledge the FCMat platform for XPS measurements.

■ REFERENCES

(1) Shankhari, P.; Janka, O.; Pöttgen, R.; Fokwa, B. P. T. Rare-Earth-Free Magnets: Enhancing Magnetic Anisotropy and Spin Exchange Toward High-T_C $Hf_2MIr_5B_2$ (M = Mn, Fe). *J. Am. Chem. Soc.* **2021**, *143* (11), 4205−4212.
(2) Lee, E.; Fokwa, B. P. T. Nonprecious Metal Borides: Emerging Electrocatalysts for Hydrogen Production. *Acc. Chem. Res.* **2022**, *55* (1), 56−64.
(3) Bhaskar, G.; Behera, R. K.; Gvozdetskyi, V.; Carnahan, S. L.; Ribeiro, R. A.; Oftedahl, P.; Ward, C.; Canfield, P. C.; Rossini, A. J.; Huang, W.; Zaikina, J. V. Breaking New Ground: *MB*ene Route toward Selective Vinyl Double Bond Hydrogenation in Nitroarenes. *J. Am. Chem. Soc.* **2023**, *145* (50), 27459−27470.
(4) Kageyama, H.; Hayashi, K.; Maeda, K.; Attfield, J. P.; Hiroi, Z.; Rondinelli, J. M.; Poeppelmeier, K. R. Expanding Frontiers in Materials Chemistry and Physics with Multiple Anions. *Nat. Commun.* **2018**, *9* (1), No. 772.
(5) Carenco, S.; Portehault, D.; Boissière, C.; Mézailles, N.; Sanchez, C. Nanoscaled Metal Borides and Phosphides: Recent Developments and Perspectives. *Chem. Rev.* **2013**, *113* (10), 7981−8065.
(6) Lugscheider, E.; Reimann, H.; Knotek, O. Das Dreistoffsystem Nickel-Bor-Silicium. *Monatsh. Chem. - Chem. Mon.* **1975**, *106* (5), 1155−1165.
(7) Aronsson, B.; Lundgren, G. X-Ray Investigations on Me-Si-B Systems. *Acta Chem. Scand.* **1959**, *13*, 433−441.
(8) ElMeligy, T. A.; Kota, S.; Natu, V.; Lind, H.; Palisaitis, J.; Persson, P. O. Å.; Rosen, J.; Barsoum, M. W. Synthesis, Characterization, Properties, First Principles Calculations, and X-Ray Photoelectron Spectroscopy of Bulk Mn_5SiB_2 and Fe_5SiB_2 Ternary Borides. *J. Alloys Compd.* **2021**, *888*, No. 161377.
(9) Ondry, J. C.; Gupta, A.; Zhou, Z.; Chang, J. H.; Talapin, D. V. Synthesis of Ternary and Quaternary Group III-Arsenide Colloidal Quantum Dots via High-Temperature Cation Exchange in Molten Salts: The Importance of Molten Salt Speciation. *ACS Nano* **2024**, *18* (1), 858−873.
(10) Song, Y.; Gómez-Recio, I.; Ghoridi, A.; Igoa Saldaña, F.; Janisch, D.; Sassoye, C.; Dupuis, V.; Hrabovsky, D.; Ruiz-González, M. L.; González-Calbet, J. M.; Casale, S.; Zitolo, A.; Lassalle-Kaiser, B.; Laberty-Robert, C.; Portehault, D. Heterostructured Cobalt Silicide Nanocrystals: Synthesis in Molten Salts, Ferromagnetism, and Electrocatalysis. *J. Am. Chem. Soc.* **2023**, *145*, 19207.
(11) Portehault, D.; Devi, S.; Beaunier, P.; Gervais, C.; Giordano, C.; Sanchez, C.; Antonietti, M. A General Solution Route toward Metal Boride Nanocrystals. *Angew. Chem., Int. Ed.* **2011**, *50* (14), 3262−3265.
(12) Delacroix, S.; Igoa, F.; Song, Y.; Le Godec, Y.; Coelho-Diogo, C.; Gervais, C.; Rousse, G.; Portehault, D. Electron Precise Sodium Carbaboride Nanocrystals from Molten Salts: Single Sources to Boron Carbides. *Inorg. Chem.* **2021**, *60* (7), 4252−4260.
(13) Portehault, D.; Gómez-Recio, I.; Baron, M. A.; Musumeci, V.; Aymonier, C.; Rouchon, V.; Le Godec, Y. Geoinspired Syntheses of Materials and Nanomaterials. *Chem. Soc. Rev.* **2022**, *51* (11), 4828−4866.
(14) Masa, J.; Andronescu, C.; Antoni, H.; Sinev, I.; Seisel, S.; Elumeeva, K.; Barwe, S.; Marti-Sanchez, S.; Arbiol, J.; Cuenya, B. R.; Muhler, M.; Schuhmann, W. Role of Boron and Phosphorus in Enhanced Electrocatalytic Oxygen Evolution by Nickel Borides and Nickel Phosphides. *ChemElectroChem* **2019**, *6* (1), 235−240.
(15) Liu, X.; He, G.; Liu, H.; Zhu, Y.; Xiao, J.; Han, L. Boron-Doped Cobalt-Iron Bimetal Phosphides Nanosheets for Enhanced Oxygen Evolution. *J. Alloys Compd.* **2022**, *893*, No. 162208.
(16) Badruzzaman, A.; Yuda, A.; Ashok, A.; Kumar, A. Recent Advances in Cobalt Based Heterogeneous Catalysts for Oxygen Evolution Reaction. *Inorg. Chim. Acta* **2020**, *511*, No. 119854.
(17) Wang, Y.; Yan, D.; El Hankari, S.; Zou, Y.; Wang, S. Recent Progress on Layered Double Hydroxides and Their Derivatives for Electrocatalytic Water Splitting. *Adv. Sci.* **2018**, *5* (8), No. 1800064.
(18) Zhao, J.; Zhang, J.; Li, Z.; Bu, X. Recent Progress on NiFe-Based Electrocatalysts for the Oxygen Evolution Reaction. *Small* **2020**, *16* (51), No. 2003916.
(19) Yu, M.; Budiyanto, E.; Tüysüz, H. Principles of Water Electrolysis and Recent Progress in Cobalt-, Nickel-, and Iron-Based Oxides for the Oxygen Evolution Reaction. *Angew. Chem., Int. Ed.* **2022**, *61* (1), No. e202103824.
(20) Kumbhar, V. S.; Lee, H.; Lee, J.; Lee, K. Recent Advances in Water-Splitting Electrocatalysts Based on Manganese Oxide. *Carbon Resour. Convers.* **2019**, *2* (3), 242−255.
(21) Wang, N.; Xu, A.; Ou, P.; Hung, S.-F.; Ozden, A.; Lu, Y.-R.; Abed, J.; Wang, Z.; Yan, Y.; Sun, M.-J.; Xia, Y.; Han, M.; Han, J.; Yao, K.; Wu, F.-Y.; Chen, P.-H.; Vomiero, A.; Seifitokaldani, A.; Sun, X.; Sinton, D.; Liu, Y.; Sargent, E. H.; Liang, H. Boride-Derived Oxygen-Evolution Catalysts. *Nat. Commun.* **2021**, *12* (1), No. 6089.
(22) Chen, X.; Liang, C. Transition Metal Silicides: Fundamentals, Preparation and Catalytic Applications. *Catal. Sci. Technol.* **2019**, *9* (18), 4785−4820.
(23) Tian, L.; Yan, X.; Chen, X. Electrochemical Activity of Iron Phosphide Nanoparticles in Hydrogen Evolution Reaction. *ACS Catal.* **2016**, *6* (8), 5441−5448.
(24) Xiao, P.; Sk, M. A.; Thia, L.; Ge, X.; Lim, R. J.; Wang, J.-Y.; Lim, K. H.; Wang, X. Molybdenum Phosphide as an Efficient Electrocatalyst for the Hydrogen Evolution Reaction. *Energy Environ. Sci.* **2014**, *7* (8), 2624−2629.
(25) Dutta, A.; Samantara, A. K.; Dutta, S. K.; Jena, B. K.; Pradhan,

(26) Kim, J.-H.; Kawashima, K.; Wygant, B. R.; Mabayoje, O.; Liu, Y.; Wang, J. H.; Mullins, C. B. Transformation of a Cobalt Carbide (Co_3C) Oxygen Evolution Precatalyst. *ACS Appl. Energy Mater.* **2018**, DOI: 10.1021/acsaem.8b01336.
(27) Wan, C.; Regmi, Y. N.; Leonard, B. M. Multiple Phases of Molybdenum Carbide as Electrocatalysts for the Hydrogen Evolution Reaction. *Angew. Chem.* **2014**, *126* (25), 6525−6528.
(28) Chen, P.; Ye, J.; Wang, H.; Ouyang, L.; Zhu, M. Recent Progress of Transition Metal Carbides/Nitrides for Electrocatalytic Water Splitting. *J. Alloys Compd.* **2021**, *883*, No. 160833.
(29) Swesi, A. T.; Masud, J.; Nath, M. Nickel Selenide as a High-Efficiency Catalyst for Oxygen Evolution Reaction. *Energy Environ. Sci.* **2016**, *9* (5), 1771−1782.
(30) Fang, Z.; Peng, L.; Lv, H.; Zhu, Y.; Yan, C.; Wang, S.; Kalyani, P.; Wu, X.; Yu, G. Metallic Transition Metal Selenide Holey Nanosheets for Efficient Oxygen Evolution Electrocatalysis. *ACS Nano* **2017**, *11* (9), 9550−9557.
(31) Singh, H.; Marley-Hines, M.; Chakravarty, S.; Nath, M. Multi-Walled Carbon Nanotube Supported Manganese Selenide as a Highly Active Bifunctional OER and ORR Electrocatalyst. *J. Mater. Chem. A* **2022**, *10* (12), 6772−6784.
(32) Trotochaud, L.; Young, S. L.; Ranney, J. K.; Boettcher, S. W. Nickel−Iron Oxyhydroxide Oxygen-Evolution Electrocatalysts: The Role of Intentional and Incidental Iron Incorporation. *J. Am. Chem. Soc.* **2014**, *136* (18), 6744−6753.
(33) Wang, X.; Zuo, Y.; Horta, S.; He, R.; Yang, L.; Ostovari Moghaddam, A.; Ibáñez, M.; Qi, X.; Cabot, A. CoFeNiMnZnB as a High-Entropy Metal Boride to Boost the Oxygen Evolution Reaction. *ACS Appl. Mater. Interfaces* **2022**, *14* (42), 48212−48219.
(34) Jose, V.; Nsanzimana, J. M. V.; Hu, H.; Choi, J.; Wang, X.; Lee, J. Highly Efficient Oxygen Reduction Reaction Activity of N-Doped Carbon−Cobalt Boride Heterointerfaces. *Adv. Energy Mater.* **2021**, *11* (17), No. 2100157.
(35) Song, X.; Liu, X.; Wang, H.; Guo, Y.; Wang, Y. Improved Performance of Nickel Boride by Phosphorus Doping as an Efficient Electrocatalyst for the Oxidation of 5-Hydroxymethylfurfural to 2,5-Furandicarboxylic Acid. *Ind. Eng. Chem. Res.* **2020**, *59* (39), 17348−17356.
(36) Sun, H.; Xu, X.; Yan, Z.; Chen, X.; Jiao, L.; Cheng, F.; Chen, J. Superhydrophilic Amorphous Co−B−P Nanosheet Electrocatalysts with Pt-like Activity and Durability for the Hydrogen Evolution Reaction. *J. Mater. Chem. A* **2018**, *6* (44), 22062−22069.
(37) Hu, G.; Xiang, J.; Li, J.; Liu, P.; Ali, R. N.; Xiang, B. Urchin-like Ternary Cobalt Phosphosulfide as High-Efficiency and Stable Bifunctional Electrocatalyst for Overall Water Splitting. *J. Catal.* **2019**, *371*, 126−134.
(38) Kumar, R.; Bahri, M.; Song, Y.; Gonell, F.; Thomas, C.; Ersen, O.; Sanchez, C.; Laberty-Robert, C.; Portehault, D. Phase Selective Synthesis of Nickel Silicide Nanocrystals in Molten Salts for Electrocatalysis of the Oxygen Evolution Reaction. *Nanoscale* **2020**, *12* (28), 15209−15213.
(39) Song, Y.; Casale, S.; Miche, A.; Montero, D.; Laberty-Robert, C.; Portehault, D. Converting Silicon Nanoparticles into Nickel Iron Silicide Nanocrystals within Molten Salts for Water Oxidation Electrocatalysis. *J. Mater. Chem. A* **2022**, *10* (3), 1350−1358.
(40) Burdett, J. K.; Canadell, Enric.; Miller, G. J. Electronic Structure of Transition-Metal Borides with the AlB_2 Structure. *J. Am. Chem. Soc.* **1986**, *108* (21), 6561−6568.
(41) Errandonea, D.; Santamaría-Perez, D.; Vegas, A.; Nuss, J.; Jansen, M.; Rodríguez-Hernandez, P.; Muñoz, A. Structural Stability of Fe_5Si_3 and Ni_2Si Studied by High-Pressure x-Ray Diffraction and *Ab Initio* Total-Energy Calculations. *Phys. Rev. B* **2008**, *77* (9), No. 094113.
(42) Masa, J.; Piontek, S.; Wilde, P.; Antoni, H.; Eckhard, T.; Chen, Y.; Muhler, M.; Apfel, U.; Schuhmann, W. Ni-Metalloid (B, Si, P, As, and Te) Alloys as Water Oxidation Electrocatalysts. *Adv. Energy Mater.* **2019**, *9*, No. 1900796.
(43) McCrory, C. C. L.; Jung, S.; Peters, J. C.; Jaramillo, T. F. Benchmarking Heterogeneous Electrocatalysts for the Oxygen Evolution Reaction. *J. Am. Chem. Soc.* **2013**, *135* (45), 16977−16987.
(44) Spöri, C.; Brand, C.; Kroschel, M.; Strasser, P. Accelerated Degradation Protocols for Iridium-Based Oxygen Evolving Catalysts in Water Splitting Devices. *J. Electrochem. Soc.* **2021**, *168* (3), No. 034508.
(45) Lu, Y.; Wang, W.; Xie, F. Investigation of Oxygen Evolution Reaction Kinetic Process and Kinetic Parameters on Iridium Electrode by Electrochemistry Impedance Spectroscopy Analysis. *J. Electroanal. Chem.* **2020**, *871*, No. 114281.
(46) Qi, J.; Zhang, W.; Xiang, R.; Liu, K.; Wang, H.; Chen, M.; Han, Y.; Cao, R. Porous Nickel−Iron Oxide as a Highly Efficient Electrocatalyst for Oxygen Evolution Reaction. *Adv. Sci.* **2015**, *2* (10), No. 1500199.
(47) Hollinger, G. Structures Chimique et Electronique de l'interface SiO_2-Si. *Appl. Surf. Sci.* **1981**, *8* (3), 318−336.
(48) Gouget, G.; Debecker, D. P.; Kim, A.; Olivieri, G.; Gallet, J.-J.; Bournel, F.; Thomas, C.; Ersen, O.; Moldovan, S.; Sanchez, C.; Carenco, S.; Portehault, D. In Situ Solid−Gas Reactivity of Nanoscaled Metal Borides from Molten Salt Synthesis. *Inorg. Chem.* **2017**, *56* (15), 9225−9234.
(49) Diplas, S.; Løvvik, O. M. Electronic Structure Studies of Ni−X (X: B, S, P) Alloys Using x-Ray Photoelectron Spectroscopy, x-Ray Induced Auger Electron Spectroscopy and Density Functional Theory Calculations. *J. Phys.: Condens.Matter* **2009**, *21* (24), No. 245503.
(50) Masa, J.; Sinev, I.; Mistry, H.; Ventosa, E.; De La Mata, M.; Arbiol, J.; Muhler, M.; Roldan Cuenya, B.; Schuhmann, W. Ultrathin High Surface Area Nickel Boride (Ni_xB) Nanosheets as Highly Efficient Electrocatalyst for Oxygen Evolution. *Adv. Energy Mater.* **2017**, *7* (17), No. 1700381.
(51) Schreifels, J. X-Ray Photoelectron Spectroscopy of Nickel Boride Catalysts: Correlation of Surface States with Reaction Products in the Hydrogenation of Acrylonitrile. *J. Catal.* **1980**, *65* (1), 195−206.
(52) Gouin, X.; Grange, P.; Bois, L.; L'Haridon, P.; Laurent, Y. Characterization of the Nitridation Process of Boric Acid. *J. Alloys Compd.* **1995**, *224* (1), 22−28.
(53) Cha, S.; Lee, E.; Cho, G. Fabrication of Poly(3,4-Ethylenedioxythiophene):Poly(Styrenesulfonate)/Poly(Vinylidene Fluoride) Nanofiber-Web-Based Transparent Conducting Electrodes for Dye-Sensitized Photovoltaic Textiles. *ACS Appl. Mater. Interfaces* **2021**, *13* (24), 28855−28863.
(54) Biesinger, M. C.; Payne, B. P.; Grosvenor, A. P.; Lau, L. W. M.; Gerson, A. R.; Smart, R. St. C. Resolving Surface Chemical States in XPS Analysis of First Row Transition Metals, Oxides and Hydroxides: Cr, Mn, Fe, Co and Ni. *Appl. Surf. Sci.* **2011**, *257* (7), 2717−2730.
(55) Yang, J.; Liu, H.; Martens, W. N.; Frost, R. L. Synthesis and Characterization of Cobalt Hydroxide, Cobalt Oxyhydroxide, and Cobalt Oxide Nanodiscs. *J. Phys. Chem. C* **2010**, *114* (1), 111−119.
(56) Joyner, D. J.; Johnson, O.; Hercules, D. M. A Study of the Iron Borides. 1. Electron Spectroscopy. *J. Am. Chem. Soc.* **1980**, *102* (6), 1910−1917.
(57) Masa, J.; Weide, P.; Peeters, D.; Sinev, I.; Xia, W.; Sun, Z.; Somsen, C.; Muhler, M.; Schuhmann, W. Amorphous Cobalt Boride (Co_2B) as a Highly Efficient Nonprecious Catalyst for Electrochemical Water Splitting: Oxygen and Hydrogen Evolution. *Adv. Energy Mater.* **2016**, *6* (6), No. 1502313.
(58) Hausmann, J. N.; Beltrán-Suito, R.; Mebs, S.; Hlukhyy, V.; Fässler, T. F.; Dau, H.; Driess, M.; Menezes, P. W. Evolving Highly Active Oxidic Iron(III) Phase from Corrosion of Intermetallic Iron Silicide to Master Efficient Electrocatalytic Water Oxidation and Selective Oxygenation of 5-Hydroxymethylfurfural. *Adv. Mater.* **2021**, *33* (27), No. 2008823.
(59) Mondal, I.; Hausmann, J. N.; Vijaykumar, G.; Mebs, S.; Dau, H.; Driess, M.; Menezes, P. W. Nanostructured Intermetallic Nickel Silicide (Pre)Catalyst for Anodic Oxygen Evolution Reaction and Selective Dehydrogenation of Primary Amines. *Adv. Energy Mater.* **2022**, *12* (25), No. 2200269.

(60) Klemenz, S.; Schuch, J.; Hawel, S.; Zieschang, A.-M.; Kaiser, B.; Jaegermann, W.; Albert, B. Synthesis of a Highly Efficient Oxygen-Evolution Electrocatalyst by Incorporation of Iron into Nanoscale Cobalt Borides. *ChemSusChem* **2018**, *11* (18), 3150−3156.
(61) Toby, B. H.; Von Dreele, R. B. *GSAS-II*: The Genesis of a Modern Open-Source All Purpose Crystallography Software Package. *J. Appl. Crystallogr.* **2013**, *46* (2), 544−549.

Covalent transition metal borosilicides: reaction pathways in molten salts for water oxidation electrocatalysis

Daniel Janisch [a], Fernando Igoa Saldaña [a], Edouard De Rolland Dalon [a], Carlos V. M. Inocêncio,[a] Yang Song [a], Pierre-Olivier Autran [b], Antoine Miche [c], Sandra Casale [c] and David Portehault [a]

[a] *Sorbonne Université, CNRS, Laboratoire de Chimie de la Matière Condensée de Paris (LCMCP), 4 place Jussieu, F-75005 Paris, France*

[b] *European Synchrotron Radiation Facility (ESRF), 71 avenue des Martyrs, 38043 Grenoble Cedex 9, France*

[c] *Sorbonne Université, CNRS, Laboratoire de Réactivité de Surface (LRS), 4 place Jussieu, F- 75005 Paris, France*

Corresponding author: david.portehault@sorbonne-universite.fr

SUPPLEMENTARY INFORMATION

Reagents and references

All reagents were stored and handled in an argon-filled glove box. Metal chlorides were the metal sources used as received: $NiCl_2$ (99% anhydrous, Alfa Aesar), $CoCl_2$ (99.9% AnhydroBeads, Sigma Aldrich), CoI_2 (99.5% anhydrous, Alfa Aesar), $FeCl_2$ (99.5% anhydrous, Alfa Aesar) and $MnCl_2$ (>99%, Sigma Aldrich and self-dried). $NaBH_4$ (98 % min., Alfa Aesar) and NaH (90 %, Aldrich) were also used as received. Na_4Si_4 was prepared following the procedure of Song et al.[1] A eutectic mixture 45:55 wt. % of LiCl (99.9% anhydrous Alfa Aesar) and KCl (99.9% anhydrous Sigma Aldrich) served as solvent. MeOH (VWR Normapur grade) was used for washing steps after synthesis. NiO (99.9% purity powder, Sigma Aldrich), Co_3O_4 (Sigma Aldrich), FeO/Fe_2O_3 (97% nanopowder 50-100nm, Sigma Aldrich), Mn_2O_3 (99.99% purity, Sigma Aldrich), silicon nanoparticles (99% 40 nm, Nanomakers© France), Boron (>95% amorphous powder <1 μm, Sigma Aldrich) and B_6Si (98% purity, Alfa Aesar) were used as references for electrocatalytic measurements.

Synthesis of binary transition metal silicides (TM-Si) and transition metal borides (TM-B)

Ni_3B was prepared by first dispersing 100 mg (1.7 mmol) of nickel nanoparticles, produced by a previously reported method [2] in 1.6 mL anhydrous hexane in inert atmosphere and adding 5 g of eutectic LiI-KI mixture. After 15 min sonication the mixture was dried, followed by ball-milling with 27 mg $NaBH_4$ for 2 min at 20 Hz and heating in a passivated Mo-crucible at 475 °C for 90 min under Ar flow. Washing of the product-salt mixture was done analogously as the synthesis of borosilicide samples.

Ni_2Si was synthesised following the procedure developed by Song et al.[3] **Co_2B** was synthesised as described above for borosilicide samples, by reacting 129.8 mg (1 mmol) of $CoCl_2$, 24.6 mg (0.7 mmol) $NaBH_4$ and 32.4 mg (1.4 mmol) NaH in 1.25 g LiCl-KCl at 750 °C for 2 h. Similarly, **CoSi** was synthesised by reacting 312.7 mg (1 mmol) of CoI_2, 25.5 mg (0.5 mmol) Na_4Si_4 and 36 mg (1.5 mmol) NaH in 1.25 g LiCl-KCl at 750 °C for 2 h. **FeB** (α-FeB) was synthesised following the procedure developed by Igoa Saldaña et al.[4] **FeSi** was synthesised following the procedure reported by Song *et al.*[3]

Characterization

Powder X-ray diffraction patterns were collected in a Bruker D8 Discover diffractometer, working under a θ-θ Bragg-Brentano configuration. The X-ray source consisted of a sealed Cu anode with emission lines $K_{\alpha 1}$ and $K_{\alpha 2}$, with an acceleration tension of 40 kV and a current of 30 mA. The Diffracted X-ray intensity was detected using a LynxEye linear detector. To avoid a potential oxidation of the samples, the samples were stored and prepared in an Ar-filled glove box and the analyses were performed in airtight specimen holders, with a protective PMMA dome. Ni_6Si_2B, $Co_{4.75}Si_2B$, Fe_5SiB_2 and Mn_5SiB_2 structures were identified according to the PDF-4+ database through PDF cards 04-001-6497, 04-012-5335, 01-084-7462 and 04-005-3275, respectively. CoSi, Co_2B, Si references were taken from the PDF-4+(2022) database through PDF cards 00-050-1337, 04-004-1666 and 00-005-0565. Rietveld refinements were performed using the GSAS-II software.[5]

Scanning electron microscopy (SEM) was performed on a SU-70 Hitachi FESEM. The acceleration voltage was set to 20 kV for secondary electron acquisition (SE) or for back scattered electron acquisition (BSE), noted as SE (U, LA100). For **energy-dispersive X-ray spectroscopy (EDS)** the acceleration voltage was set to 5 keV.

Transmission electron microscopy (TEM) images were acquired on a Tecnai Spirit 2 microscope, equipped with a LaB_6 electron gun operating at 120 kV. The samples were prepared by depositing a drop of methanolic suspension on carbon coated Cu grids under air. High-resolution transmission electron microscopy (HRTEM) was carried out on a JEOL JEM 2100Plus LaB_6 microscope operating at 200 kV with a spatial punctual resolution of 1.8 Å equipped with X-ray Energy Dispersive Spectroscopy (EDS) for chemical analysis.

X-ray photoelectron spectroscopy (XPS) analyses were performed on an Omicron Argus X-ray photoelectron spectrometer, equipped with a monochromated Al-Kα radiation source (1486.6 eV). The emission of photoelectrons from the sample was analysed at a take-off angle of 45° under ultra-high vacuum conditions (≤10−9 mBar). Spectra were recorded with a 100 eV pass energy for the survey scan and 20 eV pass energy for core levels regions. Element peak intensities were corrected by Scofield factors. The peak areas were determined after subtraction of a U 2 Tougaard

background. Binding energies were calibrated against the C 1s (C-C) binding energy at 284.8 eV. The spectra were fitted using the Thermo Scientific™ Avantage software by applying a gaussian/lorentzian ratio equal to 70/30 for deconvolution.

Preparation of electrodes. The electrodes were loaded with the samples by drop casting. 3.5 mg of sample and 3.5mg of acetylene black (CB, Super P Alfa Aesar) were sonicated in 480 µL of absolute ethanol for 30 min, followed by adding 20 µL of Nafion solution (5 % in alcohols and water, Sigma-Aldrich) for another 30 min of sonication. The CB powder was previously treated in nitric acid, by dispersing 500 mg of acetylene black in a 50 mL of 20% HNO_3 at 80 °C overnight under stirring, followed by centrifugation, washing with water and vacuum drying [6]. The well-dispersed ink was then dropped onto a freshly polished RDE to obtain a catalyst loading of 250 $\mu g_{catalyst} \cdot cm^{-2}_{electrode}$. The electrode was left to dry under air for 15 min. The GC plates were loaded with 175 $\mu g_{catalyst} \cdot cm^{-2}_{electrode}$ where the surface carrying sample was limited to 1 cm x 1 cm.

Preparation of Fe-free KOH electrolyte. The preparation of a purified KOH (Fe-free) was carried out following the procedure of Trotochaud et al.[7] 2 g of $Ni(NO_3)_2.6H_2O$ were dissolved in 4mL purified H_2O (18 MΩ) and $Ni(OH)_2$ precipitated by adding 20 mL 1M KOH and centrifugated. The $Ni(OH)_2$ was then washed three times with 20 mL purified H_2O and 2 mL 1M KOH. Then 50 mL of 1 M KOH was sonicated together with the purified $Ni(OH)_2$ and let to settle overnight. After centrifugation, 50 mL of Fe-free 1M KOH was diluted to obtain 500 mL of Fe-free 0.1M KOH.

Electrochemical measurements were carried out using a typical three-electrode configuration, with the sample as working electrode (WE), a glassy carbon (GC) rod as counter electrode (CE) and an Ag/AgCl saturated KCl electrode as reference electrode (RE). Two different substrates employed as WE were used for different measurements: a glassy carbon rotating disk electrode (RDE) with a diameter of 5 mm was used for cyclic voltammetry (CV), linear sweep voltammetry (LSV) rotating at 1600 rpm. GC substrates (HTW, 10x10x0.5 mm) were used for chronoamperometry (CA) measurements, that were subsequently used for post-electrocatalysis characterisation. Cyclic voltammograms (CV) were recorded in the potential range of 0.036 to 1.036 V vs. Ag/AgCl reference electrode (1 to 2 V vs RHE) at a scan rate of 20 mV s^{-1}. For the

CA measurements the potential was set to 1.036 V vs. Ag/AgCl (2 V vs. RHE) and the electrolyte stirred at 300 rpm to enhance the ion diffusion. The electrolyte was bubbled with O_2 for at least 20 min before the experiment and continuously during the measurement. For the potentials reported in this work, the ohmic drop iR was corrected by considering the total impedance measured at a frequency of 50 kHz as the solution resistance. The measured potentials were converted by the equation: $E_{RHE} = E_{measured} + 0.197 + 0.0591 \times$ pH, where pH = 13 for the 0.1 M KOH electrolyte.

The **electrochemical surface area (ECSA)** was determined through CV measurements at scan rates 40, 20, 10 and 5 mV s^{-1} in the potential range 0.2 to 0.4 V vs. Ag/AgCl reference electrode (1.16-1.36 V vs. RHE) while Ar was bubbled through the electrolyte. The current density (= cathodic current - anodic current) in the middle of the potential window (0.3 V vs. Ag/AgCl reference electrode = 1.26 V vs. RHE) was taken from the 5th cycle, and is linearly dependent on the scan rate. Its slope yields the double layer capacitance (C_{DL}) that constitutes a quantitative indicator for the surface area accessible to electrolyte ions. To estimate the electrochemical surface area, C_{DL} is divided by the specific capacitance value C_S = 40 µF cm^{-2}, as is generally assumed for intermetallic compounds [8,9].

Table S1. Reaction conditions applied to obtained ternary transition metal borosilicides

	This work	Previously reported conditions	Previously reported methods	Reference
Ni_6Si_2B	650 °C, 1.5 h	850 °C, 24-200 h	Induction melting	[10]
$Co_{4.75}Si_2B$	1200 °C, 8 h	1000 °C, 48 h	Arc-melting/Sintering	[11]
Fe_5SiB_2	800 °C, 2 h	1000 °C, 336 h	Arc-melting/Sintering	[12]
		1150 °C, 3 h, 36 MPa	High pressure sintering	[13]
Mn_5SiB_2	850 °C, 4 h	1000 °C, 50 h	Arc-melting/Sintering	[14]
		1250 °C, 3 h, 36 MPa	High pressure sintering	[13]

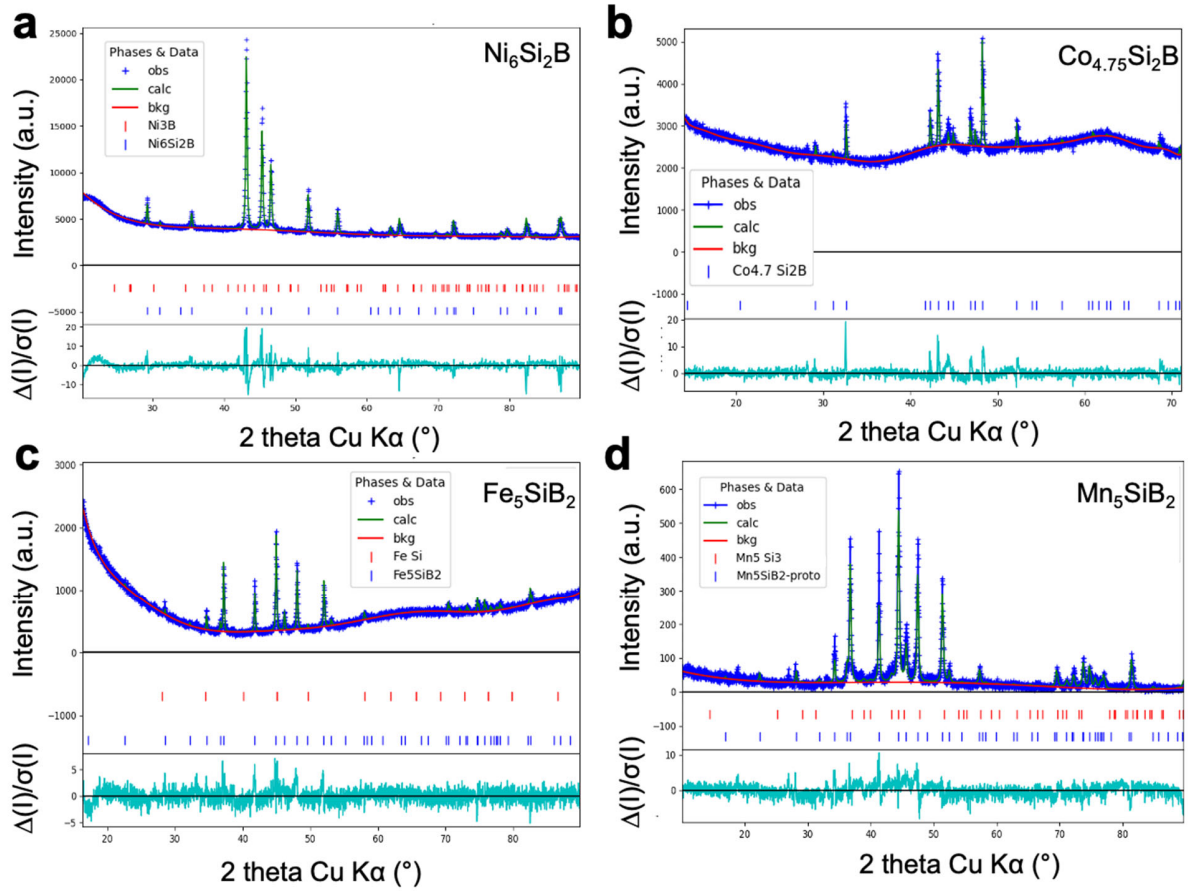

Figure S1. Rietveld analysis of the powder XRD patterns for (a) Ni_6Si_2B, (b) $Co_{4.75}Si_2B$, (c) Fe_5SiB_2 and (d) Mn_5SiB_2. The diffraction pattern of $Co_{4.75}Si_2B$ (c) shows an unusual background, that can be explained by low sample quantity, scattering by the sample holder and fluorescence of cobalt under incident Cu Kα radiation.

Table S2. Details of the Rietveld refinements of the powder XRD patterns of borosilicides shown in **Figure S1.**

Sample	Phase	Refined lattice parameters (Å)	Reference lattice parameters (Å)	Reference PDF-4+ Database (2022)	Crystall-ite size (nm)	Phase fraction (wt%)	Reliability coefficients
Ni_6Si_2B	Ni_6Si_2B (*P*-62*m*)	*a*=6.111 *c*=2.884 *Vol*=93.252	*a*=6.1050 *c*=2.8950 *Vol*=93.444	04-001-6497	66	99	χ^2 = 6.5 wR = 3.9
	Impurity: Ni_3B (*Pnma*)	*a*=5.189 *b*=6.670 *c*=4.312 *Vol*=149.239	*a*=5.2105 *b*=6.6174 *c*=4.304 *Vol*=151.381	04-003-1948	43		
$Co_{4.75}Si_2B$	$Co_{4.75}Si_2B$ (*I*4/*mcm*)	*a*=8.648 *c*=4.265 *Vol*=318.945	*a*=8.6150 *c*=4.2500 *Vol*=315.427	04-012-5335	190	>99	χ^2 = 2.8 wR = 3.3
Fe_5SiB_2	Fe_5SiB_2 (*I*4/*mcm*)	*a*=5.555 *c*=10.342 *Vol*=319.168	*a*=5.5541 *c*=10.3429 *Vol*=319.058	01-084-7462	114	99	χ^2 = 5.1 wR = 1.8
	Impurity: FeSi ($P2_13$)	*a*=4.495 *Vol*=90.817	*a*=4.4964 *Vol*=90.8908	00-038-1397	100		
Mn_5SiB_2	Mn_5SiB_2 (*I*4/*mcm*)	*a*=5.619 *c*=10.458 *Vol*=330.173	*a*=5.6090 *c*=10.4770 *Vol*=329.616	04-005-3275	55	95	χ^2 = 3.1 wR = 27.6
	Impurity: Mn_5Si_3 ($P6_3/mcm$)	*a*=7.067 *c*=4.851 *Vol*=209.846	*a*=6.8980 *c*=4.8020 *Vol*=197.879	01-078-4965	20		

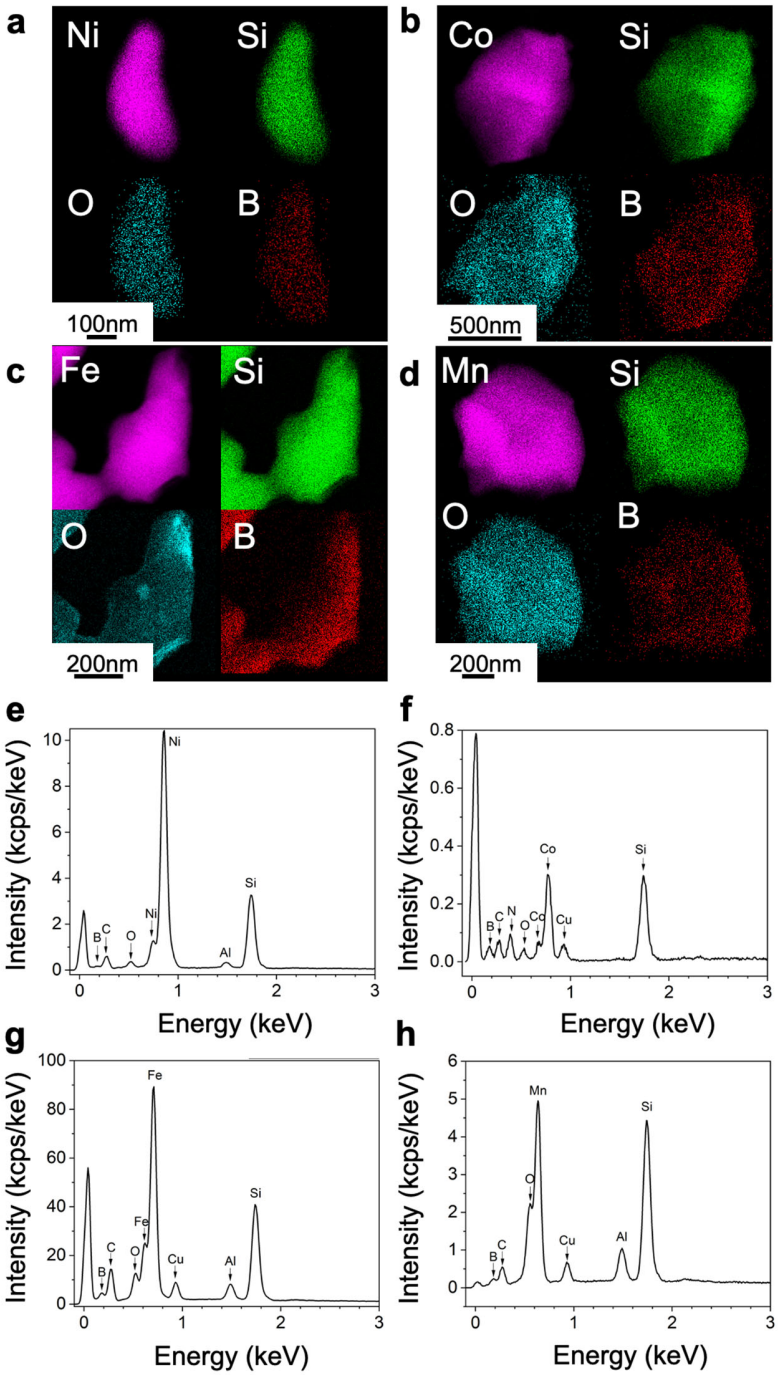

Figure S2. STEM-EDS maps of (a) Ni_6Si_2B, (b) $Co_{4.75}Si_2B$, (c) Fe_5SiB_2 and (d) Mn_5SiB_2, with respective EDS spectra (e-h). Detected copper stems from the carbon coated Cu-grid used as TEM support.

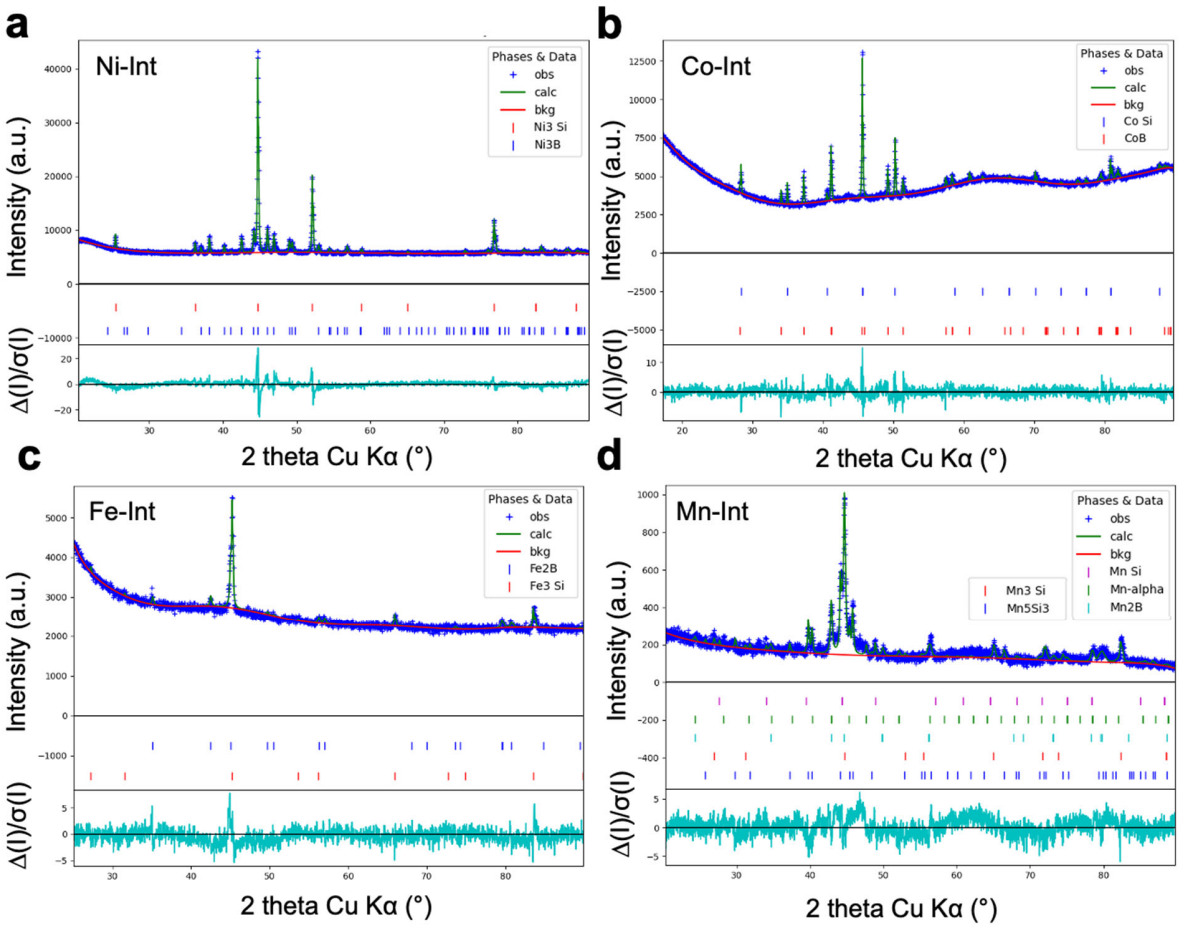

Figure S3. Rietveld refinements of the XRD patterns recorded for the powders obtained from prematurely quenched reactions. (a) **Ni- Int**, (b) **Co-Int**, (c) **Fe-Int**, (d) **Mn-Int** were quenched respectively at 500 °C and 0 h dwell time, 900 °C after 4 h, 700 °C after 1 h and at 450°C after 2 h.

Table S3. Details of the Rietveld refinements of the powder XRD patterns of reaction intermediates (TM-Int) shown in **Figure S3**.

Sample	Phase	Refined lattice parameters (Å)	Reference lattice parameters (Å)	Reference PDF-4+ Database (2022)	Cryst allite size (nm)	Phase fraction (wt%)	Phase fraction (mol%)	Reliability coefficient
Ni-Int	Ni_3B (P*nma*)	*a*=5.221 *b*=6.615 *c*=4.394 *Vol*=151.750	*a*=5.2105 *b*=6.6174 *c*=4.3904 *Vol*=151.381	04-003-1948	87	39	41	χ^2 = 6.1 wR = 3.2
	Ni_3Si (*Pm*-3*m*)	*a*=3.507 *Vol*=43.134	*a*=3.5060 *Vol*=43.096	01-086-4982	110	61	59	
Co-Int	CoB (*Pbnm*)	*a*=3.954 *b*=5.264 *c*=3.045 *Vol*=63.373	*a*=3.9480 *b*=5.2430 *c*=3.0370 *Vol*=62.864	04-003-2122	426	49	55	χ^2 = 2.3 wR = 2.2
	CoSi ($P2_13$)	*a*=4.447 *Vol*=87.926	*a*=4.4460 *Vol*=87.884	00-050-1337	233	51	45	
Fe-Int	Fe_2B (*I*4/*mcm*)	*a*=5.016 *c*=4.252 *Vol*=110.879	*a*=5.1059 *c*=4.2510 *Vol*=110.824	04-013-1639	58	52	63	χ^2 = 1.8 wR = 2.6
	Fe_3Si (*Fm*-3*m*)	*a*=5.665 *Vol*=181.770	*a*=5.7522 *Vol*=181.154	04-016-3988	95	48	37	
Mn-Int	Mn (*I*-43*m*)	*a*=8.942 *Vol*=714.982	*a*=8.9120 *Vol*=707.824	00-032-0637	55	11	29	χ^2 = 2.1 wR = 11.1
	Mn_2B (*I*4/*mcm*)	*a*=5.176 *c*=4.213 *Vol*=112.852	*a*=5.1490 *c*=4.2090 *Vol*=111.590	00-025-0535	30	23	28	
	Mn_5Si_3 (*P*63/*mcm*)	*a*=6.920 *c*=4.826 *Vol*=200.160	*a*=6.8980 *c*=4.8020 *Vol*=197.879	01-078-4965	72	36	15	
	Mn_3Si (*Fm*-3*m*)	*a*=5.731 *Vol*=188.230	*a*=5.7242 *Vol*=187.562	04-006-9117	57	22	17	
	MnSi ($P2_13$)	*a*=4.560 *Vol*=94.819	*a*=4.5600 *Vol*=94.819	00-042-1487	91	7	12	

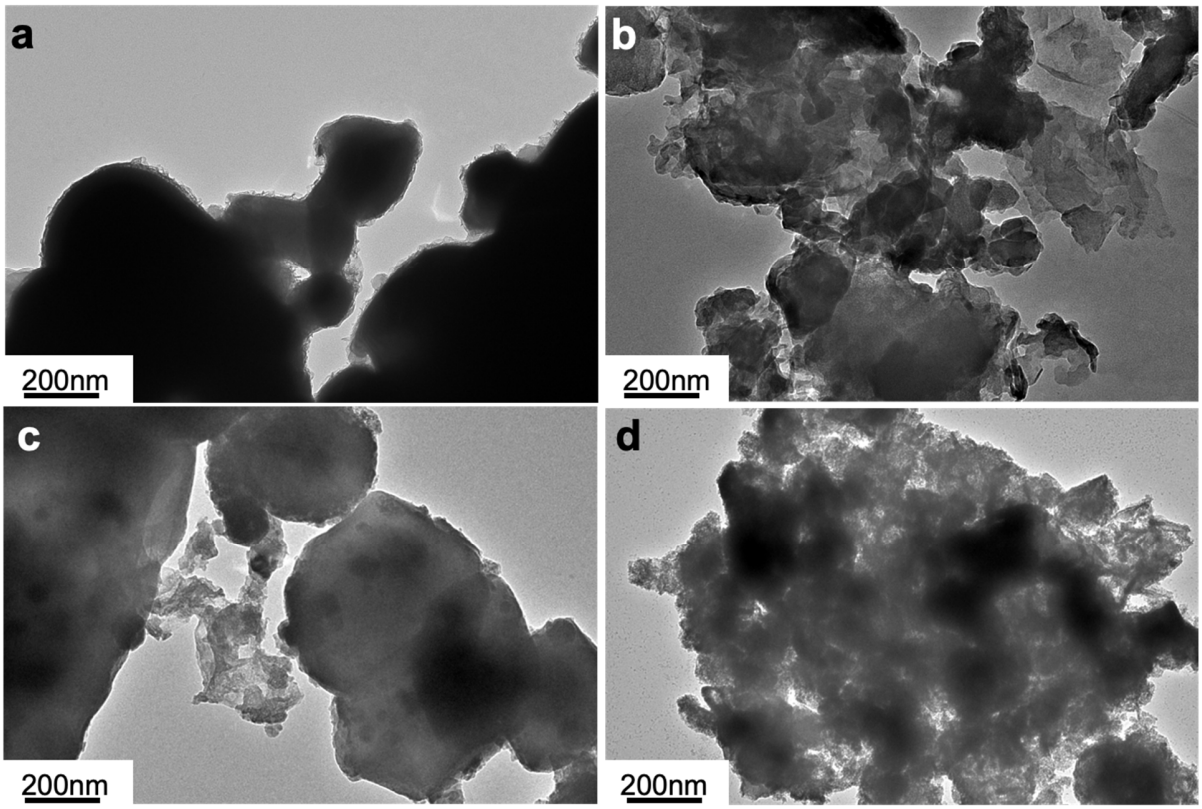

Figure S4. TEM images of reaction intermediates: (a) **Ni-Int**, (b) **Co-Int**, (c) **Fe-Int** and (d) **Mn-Int** samples.

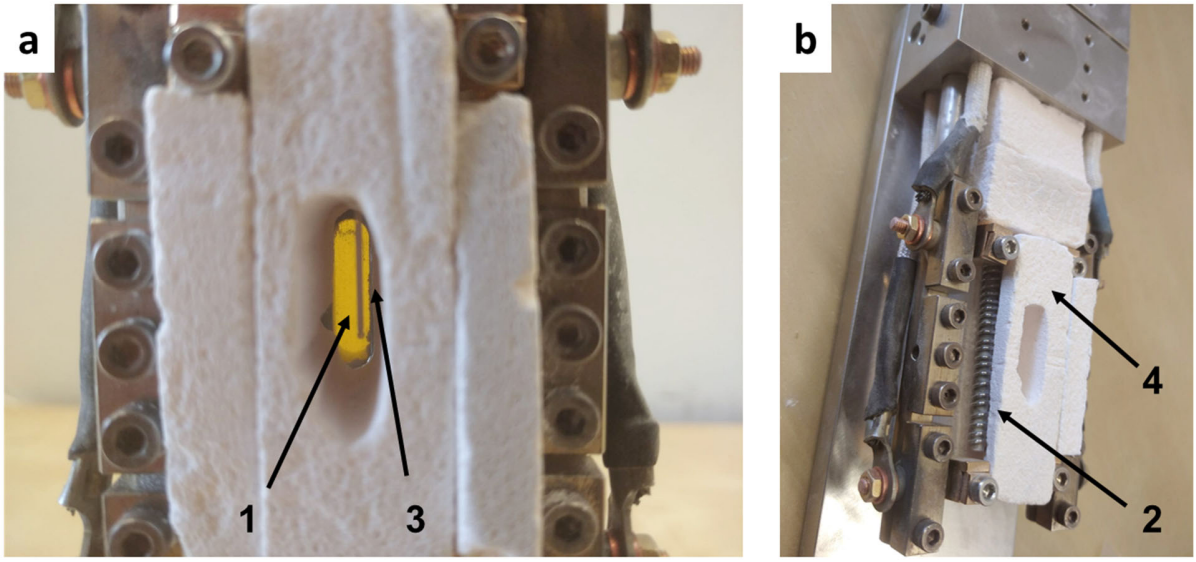

Figure S5. Custom made capillary oven assembly. (a) front view and (b) side view showing (1) capillary, (2) resistive heating elements, (3) thermocouple and (4) insulating material.

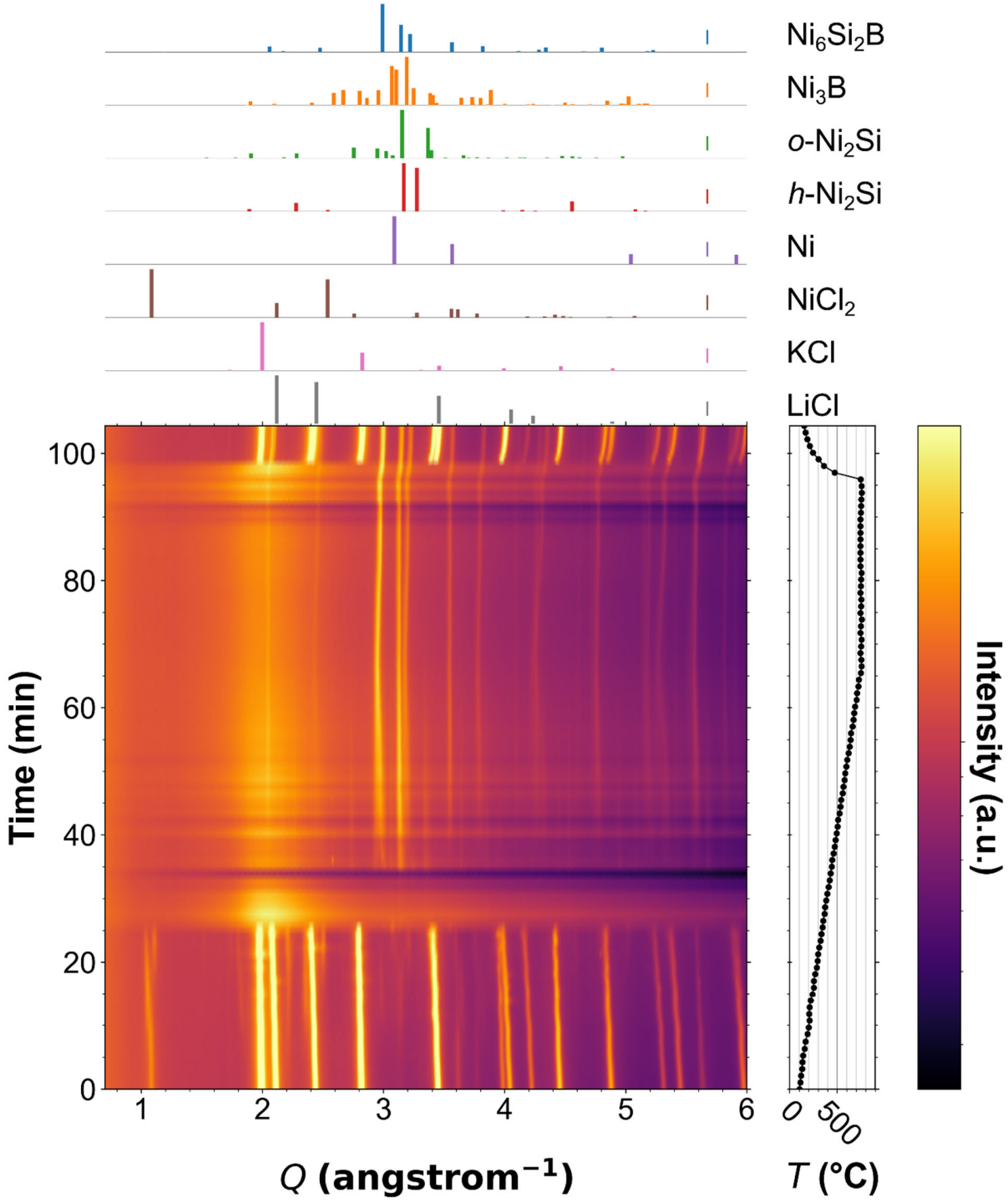

Figure S6. Synchrotron radiation-based *in situ* X-ray diffractograms depicted as heatmaps recorded during the synthesis of Ni_6Si_2B.

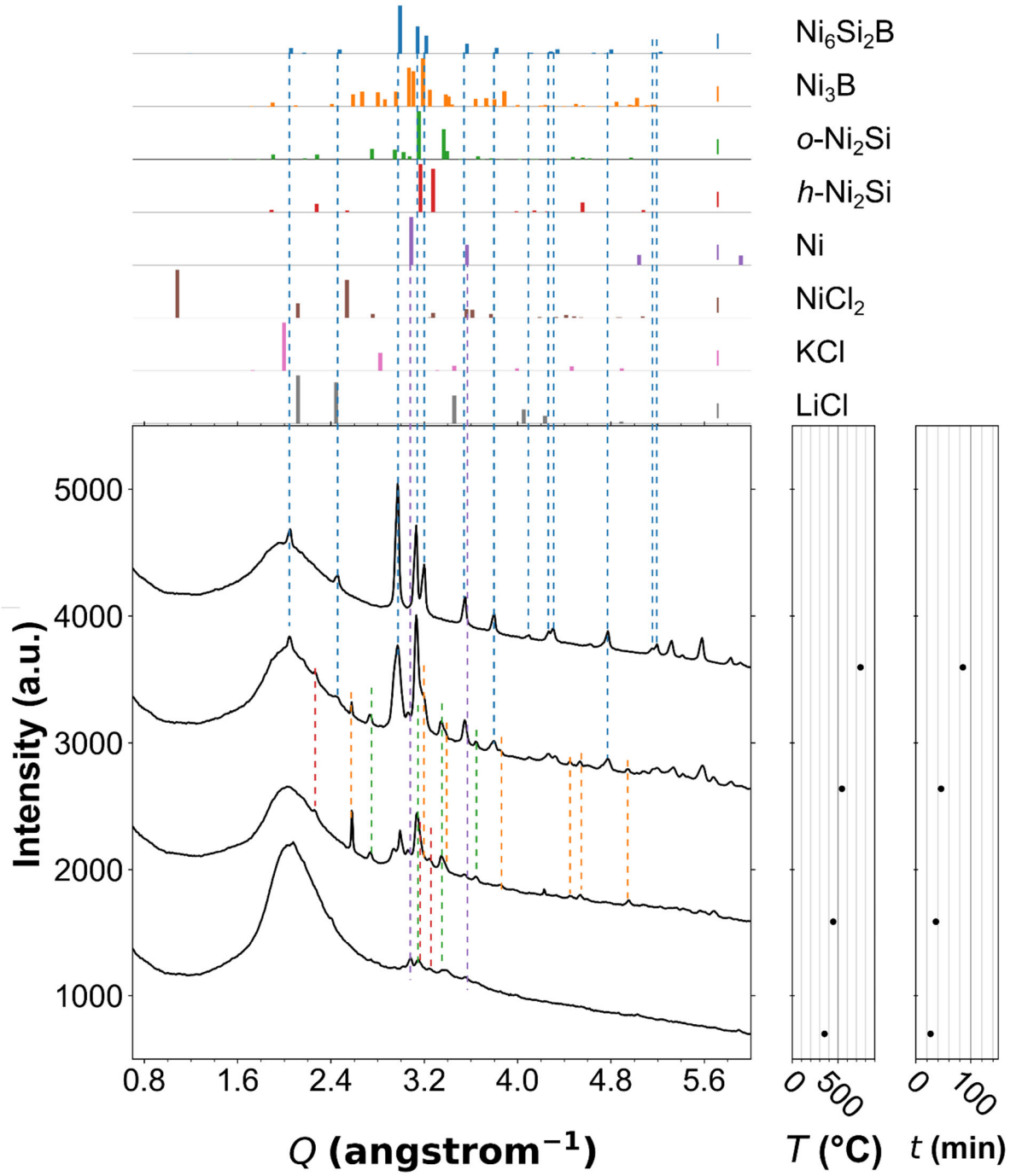

Figure S7. Synchrotron radiation-based *in situ* X-ray diffractograms selected from Figure S6 during the synthesis of Ni_6Si_2B. Note the shift to low q values compared to database references due to thermal dilatation.

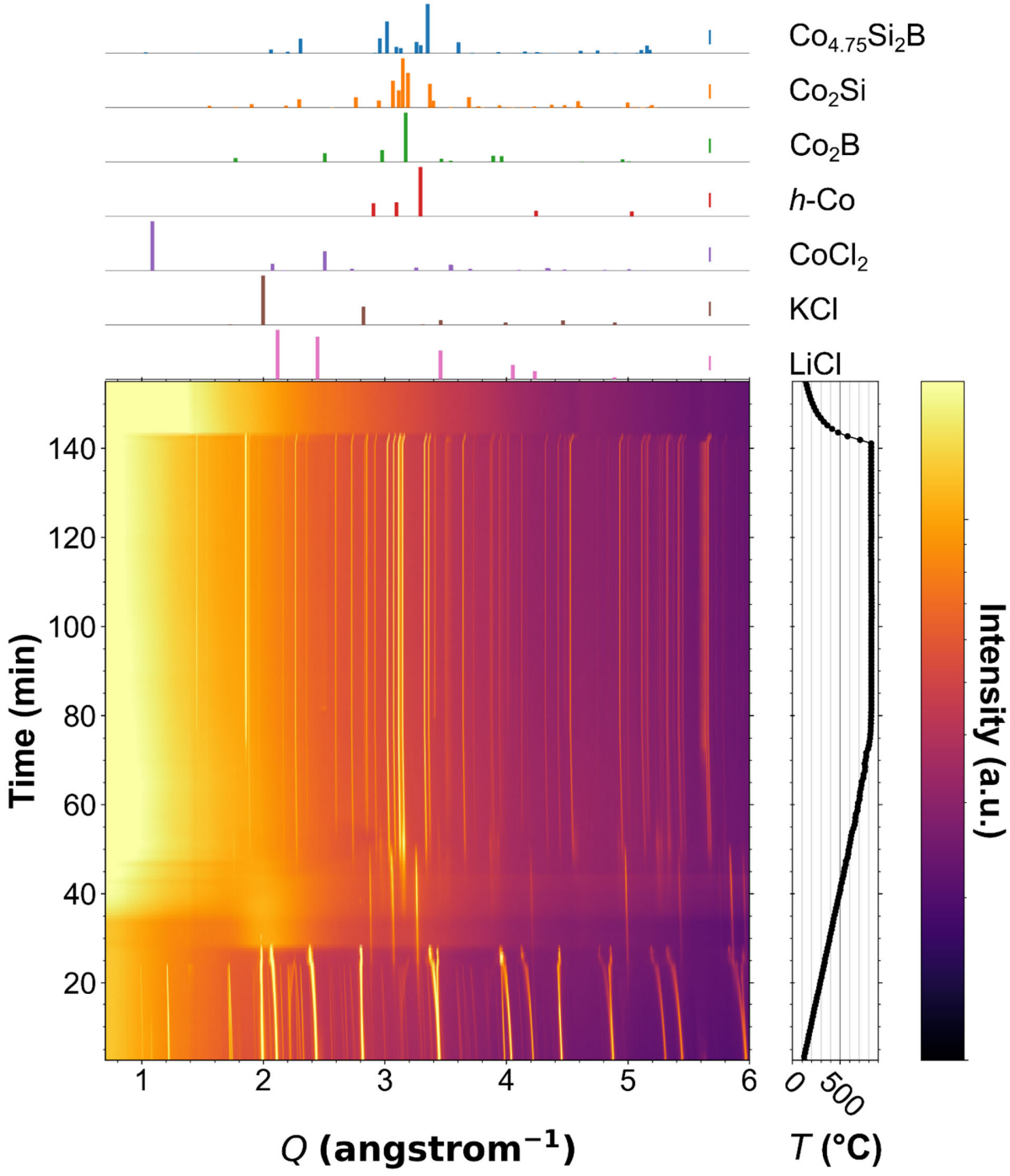

Figure S8. Synchrotron radiation-based *in situ* X-ray diffractograms depicted as heatmaps recorded during the synthesis of $Co_{4.75}Si_2B$.

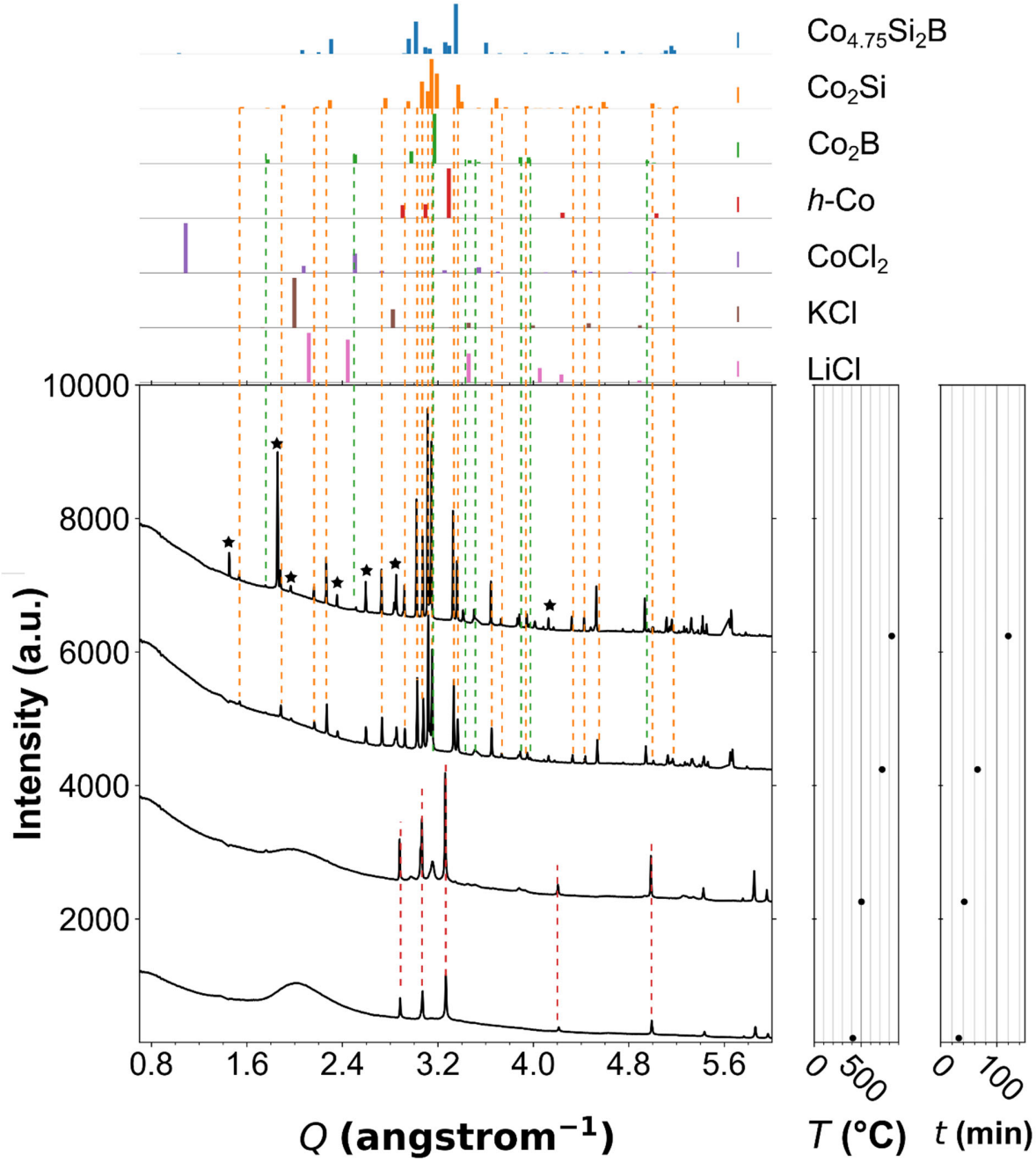

Figure S9. Synchrotron radiation-based *in situ* X-ray diffractograms selected from Figure S8 during the synthesis of $Co_{4.75}Si_2B$. Note the shift to low *q* values compared to database references due to thermal dilatation. Stars indicate peaks that originate from the crystallization of the silica capillary walls at high temperature.

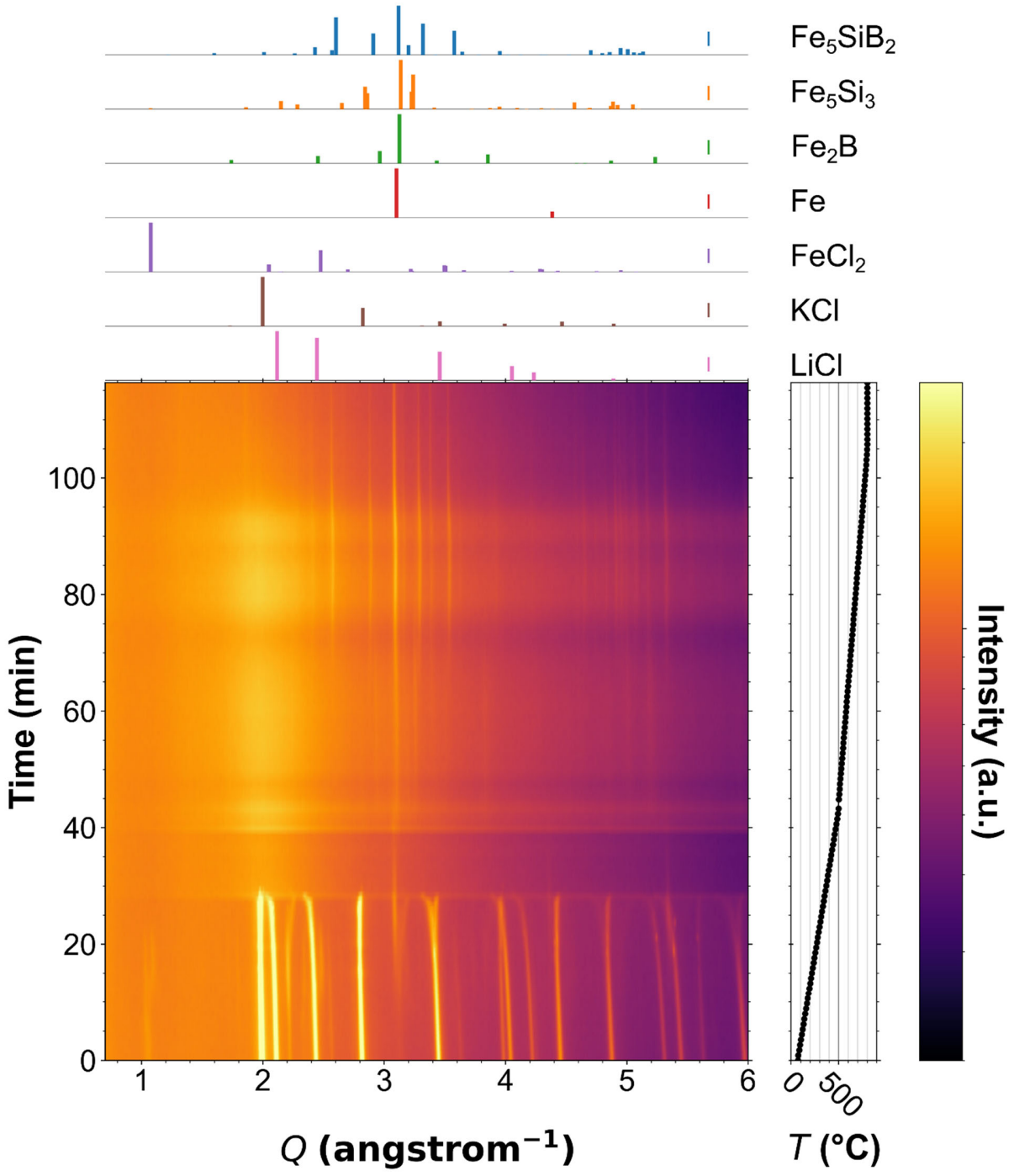

Figure S10. Synchrotron radiation-based *in situ* X-ray diffractograms depicted as heatmaps recorded during the synthesis of Fe_5SiB_2.

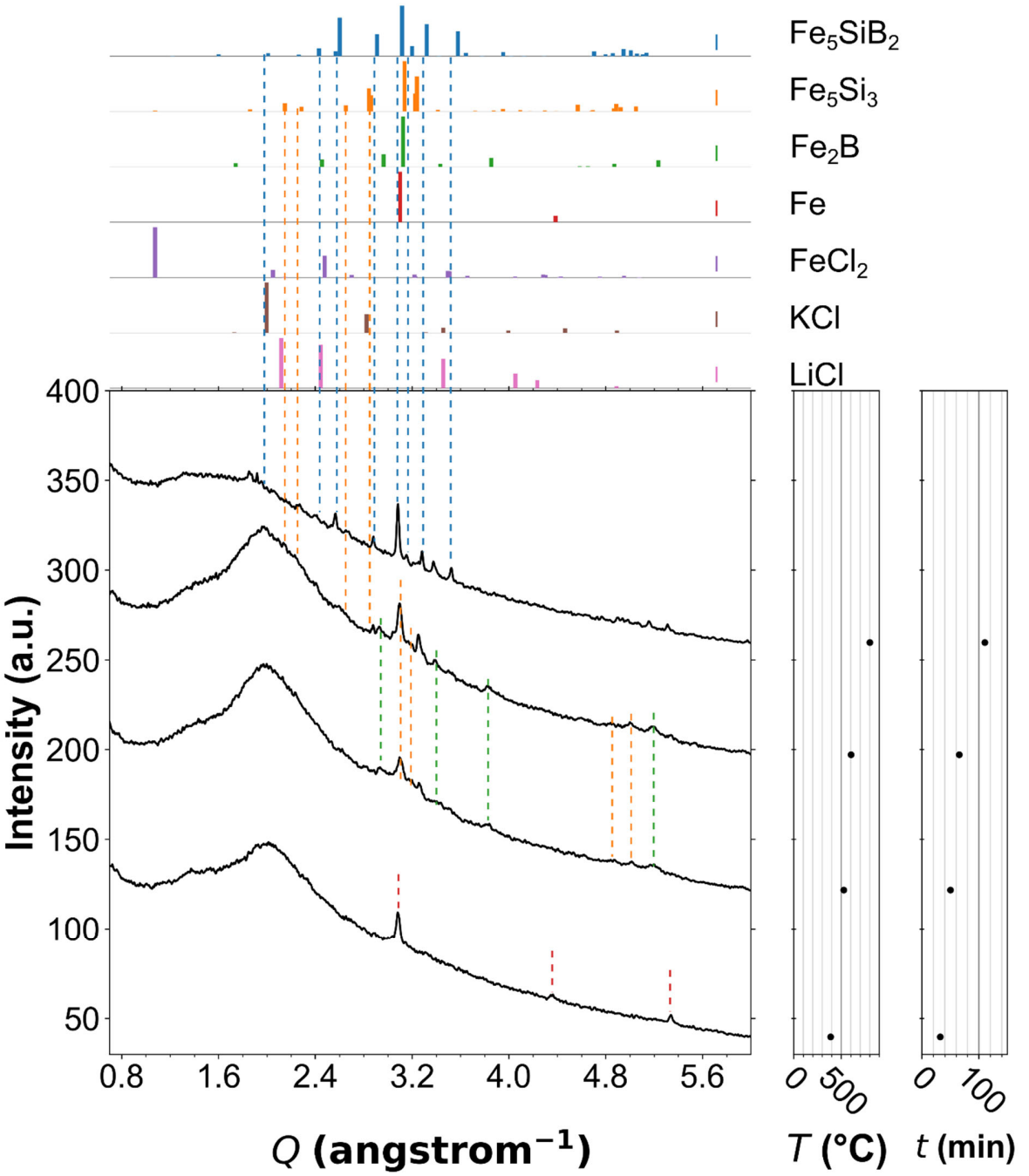

Figure S11. Synchrotron radiation-based *in situ* X-ray diffractograms selected from Figure S10 during the synthesis of Fe_5SiB_2. Note the shift to low q values compared to database references due to thermal dilatation.

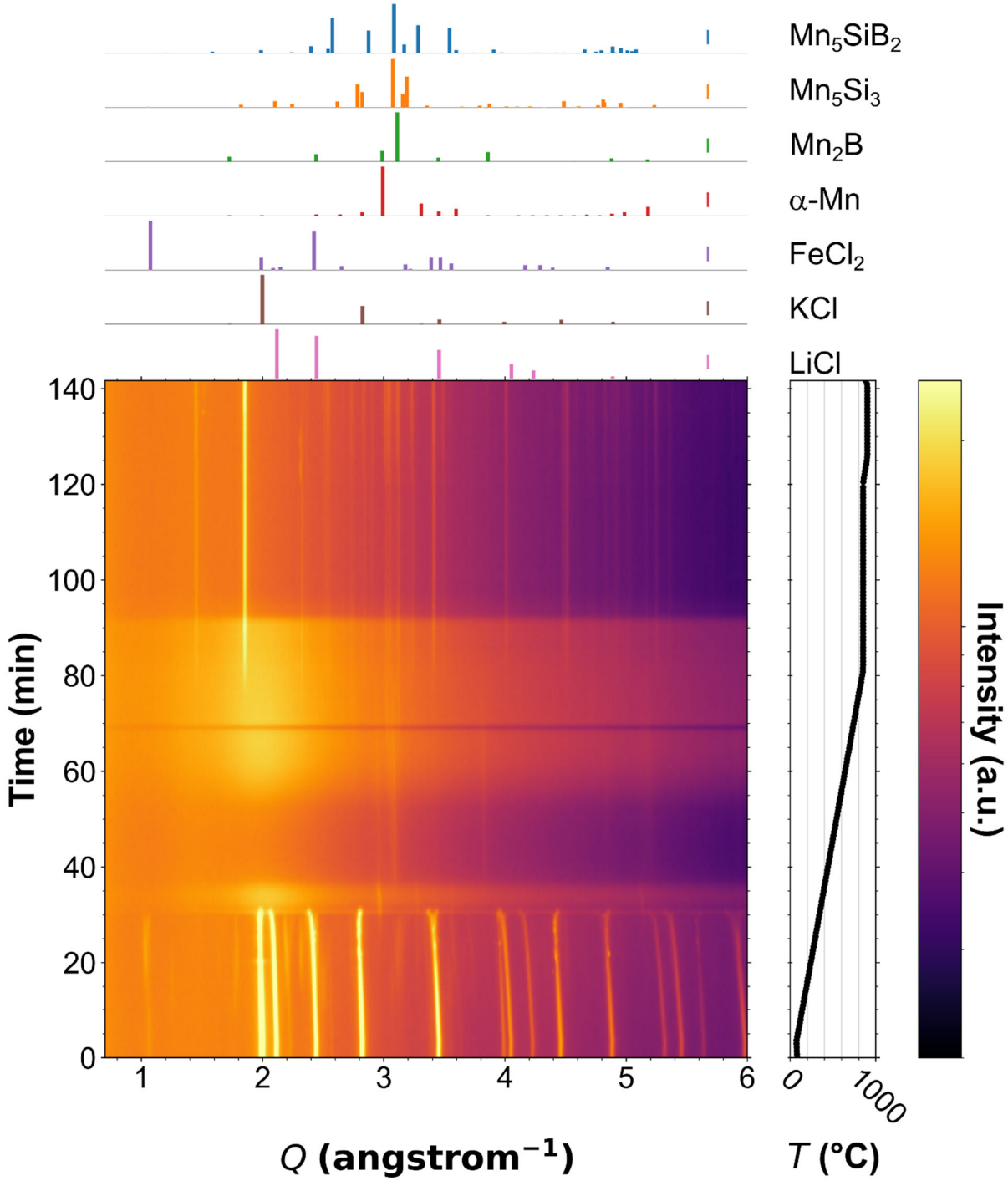

Figure S12. Synchrotron radiation-based *in situ* X-ray diffractograms depicted as heatmaps recorded during the synthesis of Mn_5SiB_2.

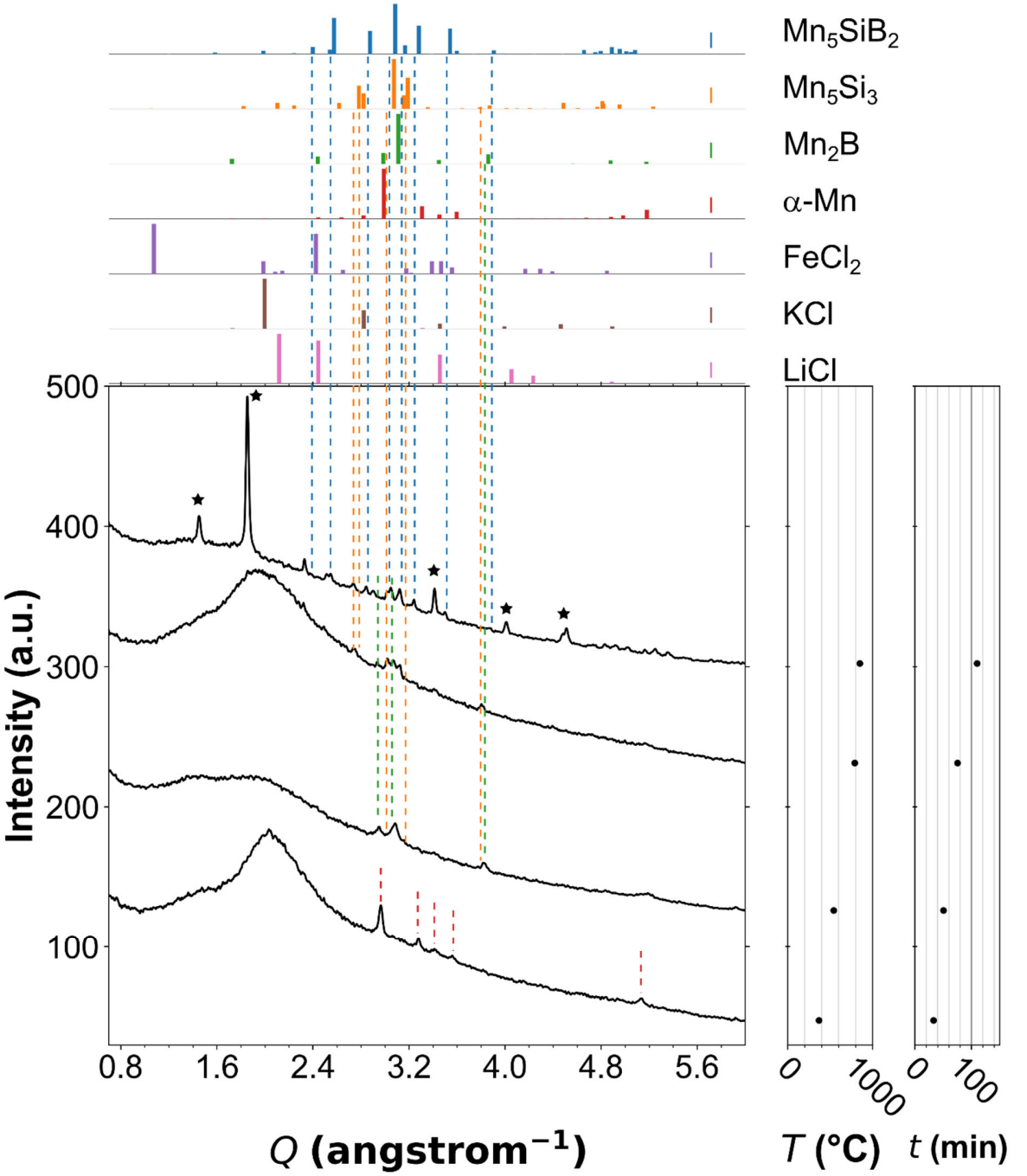

Figure S13. Synchrotron radiation-based *in situ* X-ray diffractograms selected from Figure S12 during the synthesis of Mn_5SiB_2. Note the shift to low *q* values compared to database references due to thermal dilatation. Stars indicate peaks that originate from the crystallization of the silica capillary walls at high temperature.

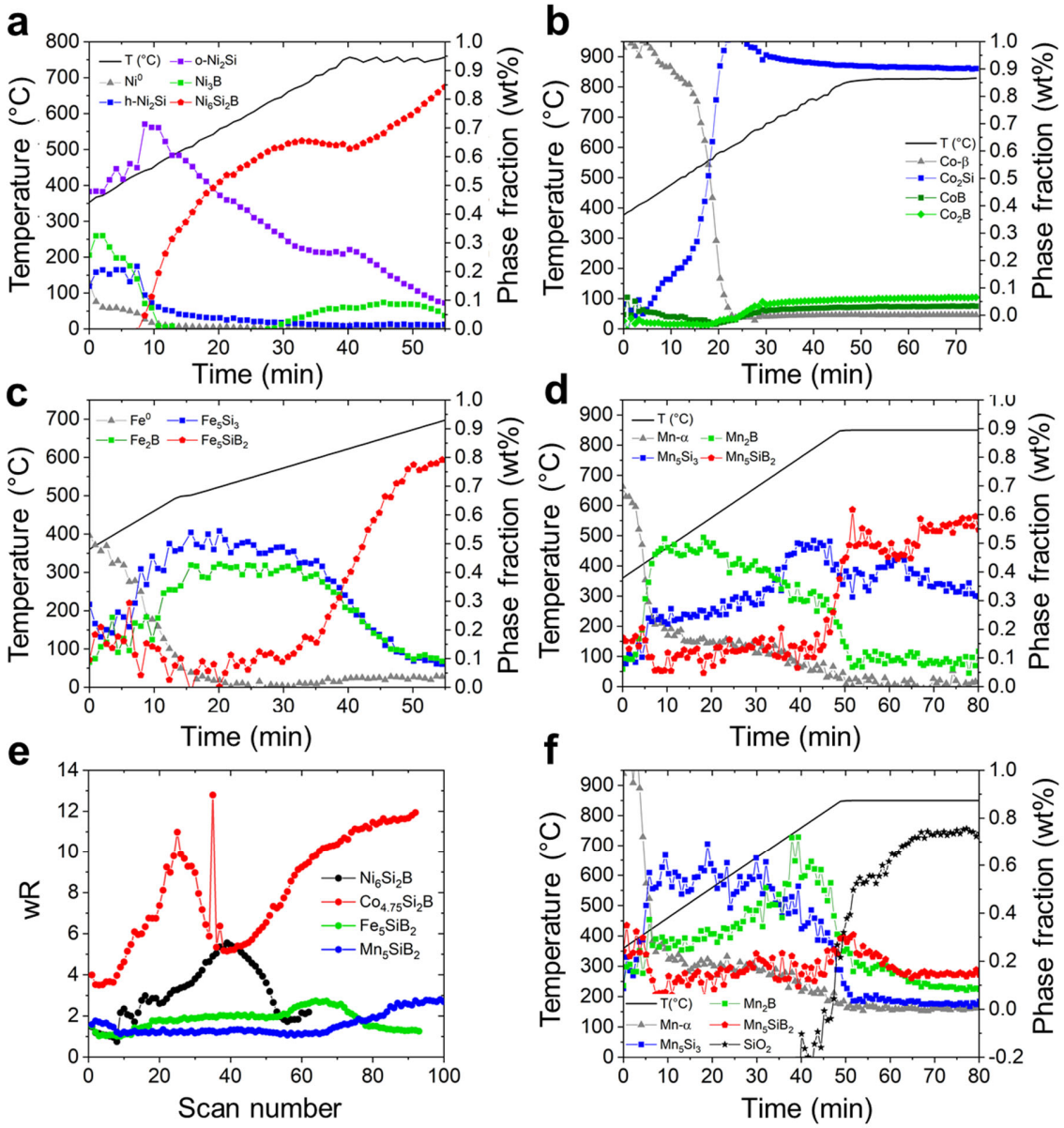

Figure S14. Phase fractions evaluated by sequential Rietveld refinements of *in situ* XRD data as a function of time and temperature for (a) Ni_6Si_2B, (b) $Co_{4.75}Si_2B$, (c) Fe_5SiB_2 and (d) Mn_5SiB_2 syntheses, from which the contribution of crystalline SiO_2, formed by crystallization of the fused silica capillary walls at high temperatures, was removed. (e) Reliability factor *wR* as a function of scan number throughout the sequential refinement. (f) Phase fractions including crystallizing SiO_2 capillary walls, for Mn_5SiB_2 synthesis. For these refinements, the cell parameters were kept constant at values established through classical Rietveld refinements at various temperatures of each dataset, as detailed in **Table S4**.

Table S4. Details of sequential Rietveld refinements of *in situ* XRD data shown in **Figure S14**. The resulting cell parameters were used for phase fraction refinement in **Figure** .

Sample	Phases	Cell parameters (Å)	Crystallite size (nm)
Ni_6Si_2B	Ni	*F m*-3*m* (*a*=3.540, *Vol*=44.377 Å^3)	300
	h-Ni_2Si	*P* $6_3$22 (*a*=3.845, *c*=4.896, *Vol*=62.691 Å^3)	500
	o-Ni_3Si	*P nma* (*a*=5.061, *b*=3.764, *c*=7.066, *Vol*=134.595 Å^3)	500
	Ni_3B	*P nma* (*a*=5.236, *b*=6.654, *c*=4.351, *Vol*=151.592 Å^3)	300
	Ni_6Si_2B	*P* -62*m* (*a*=6.151, *c*=2.923, *Vol*=95.783 Å^3)	500
$Co_{4.75}Si_2B$	Co-β	*P* 63/*mmc* (*a*=2.290, *c*=3.732, *Vol*=16.952 Å^3)	300
	Co_2Si	*P nma* (a=4.514, *b*=3.420, *c*=6.488, *Vol*=100.174 Å^3)	300
	Co_2B	*I* 4/*mcm* (*a*=5.063, *c*=4.247, *Vol*=108.865 Å^3)	300
	CoB	*P nma* (*a*=3.972, *b*=5.221, *c*=3.049, *Vol*=63.221 Å^3)	300
Fe_5SiB_2	α-Fe	*I m*-3*m* (*a*=2.887, *Vol*=24.064 Å^3)	400
	Fe_5Si_3	*P* 63/*mcm* (*a*=6.772, *c*=4.717, *Vol*=187.345 Å^3)	500
	Fe_2B	*I* 4/*mcm* (*a*=5.179, *c*=4.315, *Vol*=115.735 Å^3)	500
	Fe_5SiB_2	*I* 4/*mcm* (*a*=5.638, *c*=10.441, *Vol*=331.867 Å^3)	500
Mn_5SiB_2	Mn-α	*I* -43*m* (*a*=9.008, *Vol*=730.868 Å^3)	200
	Mn_5Si_3	*P* 63/*mcm* (*a*=6.988, *c*=4.904, *Vol*=207.414 Å^3)	500
	Mn_2B	*I* 4/*mcm* (*a*=5.219, *c*=4.222, *Vol*=114.973 Å^3)	500
	Mn_5SiB_2	*I* 4/mcm (*a*=5.693, *c*=10.513, *Vol*=340.732 Å^3)	500
	SiO_2	*P* $3_2$21 (*a*=4.996, *c*=5.462, *Vol*=118.058 Å^3)	3000

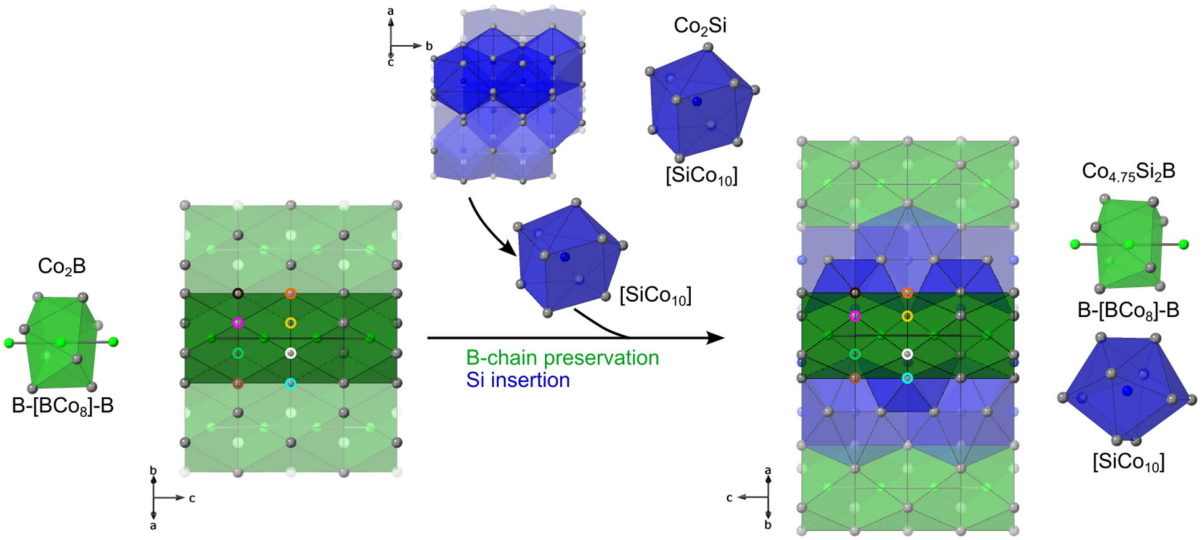

Figure S15. $Co_{4.75}Si_2B$ crystallization mechanism unveiled by *in situ* XRD. Scheme of the reaction mechanism from Co_2B and Co_2Si to $Co_{4.75}Si_2B$. The linear covalent B-chains are maintained from the boride to the borosilicide. Insertion of Si proceeds by maintaining the coordination polyhedra $SiCo_{10}$ of the intermediate silicide phase. Light and dark green boron coordination polyhedra correspond to same crystallographic sites but different colors are used as guides to the eye to highlight structural motifs. Color-coded atoms illustrate how B-centered polyhedra are maintained.

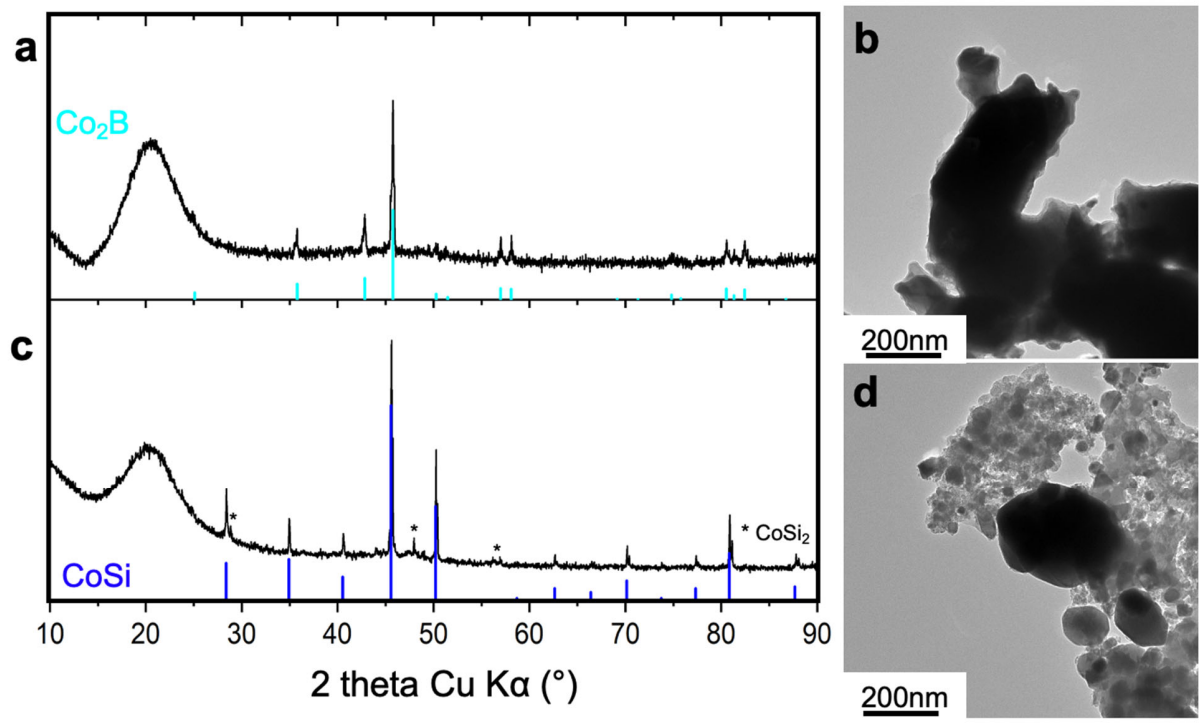

Figure S16. XRD patterns of (a) Co_2B and (c) CoSi with corresponding TEM images (b) and (d). The synthesis and characterisation of other reference materials used for the electrochemical study are described in the literature: Ni_3B,[2] Ni_2Si,[15] FeSi,[3] FeB.[4]

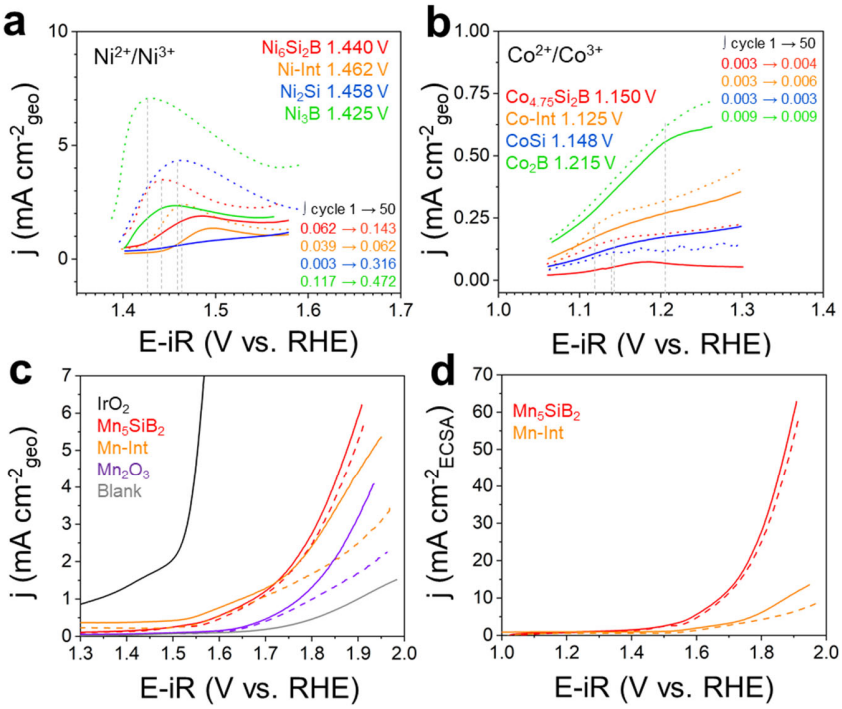

Figure S17. Integration of oxidation waves for (a) Ni and (b) Co samples, with solid lines and dashed lines corresponding to first and 50th cycles, respectively. iR-corrected polarisation curves in Fe-purified and O_2-saturated 0.1 M KOH at a scan rate of 20 mV s^{-1} on a rotating disk electrode (RDE) at 1600 rpm for Mn-based samples: (c) LSV normalised by geometrical surface area and (d) LSV normalised by ECSA.

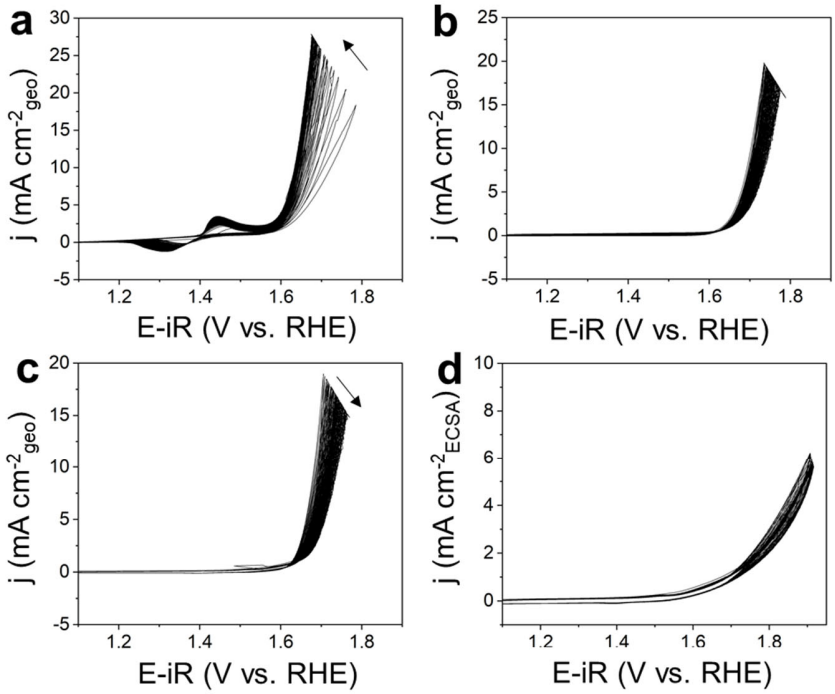

Figure S18. iR-corrected polarisation curves in Fe-free O_2-saturated 0.1 M KOH electrolyte of the first 50 consecutive cycles for (a) Ni_6Si_2B, (b) $Co_{4.75}Si_2B$, (c) Fe_5SiB_2 and (d) Mn_5SiB_2. While Ni_6Si_2B shows activation, the activity Fe_5SiB_2 decreases and $Co_{4.75}Si_2B$ Mn_5SiB_2 remain at constant current densities. Seeming deactivation stems only from bubble formation.

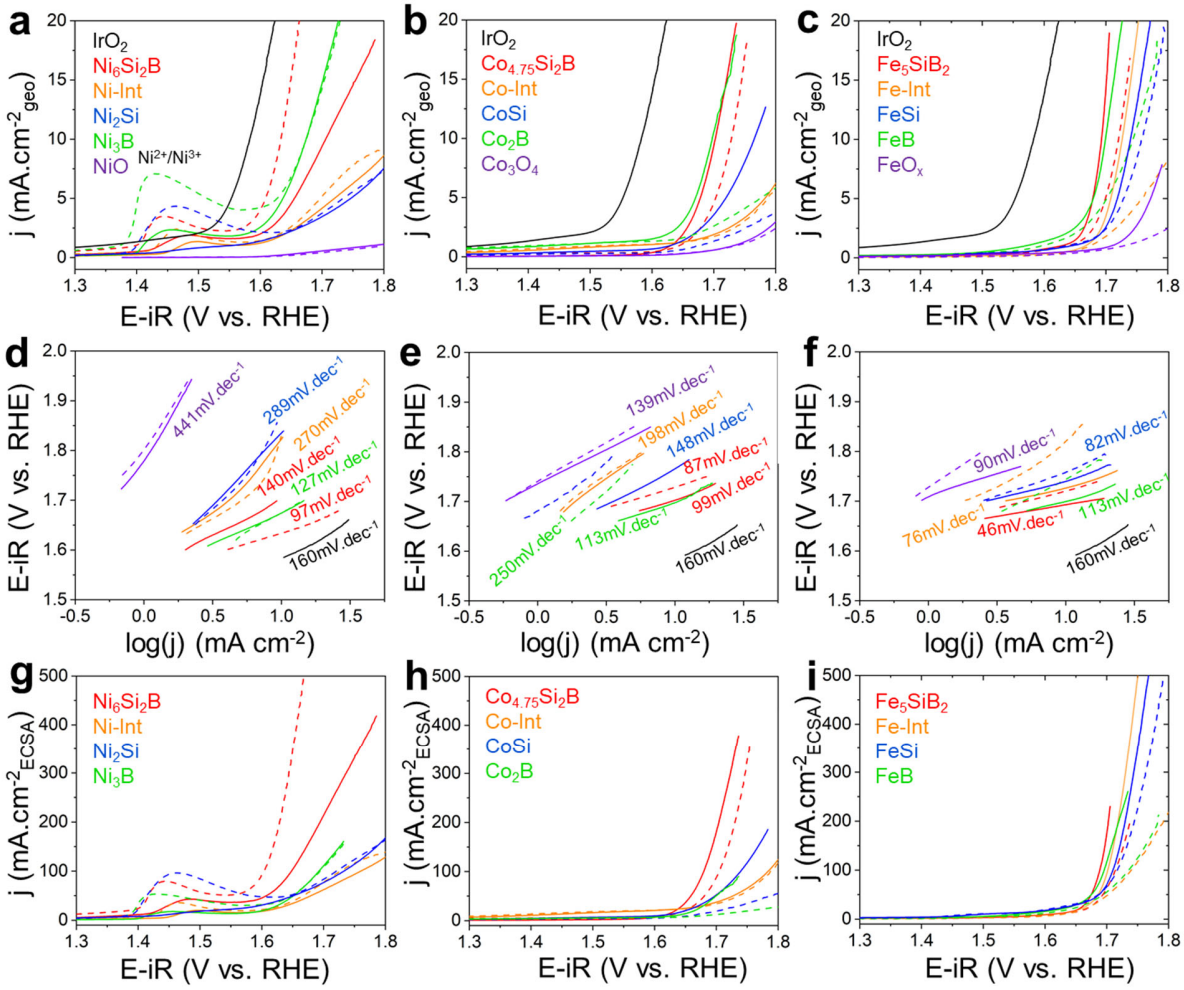

Figure S19. Oxygen evolution reaction electrocatalytic properties. iR-corrected polarisation curves are recorded in Fe-purified and O_2-saturated 0.1 M KOH at a scan rate of 20 mV s^{-1} on a rotating disk electrode (RDE) at 1600 rpm. The current is normalised *vs.* the geometrical surface area for (a) Ni-, (b) Co-, (c) and Fe-based samples. Corresponding Tafel plots for (d) Ni-, (e) Co-, and (f) Fe-based samples. Polarisation curves normalised by ECSA for (g) Ni-, (h) Co-, and (i) Fe-based samples. Solid and dashed lines indicate the 1st and 50th cycles, respectively.

Table S5. Comparison of non-precious OER catalysts in alkaline medium.

OER electrocatalyst	Electrolyte	Overpotential (mV) at 10 mA cm^{-2}_{geo}	Tafel slope (mV dec^{-1})	Mass loading (mg cm^{-2})	Reference
Ni_6Si_2B	0.1M KOH	404	97	0.17	This work
$Co_{4.75}Si_2B$	0.1M KOH	473	88	0.17	This work
Fe_5SiB_2	0.1M KOH	463	46	0.17	This work
Mn_5SiB_2	0.1M KOH	800	292	0.17	This work
NiO	1M NaOH	430	n.a.	0.8	[16]
NiSi Fe-doped	0.1M KOH	337	64	0.17	[3]
Ni_2B	1M KOH	350	58	n.a.	[17]
$Ni_{0.8}Fe_{0.2}B$	0.1M KOH	316	61	n.a.	[18]
Ni_2P	1M KOH	290	47	n.a.	[19]
CoO	1M NaOH	500	n.a.	0.8	[16]
CoB N-doped	0.1M KOH	370	n.a.	0.21	[20]
Co_2B	1M KOH	405	51	0.20	[21]
CoPS	1M KOH	308	58	0.21	[22]
CoSi	0.1M KOH	370	n.a.	0.17	[23]
Fe_2O_3	1M NaOH	1240	n.a.	0.8	[16]
FeSi/Nickel foam	1M KOH	219	39	n.a.	[24]
FeB	1M KOH	460	58	0.56	[25]
CoFeB	1M KOH	280	39	0.56	[25]
Mn_2O_3	1M NaOH	500	n.a.	0.8	[16]
MnO_2 nanorods	1M KOH	450	73	n.a.	[26]
Mn_3O_4	0.1M KOH	570	72	n.a.	[27]

Supplementary text 1: electrocatalytic properties

Electrochemically active surface area (ECSA) evaluation. As the geometric surface area may not reflect similar catalyst surfaces and active sites from one sample to the other, we have normalized the current densities by the electrochemical surface area (ECSA). The quantification of the coulombic charge by integration of the CV oxidation peak to extract the electrochemical surface area (ECSA), was shown not reliable, because redox reactions may penetrate deeper than one monolayer of catalyst [28] and the actual number of electrons transferred per metal site may deviate from the monolayer assumption, in addition to uncertainties from baseline determination.[8] We have then evaluated the ECSA by measuring the double layer capacitance (C_{DL}) that is a quantitative indicator of the surface area accessible to electrolyte ions. It can be determined by measuring CVs at various scan rates, where C_{DL} is evaluated from the slope of the current density at the middle of the potential window (**Figure S20**) plotted as a function of scan rate, shown in **Figure S21**. The ECSA (**Table S6**) is obtained by dividing C_{DL} by the specific capacitance approximated to 40 μF cm^{-2} for transition metal-based catalysts in 0.1-1M KOH solutions.[8,9,29]

Electrochemical impedance spectroscopy (EIS). Nyquist plots of the pristine electrodes before activation (before CV) in **Figure 6e** were fitted with an equivalent circuit $R_s(Q_{dl}R_{ct}(Q_{ads}R_{ads}))$ comprising three resistive components (**Table S7**).[30,31] R_s describes the resistance of the electrolyte and ranges narrowly between 11.2 and 11.9 Ω.cm^2 for all materials, attesting equal electrolyte concentration and distance from the CE. The charge transfer resistance (R_{ct}) is evaluated from the smallest circle at high frequency (**Figure 6e**). R_{ads} is ascribed to the larger circle at middle frequencies (**e**).

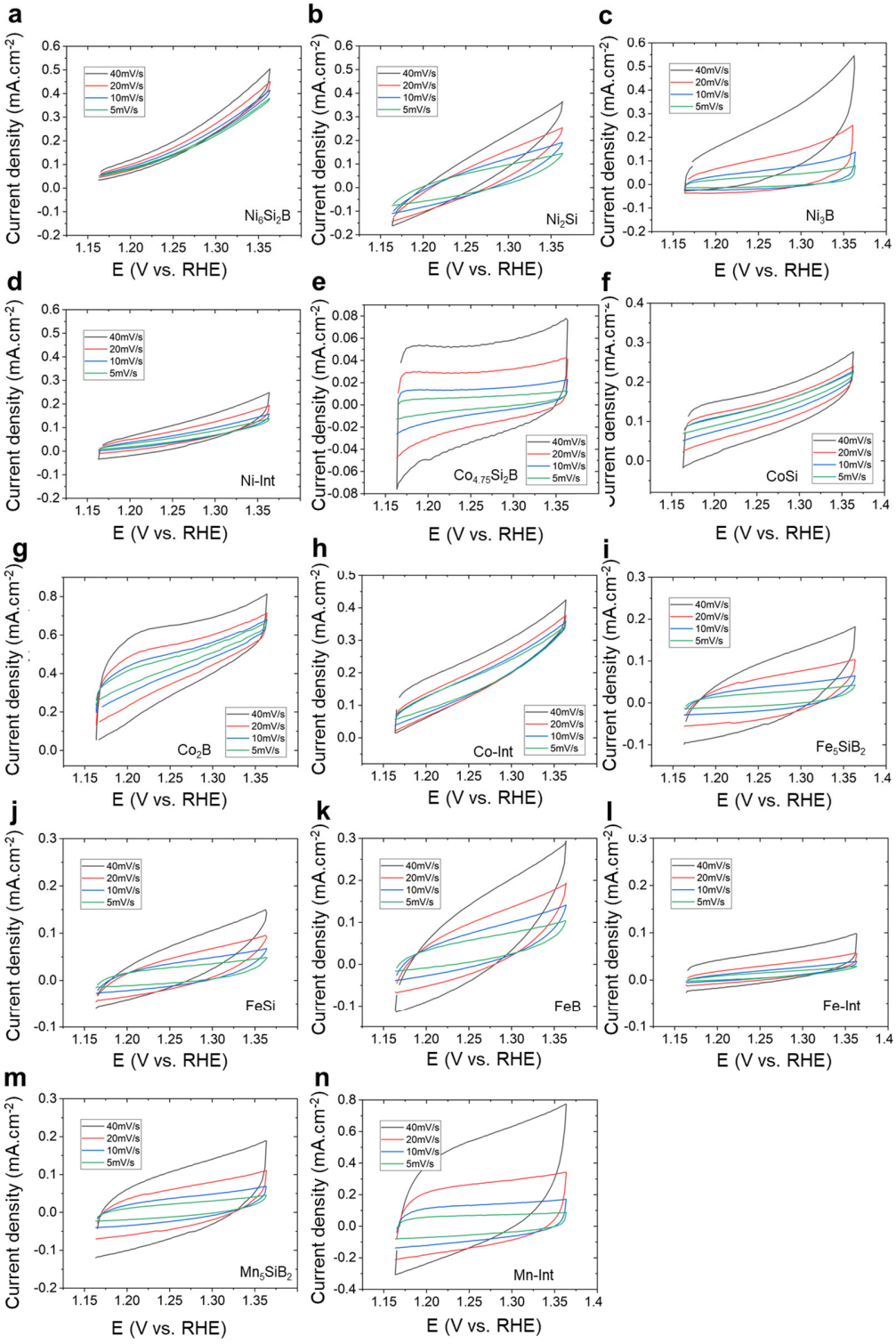

Figure S20. ECSA measurements: 5th cyclic voltammograms at scan rates from 40 to 5 mV s^{-1} in Ar-saturated and Fe-purified 0.1 M KOH of (a) Ni_6Si_2B, (b) Ni_2Si, (c) Ni_3B, (d) Ni-Int, (e) $Co_{4.75}Si_2B$, (f) CoSi, (g) Co_2B, (h) Co- Int, (i) Fe_5SiB_2, (j) FeSi, (k) FeB, (l) Fe-Int, (m) Mn_5SiB_2, (n) Mn-Int.

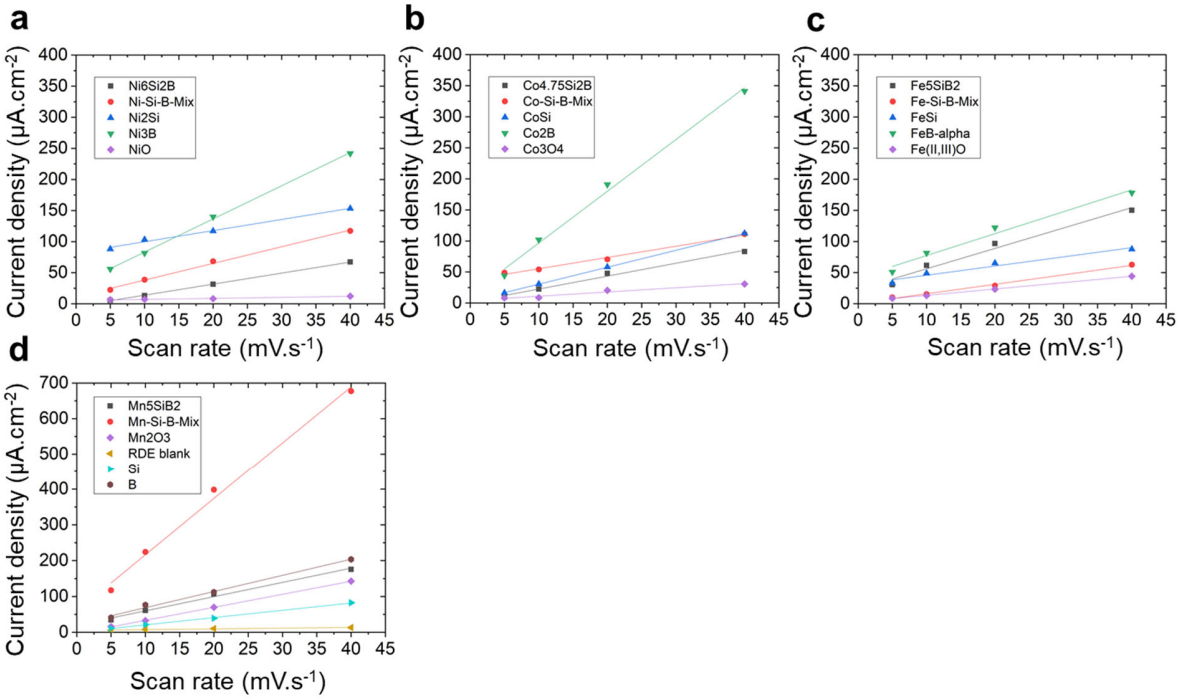

Figure S21. ECSA measurement: current densities from **Table S6** plotted as a function of scan rate (a) Ni-samples, (b) Co-based samples, (c) Fe-based samples, (d) Mn-based samples including elemental Si and elemental B references.

Table S6. Overview of electrochemical surface areas (ECSAs) measured before catalytic activation. The ECSA value was obtained by dividing the C_{CDL} value by Cs = 40 µF cm^{-2}.

Sample	I (mA) 40mVs^{-1}	I (mA) 20mVs^{-1}	I (mA) 10mVs^{-1}	I (mA) 5mVs^{-1}	Linear interpolation	R^2	C_{DL} (µF)	ECSA (cm^2)
Ni_6Si_2B	67.23	31.58	13.24	5.6	y=1.77x-3.85	0.9997	1.77	0.044
Ni-Int	117.14	68.25	38.71	22.41	y=2.68x+11.3	0.9964	2.68	0.067
Ni_2Si	153.3	117.14	103.39	88.11	y=1.79x+81.89	0.9911	1.79	0.045
Ni_3B	241.91	140.06	81.49	56.02	y=5.33x+29.89	0.9992	5.33	0.133
NiO	12.22	8.15	7.08	6.62	y=0.16x+5.47	0.9741	0.16	0.004
$Co_{4.75}Si_2B$	83.02	47.87	22.41	9.68	y=2.08x+1.75	0.9903	2.08	0.052
Co-Int	111.03	70.38	53.99	48.89	y=1.81x+37.09	0.9917	1.81	0.045
CoSi	112.04	58.06	30.56	16.3	y=2.73x+3.06	0.9999	2.73	0.068
Co_2B	341.23	190.99	101.86	44.31	y=8.33x+13.35	0.9942	8.33	0.208
Co_3O_4	30.56	20.37	8.66	8.15	y=0.68x+4.23	0.9618	0.68	0.017
Fe_5SiB_2	150.24	96.77	61.62	30.56	y=3.28x+23.28	0.9754	3.28	0.082
Fe-Int	62.64	29.03	15.28	10.19	y=1.52x+0.75	0.9943	1.52	0.038
FeSi	87.6	65.19	48.89	33.1	y=1.47x+31.05	0.9598	1.47	0.037
FeB	178.25	122.23	81.49	50.93	y=3.52x+42.29	0.9768	3.52	0.088
$Fe(II,III)O_x$	44.31	23.43	13.24	8.66	y=1.02x+3.21	0.9997	1.02	0.026
Mn_5SiB_2	175.71	106.95	61.12	34.63	y=3.97x+20.08	0.9916	3.97	0.099
Mn-Int	677.36	398.17	224.09	117.14	y=15.8x+58.9	0.9933	15.75	0.394
Mn_2O_3	142.6	69.77	32.59	15.79	y=3.64x+3.0	0.9999	3.64	0.091
RDE blank	13.24	10.29	7.64	6.11	y=0.2x+5.58	0.9715	0.2	0.005
Si	82.51	39.22	21.39	11.2	y=2.03x+0.47	0.9984	2.03	0.051
B	203.72	112.04	76.39	40.74	y=4.51x+23.69	0.9938	4.51	0.113

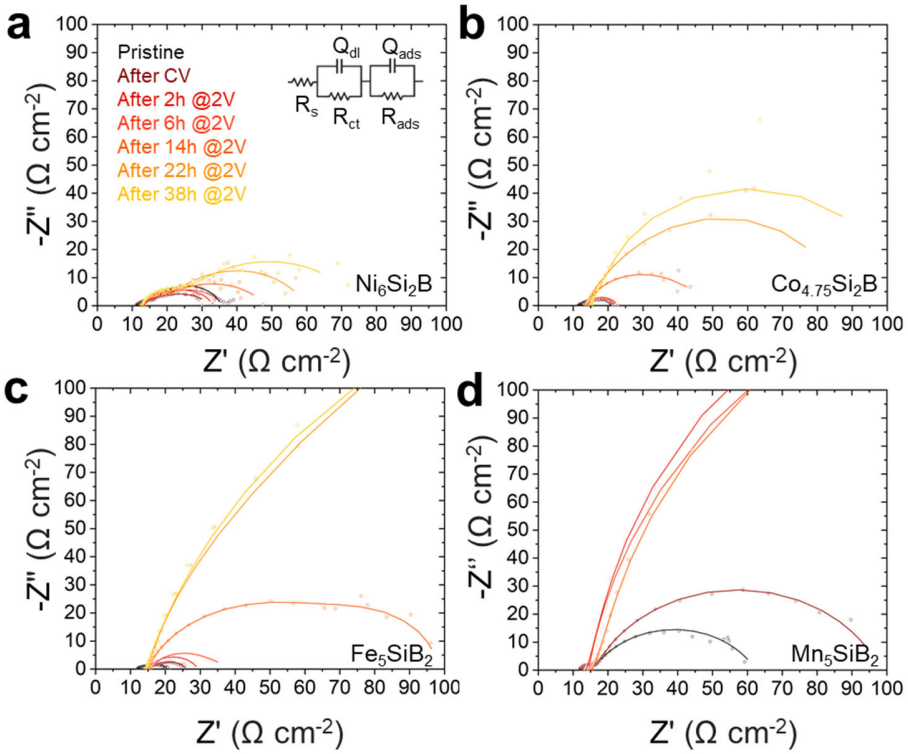

Figure S22. Electrochemical impedance spectra recorded at 2 V vs. RHE before electrocatalytic reaction (pristine), after CV cycles and during long term CA measurements, plotted as Nyquist plots for (a) Ni_6Si_2B (inset shows the equivalent circuit used for the fit), (b) $Co_{4.75}Si_2B$, (c) Fe_5SiB_2, (d) Mn_5SiB_2. Ni_6Si_2B and $Co_{4.75}Si_2B$ were activated by 50 cycles between 1 and 2 V vs. RHE before CA measurements. Fe_5SiB_2 and Mn_5SiB_2 were activated only by 5 CV cycles to prevent premature degradation.

Table S7. R_s, R_{ct} and R_{ads} values measured by EIS before and after electrochemical activation detailed in **Figure S22**, then at different CA durations at 2 V vs. RHE.

Sample		Before	Post CV	after 2h	after 6h	after 14h	after 22h	after 38h
Ni_6Si_2B	R_s ($\Omega.cm^2$)	11.2	12.9	13.6	13.2	12.4	12.7	12.7
	R_{ct} ($\Omega.cm^2$)	4.9	12.0	13.4	19.4	30.1	38.7	57.2
	R_{ads} ($\Omega.cm^2$)	19.6	6.3	5.8	3.6	5.4	8.5	10.6
$Co_{4.75}Si_2B$	R_s ($\Omega.cm^2$)	11.4	13.6	13.5	14.1	13.6	13.6	-
	R_{ct} ($\Omega.cm^2$)	5.6	8.0	8.1	8.5	27.5	56.5	-
	R_{ads} ($\Omega.cm^2$)	4.4	0.4	0.4	0.5	7.3	18.6	-
Fe_5SiB_2	R_s ($\Omega.cm^2$)	11.8	14.3	14.8	14.8	14.8	15.1	-
	R_{ct} ($\Omega.cm^2$)	3.7	12.7	14.2	19.6	61.9	303.3	-
	R_{ads} ($\Omega.cm^2$)	4.6	2.2	2.8	3.6	35.3	65.7	-
Mn_5SiB_2	R_s ($\Omega.cm^2$)	11.9	12.0	13.5	-	-	-	-
	R_{ct} ($\Omega.cm^2$)	4.4	4.4	83.9	-	-	-	-
	R_{ads} ($\Omega.cm^2$)	40.4	79.4	306.0	-	-	-	-

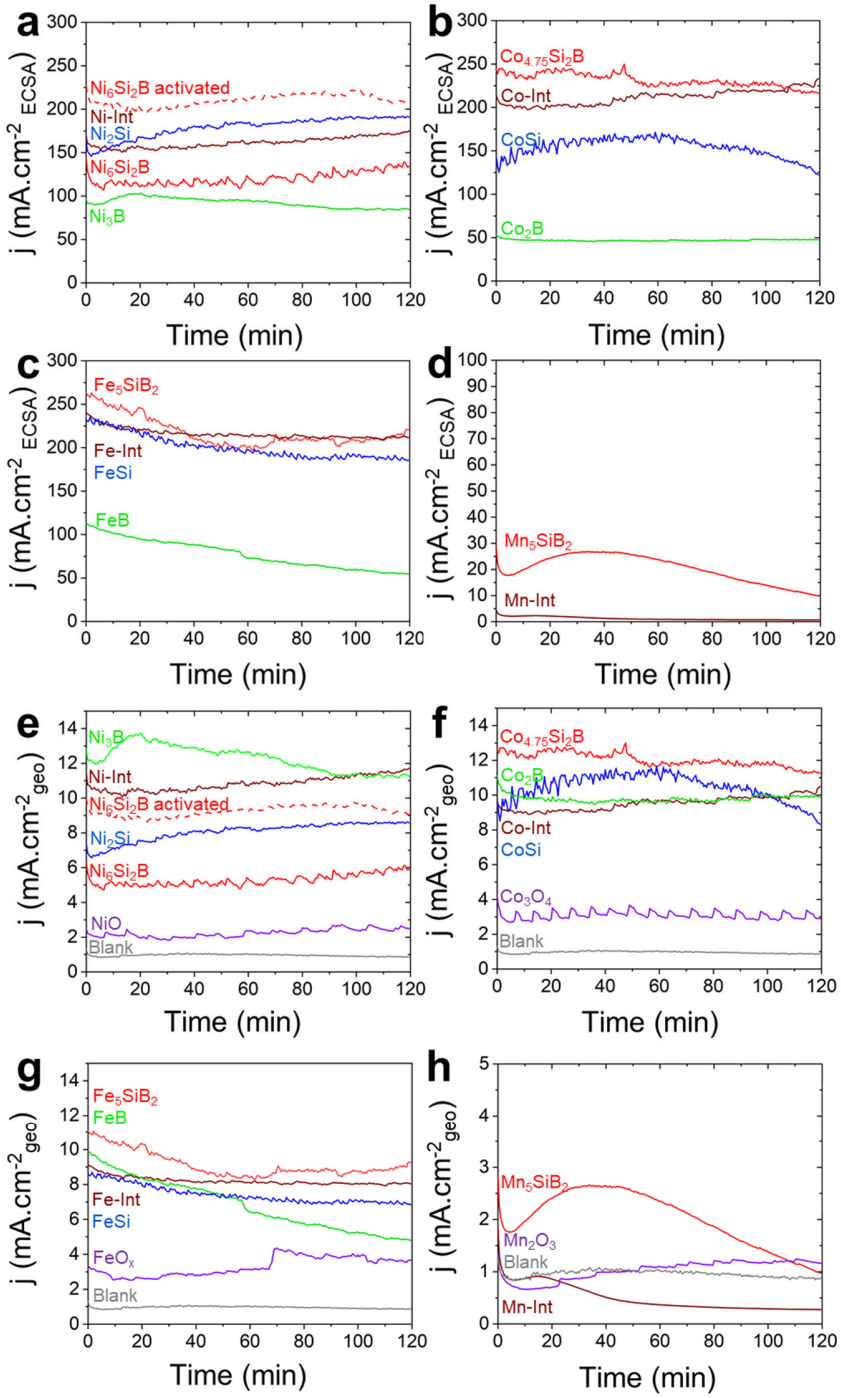

Figure S23. Chronoamperometric measurements at 2 V vs. RHE normalised versus the electrochemical surface area (ECSA) for (a) Ni-, (b) Co-, (c) Fe-, and (d) Mn-based samples and normalised versus the geometric surface area for (e) Ni-, (f) Co-, (g) Fe- and (h) Mn-based samples.

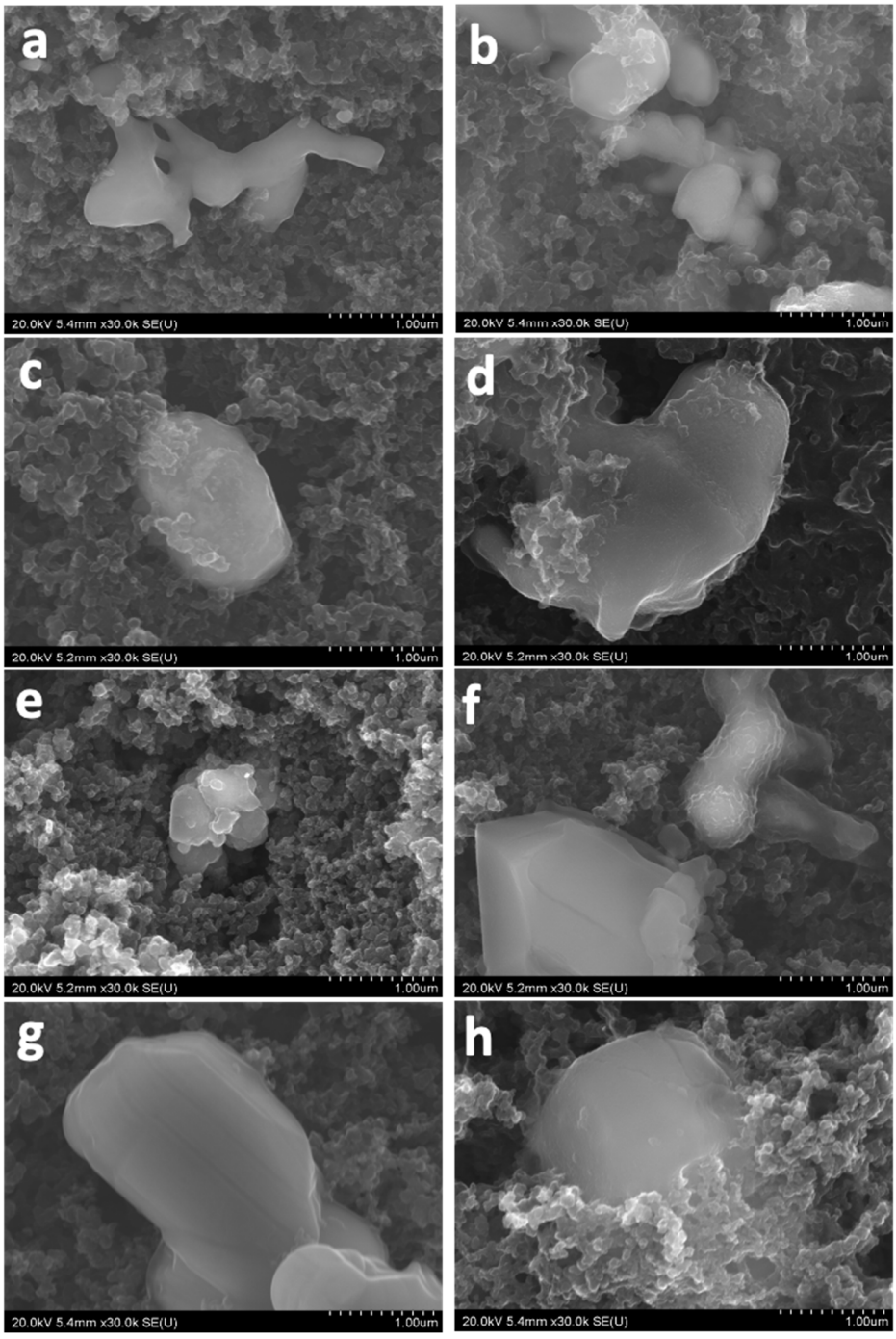

Figure S24. Secondary electron mode SE-SEM images of (a) pristine electrodes (PE) and (b) post-catalysis (PC) Ni_6Si_2B electrodes, (c) PE and (d) PC $Co_{4.75}Si_2B$ electrodes, (e) PE and (f) PC Fe_5SiB_2 electrodes, PE (g) and (h) PC Mn_5SiB_2 electrodes. The electrodes exhibit large and faceted particles embedded in the ~50 nm carbon black particles before and after catalysis.

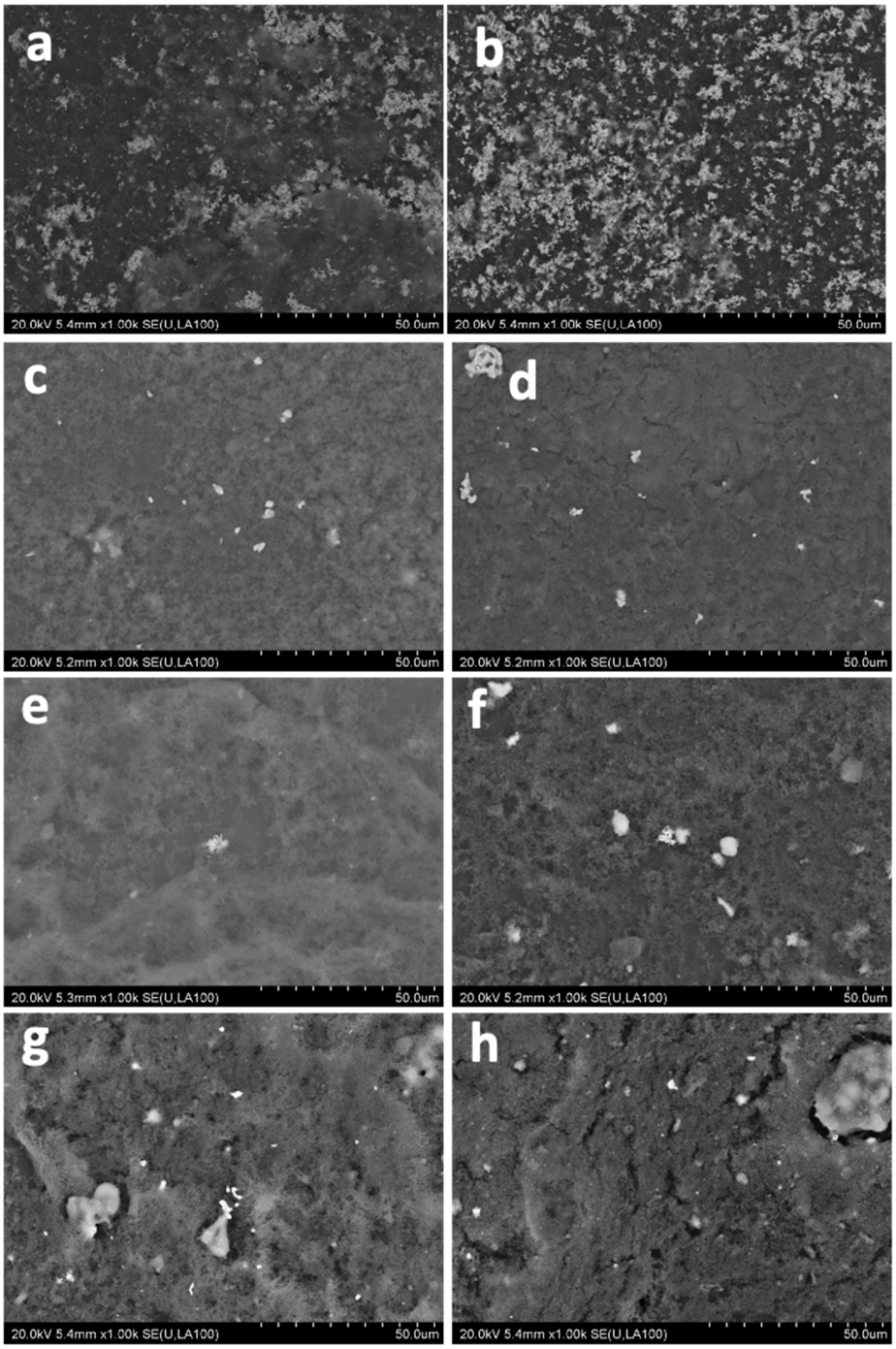

Figure S25. Low magnification backscattered electron mode BSE-SEM images of (a) PE and (b) PC Ni_6Si_2B electrodes, (c) PE and (d) PC $Co_{4.75}Si_2B$ electrodes, (e) PE and (f) PC Fe_5SiB_2 electrodes, PE (g) and (h) PC Mn_5SiB_2 electrodes. The electrodes exhibit large and faceted particles embedded in the ~50 nm carbon black particles before and after catalysis.

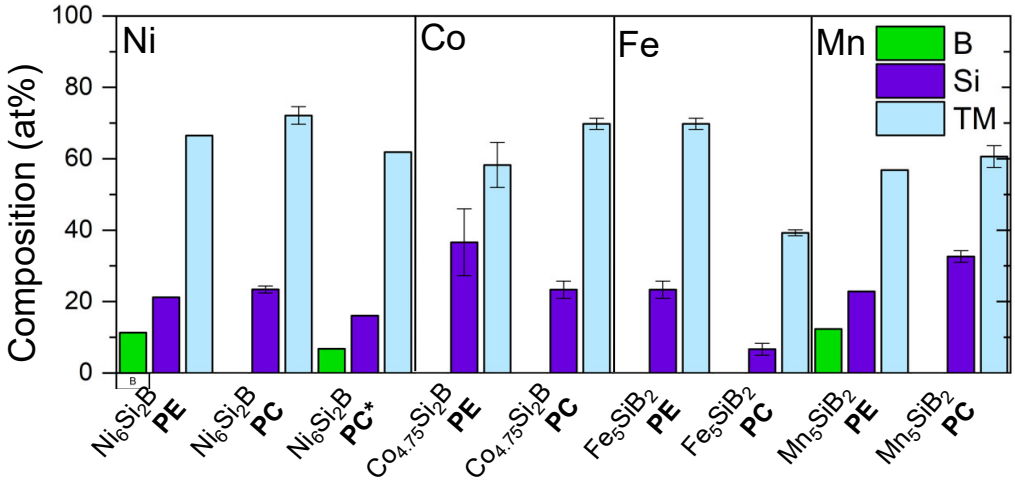

Figure S26. SEM-EDS relative metal, silicon and boron contents for Ni_6Si_2B, $Co_{4.75}Si_2B$, Fe_5SiB_2 and Mn_5SiB_2 before (PE) and after (PC) chronoamperometry for 2 h at 2V vs. RHE (**Figure S23**). The asterisk (*) represents Ni_6Si_2B that was activated through 50 CV cycles between 1 and 2 V vs. RHE before CA. The B content however is strongly decreased after catalysis, as boron is not detected. The low energy of the B-K transition results in strong auto-absorption that makes its detection by EDS challenging, especially if the surface is depleted in boron.

Supplementary text 2: XPS results and discussion

Nickel borosilicide. The Ni $2p_{3/2}$ spectrum of Ni_6Si_2B shows three contributions at 852.6, 856.0 and 861.2 eV (**Figure 7a,** full 2p spectrum in **Figure S27a**). The low energy peak indicates low valence Ni that is typically found in elemental Ni (852.6-852.7 eV) [32,17] and nickel borides (852.2-852.5 eV) [33,34,18], as we also measure in Ni_3B (852.6 eV, **Figure 7a** and **Figure S27a**). This peak appears at lower binding energy than for silicides [3,15,33] as observed for Ni_2Si (853.1 eV). The Si 2p doublet peaks at 98.9 eV/99.6 eV (**Figure S27e**) is consistent with values recorded on metal silicides[15,33] and measured herein for Ni_2Si. It is negatively shifted compared to elemental Si (99.5 eV) [35] which indicates electron enrichment of Si from Ni atoms, its only closest neighbours in the crystal structure of Ni_6Si_2B. Likewise, the low valence B 1s binding energy (187.9 eV, **Figure 7f**) is consistent with values measured with metal-rich borides and negatively shifted compared to elemental boron (189.2 eV) [36], again indicating electron enrichment of boron from nickel. Overall electron transfer from Ni to Si and B agrees with the electronegativity scale, which yields a global charge state $Ni^{+\delta+\delta'}Si^{-\delta}B^{-\delta'}$. The fact that the low valence Ni 2p peak exhibits a binding energy comparable with elemental nickel (only slight electron enrichment) and a negative shift compared to nickel silicide, despite overall electron transfer, is indicative of a back-donation effect well documented in metal-rich borides and alloys, especially nickel borides: the hybridization with boron sp states populates the Ni 3d states, which compensates the Ni 2p binding energy shift expected by a global electron impoverishment of the metal [37,38].

The surface of as-prepared Ni_6Si_2B is oxidised, as evidenced by the peak at 856.0 eV and its satellite at 861.2 eV in the Ni 2p window (**Figure 7a**), which correspond to high valence Ni in the form of Ni oxide or hydroxide forming spontaneously in contact with air.[34,39] Accordingly, the O 1s signal (**Figure 6g**) suggests a large contribution of hydroxide species at 531.5-531.8 eV,[39,40] which is present in all Ni samples (**Figure S27g**). Surface oxidation is also evidenced in the Si 2p and B 1s regions, which exhibit high energy components. The Si 2p window for Ni_6Si_2B (**Figure 7e**) shows a contribution at 102.4 eV, slightly shifted to lower energy compared to Ni_2Si (102.6 eV, **Figure S27e**), and negatively shifted by 1.4 eV compared to $NiSiO_3$ or SiO_2/Si (103.5-103.8 eV),[35,41] which suggests only partial oxidation of Si species. Surface borates or boron (hydr)oxide are detected by a peak at 191.9 eV in Ni_6Si_2B (**Figure 7f**). The binding energy rests

however lower than B_2O_3/H_3BO_3 (193.6-193.7 eV),[42,43] which indicates uncomplete oxidation of surface boron species.[44]

Cobalt borosilicide. XPS of as-prepared $Co_{4.75}Si_2B$ (**Figure S27b**) indicates a barely visible metallic Co contribution in the Co 2p region, due to deep surface oxidation upon air exposure. We have then stripped the passivation oxide layer by sputtering the surface with Ar^+ ions during 15 min. The metallic peak then appears clearly at 778.5 eV, together with high valence Co-states at 780.0 and 782.3 eV (**Figure 7b**). Silicon triggers a positive shift of the Co low valence component compared to elemental Co (777.8-778.1 eV) [40,45], evidenced by binding energies in Co silicides ranging from 778.2 to 778.5 eV [23,46,47] as we measured on CoSi (778.3 eV, **Figure 7b**). The low valence Si peak at 99.6 eV (**Figure 7e**) is ascribed to the borosilicide, but does not show any significant shift compared to elemental silicon. As in the borosilicide, the Co component in Co_2B is shifted to high energies (778.4 eV, **Figure 7b**) compared to elemental Co, as expected [48–50] and in agreement with the electronegativity scale, showing that no significant back-donation occurs from boron, contrary to the nickel borosilicide. The low valence boron peak at 188.3 eV (**Figure 7e**) is shifted to lower binding energies compared to elemental boron, corroborating electron deprivation from cobalt in favour of boron. Overall charge states can thus be summarised as $Co^{+\delta+\delta'}Si^{-\delta}B^{-\delta'}$, in agreement with the electronegativity scale.

High binding energy Co 2p contributions at 780.0 and 782.3 eV in as-prepared $Co_{4.75}Si_2B$ correspond to Co^{2+} and Co^{3+} species that indicate an oxidized surface (**Figure S27b**),[40,51] to a lesser extent but still present after sputtering (**Figure 7b**). The O 1s region (**Figure S27g**) of the as-prepared $Co_{4.75}Si_2B$ exhibits two peaks at 531.5 and 532.7 eV ascribed to $Co(OH)_2$ [51] and adsorbed water.[52] The SiO_x and BO_x contributions of $Co_{4.75}Si_2B$ are negatively shifted by 0.6 and 1.2 eV compared to CoSi (**Figure S27e**) and to Co_2B (**Figure S27f**), respectively.

Iron borosilicide. As for cobalt borosilicide, the surface of Fe_5SiB_2 was stripped from oxides after Ar-sputtering. Three contributions were then observed in the Fe $2p_{3/2}$ region at 707.0, 709.4, and 711.2 eV plus two satellites at 713.5 and 717.0 eV (**Figure 7c**, the full 2p spectrum of non-sputtered Fe_5SiB_2 is shown in **Figure S27c**). The low energy peak is found at the same binding energy as FeSi and FeB, in agreement with previous reports on iron silicides (707.0-707.3 eV)[53,54] and borides (706.9 -708.3 eV).[25,55] The positive shift of 0.4 eV compared to pure Fe (706.6 eV)[40]

suggests an electron transfer from iron to both silicon and boron, in agreement with the electronegativity scale and the negative shifts of 0.5 and 1.4 eV for low valence Si (99.0 eV, **Figure 7e**) and B (**Figure 7f**, 187.8 eV) compared to pure silicon and boron, respectively. This indicates electron deprivation resulting in a partial charge distribution $Fe^{+\delta+\delta'}Si^{-\delta}B^{-\delta'}$, like Ni_6Si_2B and $Co_{4.75}Si_2B$.

The oxide layer forming upon exposure to air of as-prepared Fe_5SiB_2 is characterised by high energy peaks at 709.4 and 711.2 eV in the Fe 2p region (**Figure S27c**), ascribed to Fe^{2+} and Fe^{3+} states [56–59] in agreement with the O 1s signal (**Figure S27g**) with components at 530.5 and 531.5 eV corresponding to Fe oxides and Fe hydroxides.[59] The SiO_x peak shows a negative shift of 1.1 eV (**Figure S27e**) compared to what we measure for FeSi.

Manganese borosilicide. The Mn $2p_{3/2}$ states of as-prepared Mn_5SiB_2 (**Figure 7d,** full Mn 2p spectrum in **Figure S27d**) were deconvoluted into contributions centred at 638.7, 641.4, 642.6 and 644.2 eV. The low energy peak is ascribed to the borosilicide, with a value consistent with both Mn silicides (638.6-638.7 eV) [53,60,61] and Mn borides (638.6-638.8 eV),[62,63] but also with elemental manganese (638.6 eV).[64] An oxidised layer is indicated by the energy contributions above 640.0 eV. The former and its minor satellite at 646.0 eV correspond to Mn^{2+} [64,65] whereas features at 642.6 and 644.2 eV correspond to Mn^{3+} and Mn^{4+} states, respectively [60,65], characteristic for manganese oxides or hydroxides forming on Mn compounds when brought in contact with air.[53,66] Silicon states on Mn_5SiB_2 are shifted to lower binding energies in both low (98.8 eV) and high valence states (102.2 eV, **Figure 7e**) in line with previous reports on Mn silicides.[53] Both low and high valence boron peaks are also shifted to lower binding energies (188.0 and 191.7 eV, **Figure 7f**). The overall charge distribution for Mn_5SiB_2 is similar to what we observe for Ni_6Si_2B and $Co_{4.75}Si_2B$, and Fe_5SiB_2. Similar to the nickel borosilicide and contrary to Co and Fe compounds, we do not observe a positive shift of the metal 2p binding energies. This indicates that like Ni_6Si_2B, Mn_5SiB_2 probably exhibits back-donation from boron to the Mn 3d states.

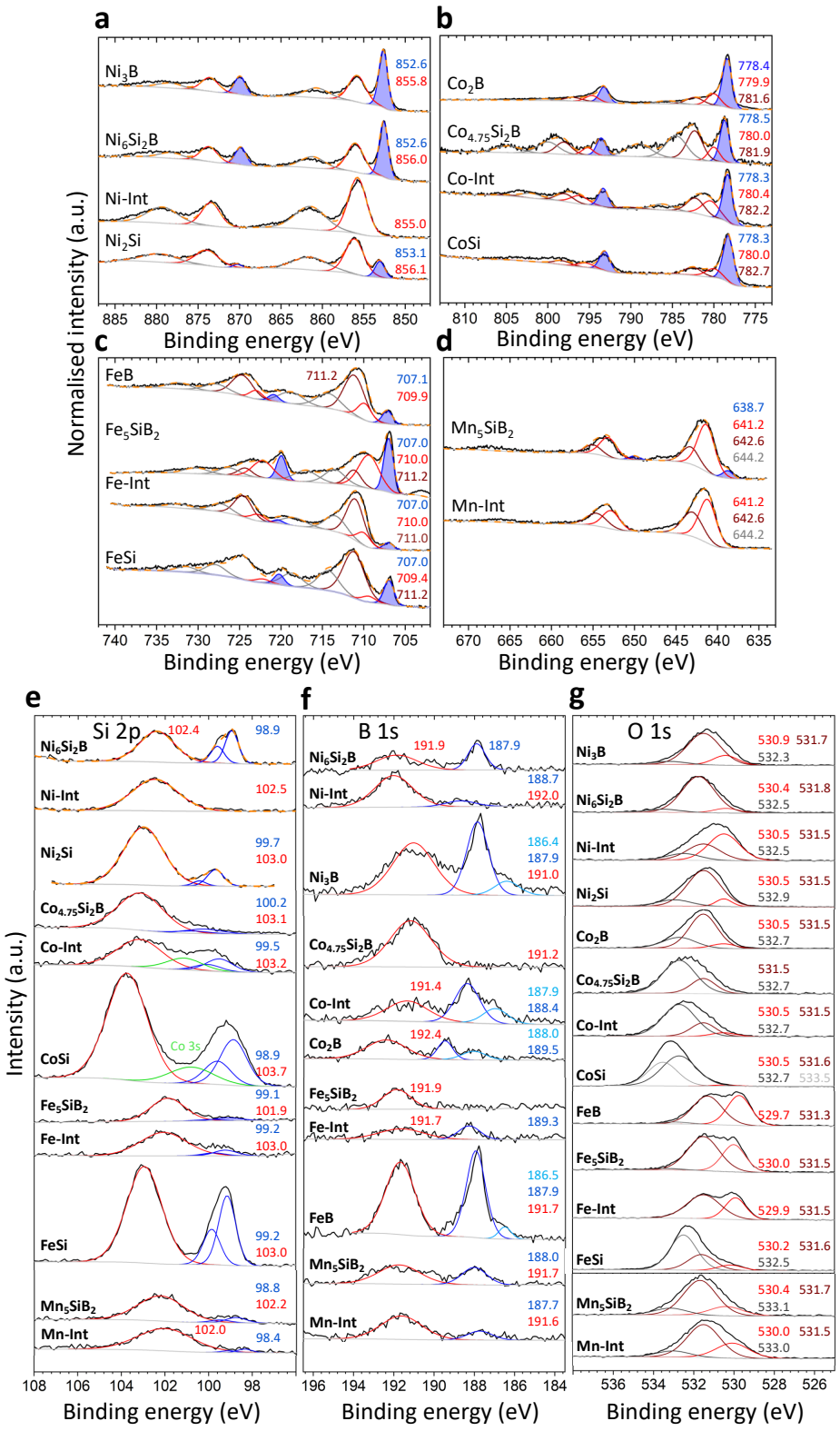

Figure S27. Deconvoluted HR-XP spectra of as-prepared borides, silicides, borosilicides and reaction intermediates (Int): (a) Ni 2p, (b) Co 2p, (c) Fe 2p, (d) Mn 2p, (e) Si 2p, (f) B 1s, (g) O 1s.

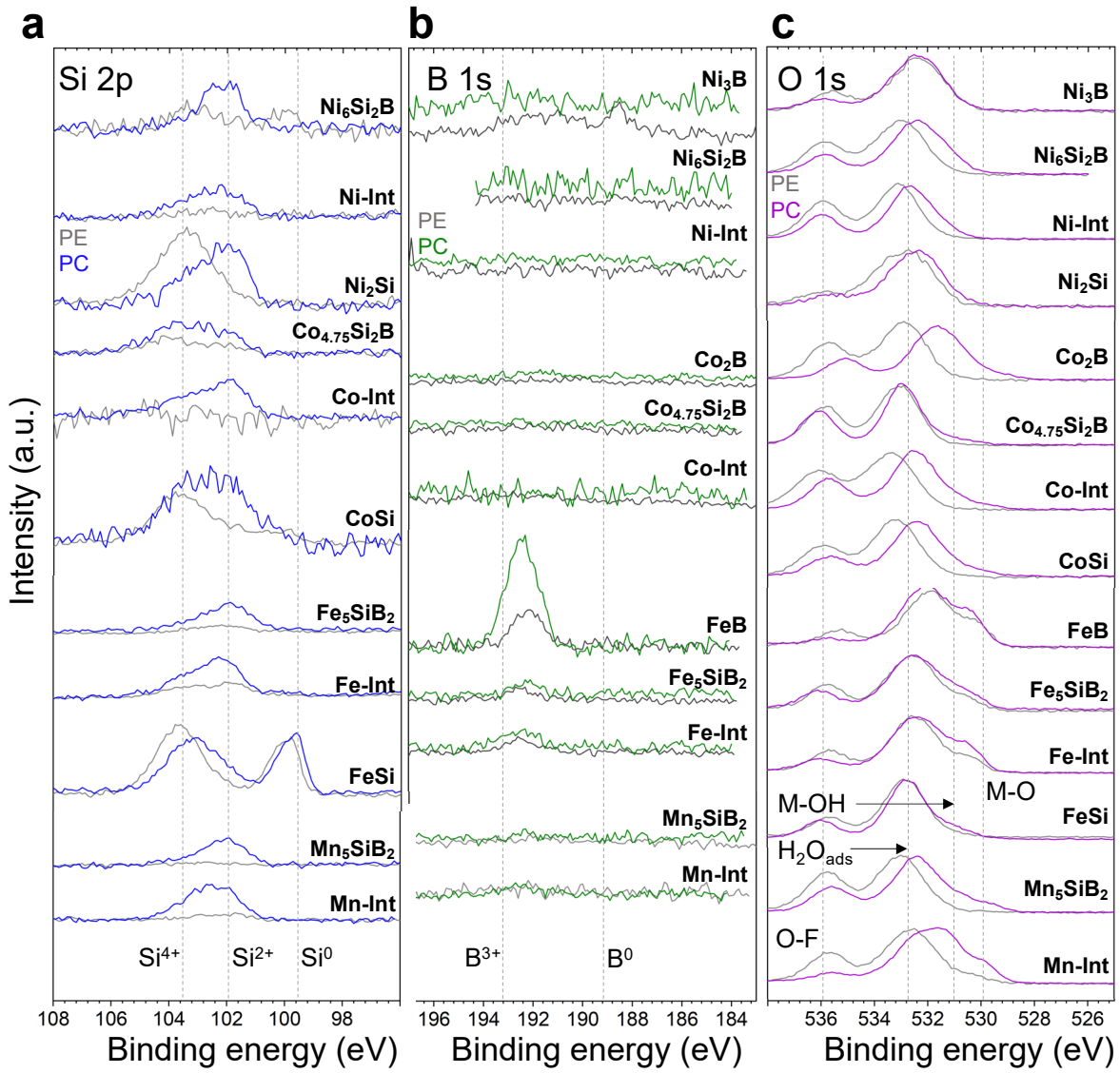

Figure S28. Comparison of XP spectra (non-normalised intensities) for electrodes before and after electrocatalysis. HR-XP spectra of (a) Si 2p where grey represents PE and blue PC, (b) B 1s where grey represents PE and green PC and (c) O 1s, where grey represents spectra of PE and violet of PC samples. Boron in (b) could not be confidently detected for the Ni-based and Co-based samples.

On the pristine (PE) Ni_6Si_2B and Ni_3B electrodes, $2p_{3/2}$ and $2p_{1/2}$ multiplet contributions characteristic of Ni-B environment (**Figure 7a**) are still observed at 852.7 and 870.4 eV (**Figure 8a**). Despite a lower sample concentration on the prepared electrode compared to the pristine powder, hence low intensity peaks, silicon is still detected (**Figure 8d** and **Figure S28a**). Boron was, however, not confidently detected in the HR-XP B 1s spectra of the Ni-based samples (**Figure S28b**). The fact that the binding energies of Ni species are close to the binding energies measured prior to electrode preparation (**Figure 7a**) suggests that the borosilicide/boride is preserved during electrode preparation, so that boron is maintained in the structure, but cannot be detected due to dilution of the material in the composite Nafion/carbon/catalyst electrode,

especially with the Nafion™ film wrapping the particles, made of elements heavier than boron. The surfaces of as-prepared Co-samples were already oxidized (**Figure 7b** was acquired after argon sputtering to remove part of the oxidized layer), and electrode processing did not change these surface states (**Figure 8c**).[40,51] Among Co-based electrodes, a silicide component (is detected at 778.5 eV (**Figure 8c**) only for CoSi, similar to the as-prepared sample (**Figure 7b**). Fe- and Mn-based electrodes show similar trends (**Figure 8c-e**, **S27-28**).

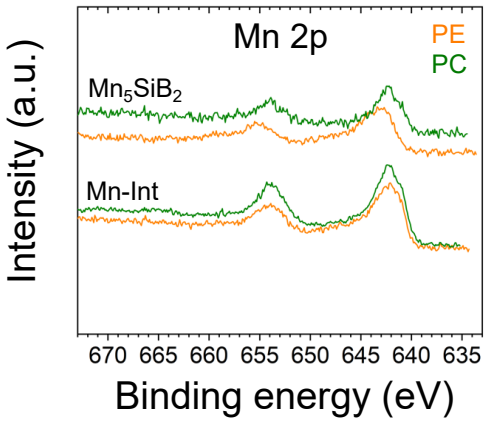

Figure S29. Non-normalised HR-XPS profiles of Mn-based (Mn 2p) electrodes before (orange) and after (green) chronoamperometry.

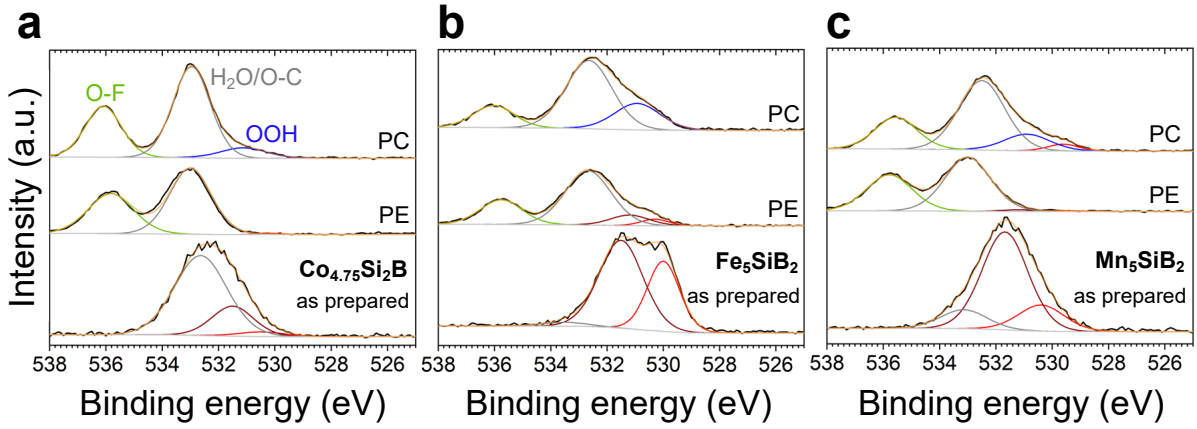

Figure S30. Deconvoluted O 1s XP-spectra of as-prepared borosilicides, pristine electrodes (PE) and after 2h CA (PC): (a) $Co_{4.75}Si_2B$, (b) Fe_5SiB_2 (c) Mn_5SiB_2.

SUPPLEMENTARY INFO-REFERENCES

(1) Song, Y.; Gómez-Recio, I.; Kumar, R.; Coelho Diogo, C.; Casale, S.; Génois, I.; Portehault, D. A Straightforward Approach to High Purity Sodium Silicide Na_4Si_4. *Dalton Trans.* **2021**, *50* (45), 16703–16710. https://doi.org/10.1039/D1DT03203H.

(2) Carenco, S.; Boissière, C.; Nicole, L.; Sanchez, C.; Le Floch, P.; Mézailles, N. Controlled Design of Size-Tunable Monodisperse Nickel Nanoparticles. *Chem. Mater.* **2010**, *22* (4), 1340–1349. https://doi.org/10.1021/cm902007g.

(3) Song, Y.; Casale, S.; Miche, A.; Montero, D.; Laberty-Robert, C.; Portehault, D. Converting Silicon Nanoparticles into Nickel Iron Silicide Nanocrystals within Molten Salts for Water Oxidation Electrocatalysis. *J. Mater. Chem. A* **2022**, *10* (3), 1350–1358. https://doi.org/10.1039/D1TA08097K.

(4) Igoa Saldaña, F.; Defoy, E.; Janisch, D.; Rousse, G.; Autran, P.-O.; Ghoridi, A.; Séné, A.; Baron, M.; Suescun, L.; Le Godec, Y.; Portehault, D. Revealing the Elusive Structure and Reactivity of Iron Boride α-FeB. *Inorg. Chem.* **2023**, *62* (5), 2073–2082. https://doi.org/10.1021/acs.inorgchem.2c03709.

(5) Toby, B. H.; Von Dreele, R. B. *GSAS-II* : The Genesis of a Modern Open-Source All Purpose Crystallography Software Package. *J. Appl. Crystallogr.* **2013**, *46* (2), 544–549. https://doi.org/10.1107/S0021889813003531.

(6) Azor, A.; Ruiz-Gonzalez, M. L.; Gonell, F.; Laberty-Robert, C.; Parras, M.; Sanchez, C.; Portehault, D.; González-Calbet, J. M. Nickel-Doped Sodium Cobaltite 2D Nanomaterials: Synthesis and Electrocatalytic Properties. *Chem. Mater.* **2018**, *30* (15), 4986–4994. https://doi.org/10.1021/acs.chemmater.8b01146.

(7) Trotochaud, L.; Young, S. L.; Ranney, J. K.; Boettcher, S. W. Nickel–Iron Oxyhydroxide Oxygen-Evolution Electrocatalysts: The Role of Intentional and Incidental Iron Incorporation. *J. Am. Chem. Soc.* **2014**, *136* (18), 6744–6753. https://doi.org/10.1021/ja502379c.

(8) Wei, C.; Sun, S.; Mandler, D.; Wang, X.; Qiao, S. Z.; Xu, Z. J. Approaches for Measuring the Surface Areas of Metal Oxide Electrocatalysts for Determining Their Intrinsic Electrocatalytic Activity. *Chem. Soc. Rev.* **2019**, *48* (9), 2518–2534. https://doi.org/10.1039/C8CS00848E.

(9) Connor, P.; Schuch, J.; Kaiser, B.; Jaegermann, W. The Determination of Electrochemical Active Surface Area and Specific Capacity Revisited for the System MnO_x as an Oxygen Evolution Catalyst. *Z. Für Phys. Chem.* **2020**, *234* (5), 979–994. https://doi.org/10.1515/zpch-2019-1514.

(10) Lugscheider, E.; Reimann, H.; Knotek, O. Das Dreistoffsystem Nickel-Bor-Silicium. *Monatshefte Für Chem. - Chem. Mon.* **1975**, *106* (5), 1155–1165. https://doi.org/10.1007/BF00906228.

(11) Aronsson, B.; Lundgren, G. X-Ray Investigations on Me-Si-B Systems. *Acta Chem. Scand.* **1959**, No. 13, 433–441.

(12) Cedervall, J.; Kontos, S.; Hansen, T. C.; Balmes, O.; Martinez-Casado, F. J.; Matej, Z.; Beran, P.; Svedlindh, P.; Gunnarsson, K.; Sahlberg, M. Magnetostructural Transition in Fe_5SiB_2 Observed with Neutron Diffraction. *J. Solid State Chem.* **2016**, *235*, 113–118. https://doi.org/10.1016/j.jssc.2015.12.016.

(13) ElMeligy, T. A.; Kota, S.; Natu, V.; Lind, H.; Palisaitis, J.; Persson, P. O. Å.; Rosen, J.; Barsoum, M. W. Synthesis, Characterization, Properties, First Principles Calculations, and X-Ray Photoelectron Spectroscopy of Bulk Mn_5SiB_2 and Fe_5SiB_2 Ternary Borides. *J.*

Alloys Compd. **2021**, *888*, 161377. https://doi.org/10.1016/j.jallcom.2021.161377.
(14) De Almeida, D. M.; Bormio-Nunes, C.; Nunes, C. A.; Coelho, A. A.; Coelho, G. C. Magnetic Characterization of Mn_5SiB_2 and Mn_5Si_3 Phases. *J. Magn. Magn. Mater.* **2009**, *321* (17), 2578–2581. https://doi.org/10.1016/j.jmmm.2009.03.067.
(15) Kumar, R.; Bahri, M.; Song, Y.; Gonell, F.; Thomas, C.; Ersen, O.; Sanchez, C.; Laberty-Robert, C.; Portehault, D. Phase Selective Synthesis of Nickel Silicide Nanocrystals in Molten Salts for Electrocatalysis of the Oxygen Evolution Reaction. *Nanoscale* **2020**, *12* (28), 15209–15213. https://doi.org/10.1039/D0NR04284F.
(16) Jung, S.; McCrory, C. C. L.; Ferrer, I. M.; Peters, J. C.; Jaramillo, T. F. Benchmarking Nanoparticulate Metal Oxide Electrocatalysts for the Alkaline Water Oxidation Reaction. *J. Mater. Chem. A* **2016**, *4* (8), 3068–3076. https://doi.org/10.1039/C5TA07586F.
(17) Masa, J.; Andronescu, C.; Antoni, H.; Sinev, I.; Seisel, S.; Elumeeva, K.; Barwe, S.; Marti-Sanchez, S.; Arbiol, J.; Roldan Cuenya, B.; Muhler, M.; Schuhmann, W. Role of Boron and Phosphorus in Enhanced Electrocatalytic Oxygen Evolution by Nickel Borides and Nickel Phosphides. *ChemElectroChem* **2019**, *6* (1), 235–240. https://doi.org/10.1002/celc.201800669.
(18) Liu, G.; He, D.; Yao, R.; Zhao, Y.; Li, J. Amorphous NiFeB Nanoparticles Realizing Highly Active and Stable Oxygen Evolving Reaction for Water Splitting. *Nano Res.* **2018**, *11* (3), 1664–1675. https://doi.org/10.1007/s12274-017-1783-0.
(19) Stern, L.-A.; Feng, L.; Song, F.; Hu, X. Ni $_2$ P as a Janus Catalyst for Water Splitting: The Oxygen Evolution Activity of Ni_2P Nanoparticles. *Energy Environ. Sci.* **2015**, *8* (8), 2347–2351. https://doi.org/10.1039/C5EE01155H.
(20) Elumeeva, K.; Masa, J.; Medina, D.; Ventosa, E.; Seisel, S.; Kayran, Y. U.; Genç, A.; Bobrowski, T.; Weide, P.; Arbiol, J.; Muhler, M.; Schuhmann, W. Cobalt Boride Modified with N-Doped Carbon Nanotubes as a High-Performance Bifunctional Oxygen Electrocatalyst. *J Mater Chem A* **2017**, *5* (40), 21122–21129. https://doi.org/10.1039/C7TA06995B.
(21) Ma, X.; Wen, J.; Zhang, S.; Yuan, H.; Li, K.; Yan, F.; Zhang, X.; Chen, Y. Crystal Co_xB (x = 1–3) Synthesized by a Ball-Milling Method as High-Performance Electrocatalysts for the Oxygen Evolution Reaction. *ACS Sustain. Chem. Eng.* **2017**, *5* (11), 10266–10274. https://doi.org/10.1021/acssuschemeng.7b02281.
(22) Hu, G.; Xiang, J.; Li, J.; Liu, P.; Ali, R. N.; Xiang, B. Urchin-like Ternary Cobalt Phosphosulfide as High-Efficiency and Stable Bifunctional Electrocatalyst for Overall Water Splitting. *J. Catal.* **2019**, *371*, 126–134. https://doi.org/10.1016/j.jcat.2019.01.039.
(23) Song, Y.; Gómez-Recio, I.; Ghoridi, A.; Igoa Saldaña, F.; Janisch, D.; Sassoye, C.; Dupuis, V.; Hrabovsky, D.; Ruiz-González, M. L.; González-Calbet, J. M.; Casale, S.; Zitolo, A.; Lassalle-Kaiser, B.; Laberty-Robert, C.; Portehault, D. Heterostructured Cobalt Silicide Nanocrystals: Synthesis in Molten Salts, Ferromagnetism, and Electrocatalysis. *J. Am. Chem. Soc.* **2023**, jacs.3c01110. https://doi.org/10.1021/jacs.3c01110.
(24) Hausmann, J. N.; Beltrán-Suito, R.; Mebs, S.; Hlukhyy, V.; Fässler, T. F.; Dau, H.; Driess, M.; Menezes, P. W. Evolving Highly Active Oxidic Iron(III) Phase from Corrosion of Intermetallic Iron Silicide to Master Efficient Electrocatalytic Water Oxidation and Selective Oxygenation of 5-Hydroxymethylfurfural. *Adv. Mater.* **2021**, *33* (27), 2008823. https://doi.org/10.1002/adma.202008823.
(25) Qiang, C.; Zhang, L.; He, H.; Liu, Y.; Zhao, Y.; Sheng, T.; Liu, S.; Wu, X.; Fang, Z. Efficient Electrocatalytic Water Splitting by Bimetallic Cobalt Iron Boride Nanoparticles

with Controlled Electronic Structure. *J. Colloid Interface Sci.* **2021**, *604*, 650–659. https://doi.org/10.1016/j.jcis.2021.07.024.
(26) Han, G.-Q.; Liu, Y.-R.; Hu, W.-H.; Dong, B.; Li, X.; Shang, X.; Chai, Y.-M.; Liu, Y.-Q.; Liu, C.-G. Crystallographic Structure and Morphology Transformation of MnO_2 Nanorods as Efficient Electrocatalysts for Oxygen Evolution Reaction. *J. Electrochem. Soc.* **2016**, *163* (2), H67–H73. https://doi.org/10.1149/2.0371602jes.
(27) Guo, C. X.; Chen, S.; Lu, X. Ethylenediamine-Mediated Synthesis of Mn_3O_4 Nano-Octahedrons and Their Performance as Electrocatalysts for the Oxygen Evolution Reaction. *Nanoscale* **2014**, *6* (18), 10896–10901. https://doi.org/10.1039/C4NR03822C.
(28) Gorlin, Y.; Jaramillo, T. F. A Bifunctional Nonprecious Metal Catalyst for Oxygen Reduction and Water Oxidation. *J. Am. Chem. Soc.* **2010**, *132* (39), 13612–13614. https://doi.org/10.1021/ja104587v.
(29) McCrory, C. C. L.; Jung, S.; Peters, J. C.; Jaramillo, T. F. Benchmarking Heterogeneous Electrocatalysts for the Oxygen Evolution Reaction. *J. Am. Chem. Soc.* **2013**, *135* (45), 16977–16987. https://doi.org/10.1021/ja407115p.
(30) Lu, Y.; Wang, W.; Xie, F. Investigation of Oxygen Evolution Reaction Kinetic Process and Kinetic Parameters on Iridium Electrode by Electrochemistry Impedance Spectroscopy Analysis. *J. Electroanal. Chem.* **2020**, *871*, 114281. https://doi.org/10.1016/j.jelechem.2020.114281.
(31) Qi, J.; Zhang, W.; Xiang, R.; Liu, K.; Wang, H.; Chen, M.; Han, Y.; Cao, R. Porous Nickel–Iron Oxide as a Highly Efficient Electrocatalyst for Oxygen Evolution Reaction. *Adv. Sci.* **2015**, *2* (10), 1500199. https://doi.org/10.1002/advs.201500199.
(32) Ma, F.; Wang, S.; Liang, X.; Wang, C.; Tong, F.; Wang, Z.; Wang, P.; Liu, Y.; Dai, Y.; Zheng, Z.; Huang, B. Ni3B as a Highly Efficient and Selective Catalyst for the Electrosynthesis of Hydrogen Peroxide. *Appl. Catal. B Environ.* **2020**, *279*, 119371. https://doi.org/10.1016/j.apcatb.2020.119371.
(33) Masa, J.; Piontek, S.; Wilde, P.; Antoni, H.; Eckhard, T.; Chen, Y.; Muhler, M.; Apfel, U.; Schuhmann, W. Ni-Metalloid (B, Si, P, As, and Te) Alloys as Water Oxidation Electrocatalysts. *Adv. Energy Mater.* **2019**, 1900796. https://doi.org/10.1002/aenm.201900796.
(34) Yuan, W.; Zhao, X.; Hao, W.; Li, J.; Wang, L.; Ma, X.; Guo, Y. Performance of Surface-Oxidized Ni_3B, Ni_2B, and NiB_2 Electrocatalysts for Overall Water Splitting. *ChemElectroChem* **2019**, *6* (3), 764–770. https://doi.org/10.1002/celc.201801354.
(35) Hollinger, G. Structures Chimique et Electronique de l'interface SiO2-Si. *Appl. Surf. Sci.* **1981**, *8* (3), 318–336. https://doi.org/10.1016/0378-5963(81)90126-4.
(36) Gouget, G.; Debecker, D. P.; Kim, A.; Olivieri, G.; Gallet, J.-J.; Bournel, F.; Thomas, C.; Ersen, O.; Moldovan, S.; Sanchez, C.; Carenco, S.; Portehault, D. In Situ Solid–Gas Reactivity of Nanoscaled Metal Borides from Molten Salt Synthesis. *Inorg. Chem.* **2017**, *56* (15), 9225–9234. https://doi.org/10.1021/acs.inorgchem.7b01279.
(37) Diplas, S.; Løvvik, O. M. Electronic Structure Studies of Ni–X (X: B, S, P) Alloys Using x-Ray Photoelectron Spectroscopy, x-Ray Induced Auger Electron Spectroscopy and Density Functional Theory Calculations. *J. Phys. Condens. Matter* **2009**, *21* (24), 245503. https://doi.org/10.1088/0953-8984/21/24/245503.
(38) Carenco, S.; Portehault, D.; Boissière, C.; Mézailles, N.; Sanchez, C. Nanoscaled Metal Borides and Phosphides: Recent Developments and Perspectives. *Chem. Rev.* **2013**, *113* (10), 7981–8065. https://doi.org/10.1021/cr400020d.

(39) Masa, J.; Sinev, I.; Mistry, H.; Ventosa, E.; De La Mata, M.; Arbiol, J.; Muhler, M.; Roldan Cuenya, B.; Schuhmann, W. Ultrathin High Surface Area Nickel Boride (Ni_xB) Nanosheets as Highly Efficient Electrocatalyst for Oxygen Evolution. *Adv. Energy Mater.* **2017**, *7* (17), 1700381. https://doi.org/10.1002/aenm.201700381.
(40) Biesinger, M. C.; Payne, B. P.; Grosvenor, A. P.; Lau, L. W. M.; Gerson, A. R.; Smart, R. St. C. Resolving Surface Chemical States in XPS Analysis of First Row Transition Metals, Oxides and Hydroxides: Cr, Mn, Fe, Co and Ni. *Appl. Surf. Sci.* **2011**, *257* (7), 2717–2730. https://doi.org/10.1016/j.apsusc.2010.10.051.
(41) Venezia, A. M.; Bertoncello, R.; Deganello, G. X-Ray Photoelectron Spectroscopy Investigation of Pumice-Supported Nickel Catalysts. *Surf. Interface Anal.* **1995**, *23* (4), 239–247. https://doi.org/10.1002/sia.740230408.
(42) Gouin, X.; Grange, P.; Bois, L.; L'Haridon, P.; Laurent, Y. Characterization of the Nitridation Process of Boric Acid. *J. Alloys Compd.* **1995**, *224* (1), 22–28. https://doi.org/10.1016/0925-8388(95)01532-9.
(43) Joyner, D. J.; Hercules, D. M. Chemical Bonding and Electronic Structure of B_2O_3 , H_3BO_3 , and BN: An ESCA, Auger, SIMS, and SXS Study. *J. Chem. Phys.* **1980**, *72* (2), 1095–1108. https://doi.org/10.1063/1.439251.
(44) Schreifels, J. X-Ray Photoelectron Spectroscopy of Nickel Boride Catalysts: Correlation of Surface States with Reaction Products in the Hydrogenation of Acrylonitrile. *J. Catal.* **1980**, *65* (1), 195–206. https://doi.org/10.1016/0021-9517(80)90294-8.
(45) McIntyre, N. S.; Johnston, D. D.; Coatsworth, L. L.; Davidson, R. D.; Brown, J. R. X-Ray Photoelectron Spectroscopic Studies of Thin Film Oxides of Cobalt and Molybdenum. *Surf. Interface Anal.* **1990**, *15* (4), 265–272. https://doi.org/10.1002/sia.740150406.
(46) Prabhakaran, K.; Ogino, T. Behavior of Ultrathin Layers of Co on Si and Ge Systems. *Appl. Surf. Sci.* **1996**, *100–101*, 518–521. https://doi.org/10.1016/0169-4332(96)00331-5.
(47) García-Méndez, M.; Castillón, F. F.; Hirata, G. A.; Farías, M. H.; Beamson, G. XPS and HRTEM Characterization of Cobalt–Nickel Silicide Thin Films. *Appl. Surf. Sci.* **2000**, *161* (1–2), 61–73. https://doi.org/10.1016/S0169-4332(00)00122-7.
(48) Masa, J.; Weide, P.; Peeters, D.; Sinev, I.; Xia, W.; Sun, Z.; Somsen, C.; Muhler, M.; Schuhmann, W. Amorphous Cobalt Boride (Co_2B) as a Highly Efficient Nonprecious Catalyst for Electrochemical Water Splitting: Oxygen and Hydrogen Evolution. *Adv. Energy Mater.* **2016**, *6* (6), 1502313. https://doi.org/10.1002/aenm.201502313.
(49) Krishnan, P.; Hsueh, K.-L.; Yim, S.-D. Catalysts for the Hydrolysis of Aqueous Borohydride Solutions to Produce Hydrogen for PEM Fuel Cells. *Appl. Catal. B Environ.* **2007**, *77* (1–2), 206–214. https://doi.org/10.1016/j.apcatb.2007.07.024.
(50) Chen, Z.; Kang, Q.; Cao, G.; Xu, N.; Dai, H.; Wang, P. Study of Cobalt Boride-Derived Electrocatalysts for Overall Water Splitting. *Int. J. Hydrog. Energy* **2018**, *43* (12), 6076–6087. https://doi.org/10.1016/j.ijhydene.2018.01.161.
(51) Yang, J.; Liu, H.; Martens, W. N.; Frost, R. L. Synthesis and Characterization of Cobalt Hydroxide, Cobalt Oxyhydroxide, and Cobalt Oxide Nanodiscs. *J. Phys. Chem. C* **2010**, *114* (1), 111–119. https://doi.org/10.1021/jp908548f.
(52) Wagner, C. D.; Gale, L. H.; Raymond, R. H. Two-Dimensional Chemical State Plots: A Standardized Data Set for Use in Identifying Chemical States by x-Ray Photoelectron Spectroscopy. *Anal. Chem.* **1979**, *51* (4), 466–482. https://doi.org/10.1021/ac50040a005.
(53) Ohtsu, N.; Oku, M.; Nomura, A.; Sugawara, T.; Shishido, T.; Wagatsuma, K. X-Ray Photoelectron Spectroscopic Studies on Initial Oxidation of Iron and Manganese Mono-

Silicides. *Appl. Surf. Sci.* **2008**, *254* (11), 3288–3294. https://doi.org/10.1016/j.apsusc.2007.11.005.
(54) Guan, J.; Chen, X.; Yang, K.; Rykov, A.; Wang, J.; Liang, C. Preparation and Size-Dependent Magnetism of Highly Dispersed Iron Silicide Nanoparticles on Silica. *J. Mater. Chem. C* **2014**, *2* (27), 5292. https://doi.org/10.1039/c4tc00676c.
(55) Xie, Y.; Wang, Q.; Guo, Z.; Qian, L.; Chen, M.; Yan, J. Electron Induced Efficient Dechlorination of Trichlorethylene with S Doped Fe_2B: The Enhancement Mechanism of S. *Environ. Int.* **2022**, *170*, 107619. https://doi.org/10.1016/j.envint.2022.107619.
(56) Brion, D. Etude Par Spectroscopie de Photoelectrons de La Degradation Superficielle de FeS2, CuFeS2, ZnS et PbS a l'air et Dans l'eau. *Appl. Surf. Sci.* **1980**, *5* (2), 133–152. https://doi.org/10.1016/0378-5963(80)90148-8.
(57) Joyner, D. J.; Johnson, O.; Hercules, D. M. A Study of the Iron Borides. 1. Electron Spectroscopy. *J. Am. Chem. Soc.* **1980**, *102* (6), 1910–1917. https://doi.org/10.1021/ja00526a025.
(58) Graat, P. C. J.; Somers, M. A. J. Simultaneous Determination of Composition and Thickness of Thin Iron-Oxide Films from XPS Fe 2p Spectra. *Appl. Surf. Sci.* **1996**, *100–101*, 36–40. https://doi.org/10.1016/0169-4332(96)00252-8.
(59) Bhargava, G.; Gouzman, I.; Chun, C. M.; Ramanarayanan, T. A.; Bernasek, S. L. Characterization of the "Native" Surface Thin Film on Pure Polycrystalline Iron: A High Resolution XPS and TEM Study. *Appl. Surf. Sci.* **2007**, *253* (9), 4322–4329. https://doi.org/10.1016/j.apsusc.2006.09.047.
(60) Li, W.; Shen, B.; Kang, J.; Wang, Z.; He, Y. Oxygen Evolution and Corrosion Behaviours of the Porous Mn_5Si_3 Electrode in Sulfuric Acid. *Mater. Res. Express* **2019**, *6* (8), 085542. https://doi.org/10.1088/2053-1591/ab26a3.
(61) Ohtsu, N.; Oku, M.; Shishido, T.; Wagatsuma, K. Experimental Calibration Curve for Quantitative XPS Analysis Constructed from in Situ Fractured Polycrystalline Manganese Silicide Surfaces: Experimental Calibration Curve for Quantitative XPS Analysis. *Surf. Interface Anal.* **2012**, *44* (8), 993–996. https://doi.org/10.1002/sia.4867.
(62) Ma, S.; Bao, K.; Tao, Q.; Zhu, P.; Ma, T.; Liu, B.; Liu, Y.; Cui, T. Manganese Mono-Boride, an Inexpensive Room Temperature Ferromagnetic Hard Material. *Sci. Rep.* **2017**, *7* (1), 43759. https://doi.org/10.1038/srep43759.
(63) Ma, S.; Bao, K.; Tao, Q.; Xu, C.; Feng, X.; Zhao, X.; Ge, Y.; Zhu, P.; Cui, T. Double-Zigzag Boron Chain-Enhanced Vickers Hardness and Manganese Bilayers-Induced High d-Electron Mobility in Mn_3B_4. *Phys. Chem. Chem. Phys.* **2019**, *21* (5), 2697–2705. https://doi.org/10.1039/C8CP05870A.
(64) Hsin-Kuei, H.; Rabalais, J. W. Chemisorption and the Initial Stage of Oxidation on Mn. *Surf. Sci.* **1981**, *107* (2–3), 376–390. https://doi.org/10.1016/0039-6028(81)90533-1.
(65) Audi, A. A.; Sherwood, P. M. A. Valence-Band x-Ray Photoelectron Spectroscopic Studies of Manganese and Its Oxides Interpreted by Cluster and Band Structure Calculations. *Surf. Interface Anal.* **2002**, *33* (3), 274–282. https://doi.org/10.1002/sia.1211.
(66) Bondi, J. F.; Oyler, K. D.; Ke, X.; Schiffer, P.; Schaak, R. E. Chemical Synthesis of Air-Stable Manganese Nanoparticles. *J. Am. Chem. Soc.* **2009**, *131* (26), 9144–9145. https://doi.org/10.1021/ja901372q.